

**Michael Murböck**

**Virtual Constellations of  
Next Generation Gravity Missions**

**München 2015**

---

**Verlag der Bayerischen Akademie der Wissenschaften  
in Kommission beim Verlag C. H. Beck**





Virtual Constellations of  
Next Generation Gravity Missions

Vollständiger Abdruck  
der von der Ingenieur fakultät Bau Geo Umwelt  
der Technischen Universität München  
zur Erlangung des akademischen Grades eines  
Doktor-Ingenieurs (Dr.-Ing.)  
genehmigten Dissertation

von

Michael Murböck

München 2015

---

Verlag der Bayerischen Akademie der Wissenschaften  
in Kommission beim Verlag C. H. Beck

Adresse der Deutschen Geodätischen Kommission:



Deutsche Geodätische Kommission

Alfons-Goppel-Straße 11 • D – 80 539 München  
Telefon +49 – 89 – 23 031 1113 • Telefax +49 – 89 – 23 031 -1283 /- 1100  
e-mail hornik@dgfi.badw.de • <http://www.dgk.badw.de>

Prüfungskommission

Vorsitzender: Univ.-Prof. Dr.-Ing. habil. T. Wunderlich  
Prüfer der Dissertation: 1. Univ.-Prof. Dr.techn. R. Pail  
2. Univ.-Prof. Dr.-Ing. N. Sneeuw, Universität Stuttgart  
3. Univ.-Prof. Dr.-Ing, Dr.h.c. mult. R. Rummel (i.R.)

Die Dissertation wurde am 19.02.2015 bei der Technischen Universität München eingereicht  
und durch die Ingenieur fakultät Bau Geo Umwelt am 10.06.2015 angenommen.

Diese Dissertation ist auf dem Server der Deutschen Geodätischen Kommission unter <http://dgk.badw.de/>  
sowie auf dem Server der Technischen Universität München unter  
<<http://nbn-resolving.de/urn/resolver.pl?urn:nbn:de:bvb:91-diss-20150619-1241150-1-7>> elektronisch publiziert

---

© 2015 Deutsche Geodätische Kommission, München

Alle Rechte vorbehalten. Ohne Genehmigung der Herausgeber ist es auch nicht gestattet,  
die Veröffentlichung oder Teile daraus auf photomechanischem Wege (Photokopie, Mikrokopie) zu vervielfältigen.

## Abstract

The monitoring of the Earth's gravity field is of major scientific and societal importance. Gravity field observations reflect the mass distribution and its changes with time in the Earth's system. The knowledge on many geophysical processes as, for example, the global water cycle and ice sheet mass variations, can be improved with these observations. With dedicated satellite missions the Earth's gravity field can be observed on a global scale. In this thesis Virtual Constellations of Next Generation Gravity Missions (NGGM) are assessed. The key questions for the NGGM concern science requirements, mission objectives, instrument accuracies and orbit constellations.

The science requirements are the basis for assessing the NGGM. The whole set of science requirements are 19 signals of interest in the fields of hydrology, glaciology, oceanography, solid Earth physics, and geodesy. They are unified to monthly geoid height accuracy requirements, i.e. the basic temporal resolution and the basic gravitational unit used in this thesis. The number of satellites in the NGGM constellations is limited, and therefore there is also a limit for the spatial resolution which can be achieved after one month. Constellations of 1, 2, and 4 satellites are investigated and nearly 50% of the science requirements can not be met with the required resolution.

This assessment leads to the mission objectives for the NGGM. The mission objectives ensure the NGGM to fulfil the selected science requirements with required accuracy and required spatial and temporal resolution. Four mission objectives are formulated concerning the orbital groundtrack coverage, the mission duration and the required monthly geoid height accuracies for specific spatial resolutions. The two main monthly geoid height accuracy requirements are 0.01 mm at a spatial resolutions of 500 km, and 0.4 mm for 150 km.

The basic satellite scenarios for the NGGM are discussed for different measurement concepts. The most promising measurement concept is satellite-to-satellite tracking (SST) between two low Earth orbiting satellites (low-low SST). This concept is operated by the Gravity Recovery and Climate Experiment (GRACE), which is now in orbit for 13 years and allows for estimating a global gravity field every month.

For the NGGM the low-low SST concept of GRACE has to be improved concerning instrument accuracy and observation geometry. The observation geometry of GRACE is weak, because the two satellites are on the same orbit with constant inter-satellite distance. This is called an in-line formation, and the inter-satellite observations for polar in-line pairs such as GRACE are mainly north-south directed. Therefore the observations are weak in east-west direction. The optimum are isotropic observations which are invariant with respect to direction. Two possibilities for a single and a double low-low SST pair are analysed in order to increase isotropy of the observations. For a single pair it is the so-called Pendulum formation where the trailing satellite of the single pair is in a different orbit with a separation in the ascending node. A double pair scenario consists of an in-line polar and an in-line pair in a 70° inclined orbit.

The instrument requirements for the NGGM depend on the orbital altitude. The selected single and double pair scenarios are in three altitude bands around 300, 360, and 420 km. From semi-analytical simulations results are derived in terms of the formal errors of the scenarios the instrument requirements for the key instruments of a low-low SST mission, i.e. the inter-satellite ranging instrument and the accelerometer. For the ranging instrument a noise level between 2 nm (high altitude) and 20 nm (low altitude) is required. For the accelerometer it is around  $2 \cdot 10^{-12}$  m/s<sup>2</sup>.

The largest error contribution for the NGGM is temporal aliasing mainly due to high-frequency tidal and non-tidal mass variations in the ocean and atmosphere. The effect of temporal aliasing is analysed based on the simulation of the sampling of signals with discrete frequencies with single and double pairs. The effects of temporal aliasing are resonances at specific spherical harmonic (SH) orders. The magnitude of the effects at these orders depends on the basic periods of a satellite orbit, i.e. the revolution time and the length of the nodal day. In order to avoid large resonances optimal altitude bands are selected in

which the orbits of the NGGM are found. Two methods to reduce the resonances for single and double pairs are presented as well.

The final simulation results in terms of monthly gravity retrievals include the three main error contributions of the instrument noise and of temporal aliasing from tidal and non-tidal sources. It is shown that the high-frequency signal contents have to be reduced from the observations in order to benefit from the highly sensitive instruments. There are basically two options to reduce these contents. One is a classical de-aliasing approach (applied also for current GRACE solutions) which aims at a reduction of the high-frequency signal contents in atmosphere and ocean (tidal and non-tidal) with a priori model information. Another option is the co-estimation of short period gravity field parameters. This option is discussed and validated with respect to a double low-low SST pair.

The best monthly gravity retrieval performance out of the basic scenarios is reached for the double low-low SST pairs in the low selected altitude band (300 km). The required monthly geoid accuracy is reached, if the temporal aliasing effects from full tidal and non-tidal variations are reduced by a factor of between 30 and 60. With this reduction the three best NGGM double pair scenarios with polar pairs in 300, 360, and 420 km altitude combined with a 70° inclined pair in 270 km altitude are able to provide a global geoid with an accuracy of 0.01 mm at 500 km spatial resolution, and of 0.4 mm at 150 km spatial resolution.

The NGGM is of great importance for science and society. Increased spatial and temporal resolution as well as increased accuracy of global gravity field models will improve the understanding of many processes in system Earth. The science requirements which can be fulfilled with the NGGM with the required resolution are in the fields of geodesy, oceanography, hydrology, glaciology, and solid Earth physics. For example, the requirements for unified height systems, ground water, glacial isostatic adjustment, and ice mass balance are fulfilled with the NGGM.

## Zusammenfassung

Die Beobachtung des Schwerefeldes der Erde hat große wissenschaftliche und gesellschaftliche Bedeutung. Das Schwerefeld beinhaltet Informationen über die Massenverteilung und ihre zeitlichen Änderungen im System Erde. Somit können daraus die Kenntnisse über viele geophysikalische Prozesse vertieft werden, wie zum Beispiel über den globalen Wasserkreislauf und die Massenveränderungen der Eisschilde. Mit Satellitenmissionen kann das Erdschwerefeld global erfasst werden. In dieser Dissertation werden optimale Konstellationen für Schwerefeldsatellitenmissionen der nächsten Generation (Next Generation Gravity Mission, NGGM) ermittelt. Die wichtigsten Fragen beziehen sich dabei auf die wissenschaftlichen Anforderungen, die konkreten Ziele der Satellitenmission, sowie Instrumentengenauigkeiten und Orbitkonstellationen.

Die wissenschaftlichen Anforderungen sind die Grundlage für die Planung der NGGM. Die Auswahl für diese Dissertation besteht aus 19 zu beobachtenden Signalen in Hydrosphäre, Kryosphäre, den Ozeanen, der festen Erde und im Bereich Geodäsie. Zunächst werden diese Anforderungen vereinheitlicht bezüglich ihrer physikalischen Einheit und der zeitlichen Auflösung. Als Einheit werden Geoidhöhen, und als zeitliche Auflösung ein Monat verwendet. Weil die Anzahl der Satelliten für die NGGM beschränkt ist, gibt es auch eine Grenze der erzielbaren räumlichen Auflösung nach einem Monat. Die NGGM-Konstellationen bestehen aus 1, 2 und 4 Satelliten. Damit können beinahe 50% der gewünschten Signale nicht mit der geforderten Auflösung ermittelt werden.

Aus den wissenschaftlichen Anforderungen werden die Ziele der NGGM abgeleitet. Diese ermöglichen es der NGGM, die ausgewählten Signale mit geforderter Genauigkeit und Auflösung zu beobachten. Vier solche Ziele sind formuliert bezüglich der globalen Überdeckung mit Satellitenbodenspuren, der Missionsdauer und der erforderlichen monatlichen Geoidhöhengengenauigkeit für verschiedene räumliche Auflösungen. Die geforderte (mittlere globale) monatliche Geoidhöhengengenauigkeit ist 0.01 mm für eine räumliche Auflösung von 500 km und 0.4 mm für 150 km.

Verschiedene Beobachtungskonzepte werden in den Basisszenarien der NGGM herangezogen. Das vielversprechendste Konzept ist die genaue Messung der Intersatellitendistanz zwischen zwei tieffliegenden Satelliten (satellite-to-satellite tracking in low-low mode, low-low SST). Dieses Konzept wird bereits erfolgreich in der Satellitenmission Gravity Recovery and Climate Experiment (GRACE) angewendet, welche seit 13 Jahren im Orbit ist und es erlaubt, das globale Erdschwerefeld monatlich zu erfassen.

Für die NGGM muss das low-low SST Konzept von GRACE im Hinblick auf Instrumentengenauigkeit und Beobachtungsgeometrie verbessert werden. GRACE besitzt eine schwache Beobachtungsgeometrie, weil sich die beiden Satelliten im selben polaren Orbit mit konstanter Entfernung zueinander bewegen. Dies wird In-line Formation genannt, und die Intersatellitenbeobachtungen sind damit vorwiegend in Nord-Süd-Ausrichtung orientiert. Das In-line-Konzept ist somit weniger sensitiv in Ost-West-Richtung. Eine optimale Beobachtung wäre isotrop und damit unabhängig von der Richtung. Für das low-low SST Konzept bieten sich zwei Möglichkeiten, die Isotropie zu erhöhen. Bei einem Einzelpaar in einer sogenannten Pendel-Formation erhalten die Intersatellitenbeobachtungen mehr Anteile quer zur Flugrichtung, weil sich das zweite Paar in einem Orbit mit versetztem aufsteigenden Knoten befindet. Für ein Doppelpaar kommen mehr Ost-West-gerichtete Beobachtungen hinzu aufgrund der niedrigeren Inklination eines der beiden Paare. Für die NGGM wird für das zweite Paar eine Inklination von 70° gewählt.

Die Instrumentenanforderungen hängen von der Orbithöhe ab. Die ausgewählten Einzel- und Doppelpaar-Szenarien befinden sich in drei Höhenbändern um 300, 360 und 420 km. Mit Hilfe von semi-analytischen Simulationen resultierend in formalen Fehlern für die Schwerefeldlösungen der Szenarien werden die Anforderungen an die beiden wichtigsten Instrumente einer low-low SST Mission abgeleitet. Dies sind das Instrument zur Messung der Intersatellitendistanz und die Beschleunigungsmesser. Die geforderte Genauigkeit für die Distanzmessung liegt zwischen 2 nm für die hoch und 20 nm für die niedrig fliegenden Szenarien. Die Genauigkeitsanforderungen an die Beschleunigungsmesser liegt bei  $2 \cdot 10^{-12} \text{ m/s}^2$ .

Die größten Fehlerbeiträge der NGGM kommen von zeitlichem Aliasing vorwiegend aufgrund von hochfrequenten Massenvariationen in den Ozeanen und der Atmosphäre. Dieser Effekt von zeitlichem Aliasing ist analysiert mit Simulationen der Abtastung von Signalen mit diskreten Frequenzen mit Einzel- und Doppelpaaren. Ein wichtiger Effekt von zeitlichem Aliasing sind Resonanzen bei bestimmten sphärisch-harmonischen (SH) Ordnungen. Die Größenordnung dieser Resonanzen hängt von den beiden Hauptperioden eines Orbits ab. Diese sind die Umlaufperiode und die Länge des Knotentages. Durch eine optimale Wahl der Flughöhe eines Satelliten können große Resonanzen vermieden werden. Die Szenarien der NGGM befinden sich alle in solchen optimalen Höhenbändern. Desweiteren werden auch zwei Prozessierungsansätze aufgezeigt, um die Resonanzeffekte zu reduzieren.

Die abschließenden Simulationsergebnisse der monatlichen Ermittlung eines globalen Schwerefeldes mit den Basisszenarien beinhalten die drei Hauptfehlerbeiträge, Instrumentenfehler und zeitliches Aliasing von Gezeiten- und Nicht-Gezeitenanteilen. Damit die NGGM von den hohen Instrumentengenauigkeiten profitieren kann, müssen die hochfrequenten Signalanteile und damit die Effekte von zeitlichem Aliasing reduziert werden. Hierfür werden zwei Ansätze beschrieben. Einer ist ein klassischer Ansatz, wie er auch für die GRACE-Prozessierung verwendet wird. Die hochfrequenten Signalanteile in der Atmosphäre und den Ozeanen werden mit a priori Modellinformationen reduziert. Ein weiterer Ansatz beinhaltet die Mitschätzung von kurzperiodischen Schwerefeldparametern. Diese Option wird im Hinblick auf die Anwendung mit einem Doppelpaar validiert.

Die beste monatliche globale Schwerefeldermittlung wird mit den Doppelpaaren aus den Basisszenarien in niedriger Flughöhe (300 km) erreicht. Die geforderte monatliche Genauigkeit der NGGM kann aber nur erreicht werden, wenn die Effekte von zeitlichem Aliasing um einen Faktor zwischen 30 und 60 reduziert werden. Mit dieser Reduktion erreichen die drei besten NGGM low-low SST Doppelpaare mit polaren Paaren in 300, 360 und 420 km Flughöhe kombiniert mit dem 70° geneigten Paar eine Genauigkeit des globalen Geoids von 0.01 mm bei 500 km räumlicher Auflösung und 0.4 mm bei 150 km räumlicher Auflösung.

Die NGGM hat große wissenschaftliche und gesellschaftliche Bedeutung. Sowohl mit erhöhter räumlicher und zeitlicher Auflösung, als auch mit erhöhter Genauigkeit des globalen Erdschwerefeldes wird das Verständnis einer Vielzahl an Prozessen im System Erde verbessert werden. Die wissenschaftlichen Anforderungen, die mit der NGGM erfüllt werden können, liegen in Bereichen der Geodäsie, Ozeanographie, Hydrologie, Glaziologie und der Physik der festen Erde. Zum Beispiel können die Anforderungen für die Vereinheitlichung von Höhensystemen, das Grundwasser, die postglaziale Landhebung und die Eismassenbilanz mit der NGGM erfüllt werden.

# Contents

<b>Abstract</b>	<b>iii</b>
<b>Zusammenfassung</b>	<b>v</b>
<b>Abbreviations</b>	<b>ix</b>
<b>1 Introduction</b>	<b>1</b>
1.1 Motivation . . . . .	1
1.2 Subject of this Thesis . . . . .	4
<b>2 Theory</b>	<b>7</b>
2.1 The Earth's Gravity Field in Spherical Harmonics . . . . .	7
2.2 Least Squares Adjustment . . . . .	9
2.3 Satellite Orbits . . . . .	10
2.3.1 Repeat Cycles . . . . .	12
2.3.2 Spatio-Temporal Sampling . . . . .	13
2.4 Simulation Environment . . . . .	15
2.4.1 Semi-analytical Approach . . . . .	15
2.4.2 Linear Closed-loop Approach . . . . .	17
2.4.3 Simulation Approach Comparison . . . . .	19
<b>3 From Science Requirements to Mission Objectives</b>	<b>25</b>
3.1 Translation to Geoid Heights . . . . .	25
3.2 Translation to Monthly Resolution . . . . .	27
3.3 Mission Objectives . . . . .	30
<b>4 Basic Scenarios and Instrument Requirements</b>	<b>33</b>
4.1 Basic Scenarios . . . . .	33
4.1.1 Double pair (Bender-type) . . . . .	34
4.1.2 Pendulum . . . . .	35
4.1.3 Combination of low-low SST and radial SGG . . . . .	37
4.2 Instrument Requirements . . . . .	38
<b>5 Other Error Contributions</b>	<b>43</b>
5.1 Star Sensors . . . . .	43
5.2 GNSS Positioning . . . . .	46
5.3 Tone Errors . . . . .	47

<b>6</b>	<b>Temporal Aliasing</b>	<b>51</b>
6.1	Optimal Sampling regarding Temporal Aliasing . . . . .	52
6.2	Spectral Analysis of Non-tidal Mass Variations . . . . .	57
<b>7</b>	<b>Optimal Orbits regarding Temporal Aliasing</b>	<b>61</b>
7.1	Spherical Harmonic Order Resonances . . . . .	61
7.2	GRACE Resonances . . . . .	62
7.3	Order Resonance Reduction . . . . .	64
7.3.1	Weighting of Double Pairs . . . . .	64
7.3.2	Single Pair Regularization . . . . .	67
<b>8</b>	<b>Proposed Mission Scenarios</b>	<b>71</b>
8.1	Low Resolution Gravity Retrieval . . . . .	73
8.1.1	Temporal Aliasing from Non-Tidal Variations . . . . .	73
8.1.2	Temporal Aliasing from Ocean Tides . . . . .	76
8.2	High Temporal Resolution Gravity Retrieval . . . . .	80
8.3	High Spatial Resolution Gravity Retrieval . . . . .	84
8.4	Comparison with Mission Objectives . . . . .	87
<b>9</b>	<b>Summary, Conclusions, and Outlook</b>	<b>93</b>
	<b>Bibliography</b>	<b>97</b>
	<b>Acknowledgements</b>	<b>101</b>

# Abbreviations

ACC	Accelerometer
AOHIS	Atmosphere, Ocean, Hydrology, Ice, Solid Earth
AR	Auto-Regressive
ASD	Amplitude Spectral Density
CHAMP	Challenging Minisatellite Payload
CIRA	COSPAR International Reference Atmosphere
CoM	Center of Mass
COSPAR	Committee On Space Research
CSR	Center for Space Research (University of Texas at Austin)
EIGEN	European Improved Gravity model of the Earth by New techniques
ESA	European Space Agency
GEO	Geostationary satellite
GETRIS	Geodesy and Time Reference In Space
GFZ	Deutsches Geoforschungszentrum (Hemholtz-Zentrum Potsdam)
GNSS	Global Navigation Satellite System
GOCE	Gravity and Ocean Circulation Explorer
GOCO	Gravity Observation Combination
GRACE	Gravity Recovery and Climate Experiment
GRACE-FO	GRACE Follow-On
GRS	Geodetic Reference System
IERS	International Earth Rotation and Reference System Service
ITSG	Institut für Theoretische Geodäsie und Satellitengeodäsie (TU Graz)
JPL	Jet Propulsion Laboratory (California Institute of Technology)
LCLA	Linear Closed-Loop Approach
LEO	Low Earth Orbiter
LoS	Line of Sight
LRI	Laser Ranging Interferometer
LSA	Least Squares Adjustment
MA	Moving-Average
MO	Mission Objectives
NGGM	Next Generation Gravity Mission
OTD	Ocean tide model difference
PSD	Power Spectral Density
RMS	Root Mean Square
SANA	Semi-Analytical Approach
SGG	Satellite Gravity Gradiometry
SH	Spherical Harmonic
SR	Science Requirements
SST	Satellite-to-Satellite tracking
VCM	Variance Covariance Matrix



# 1 Introduction

## 1.1 Motivation

The Earth's gravity field is an important quantity to be observed in presence and future. Especially the monitoring of the temporal changes of the mass distributions in the system Earth requires continuous and long time series. Several geophysical disciplines derive various information from the Earth's gravity field. Three important examples of mass variations shall be named here, i.e. continental hydrology, ice masses and ocean circulation.

Besides terrestrial and airborne gravimetry, satellite observations play an important role for gravity field determination. In comparison with terrestrial and airborne gravimetry, the greatest advantage of satellite missions is the ability of providing global gravity field models with homogeneous accuracy. In contrast to terrestrial measurements the observations taken in satellite altitudes of usually 200 to 500 km contain less signal content. Another challenge for global mass variation estimates from satellite observations is signal separation. Gravitational satellite observations are integrated measurements of the sum of the masses in all sub-systems of the Earth (solid Earth, ocean, continental hydrology, ice and atmosphere). Therefore it is necessary to separate the target signal, e.g. continental hydrology, from these measurements. One possibility to do so is the subtraction of model information representing all the other signal contents. But then of course the result can not be of higher accuracy than the models used in this separation step. Nevertheless, global and long term monitoring of the Earth's gravity field needs satellite missions.

Three satellite gravity field missions have been successfully launched. The first was CHALLENGING Mini-satellite Payload (CHAMP) launched in 2000 (Reigber et al., 2000) and ended in 2010 after more than 10 years in orbit. Besides the CHAMP mission tasks related to the Earth's magnetic and electrical fields its primary mission goal was the improvement of the estimation of the Earth's gravity field. For this CHAMP carried an accelerometer measuring the non-conservative forces acting on it and a Global Navigation Satellite System (GNSS) receiver for precise positioning. From these Satellite-to-Satellite tracking (SST) observations in high-low mode gravity field models have been estimated down to a spatial resolution of approximately 170 km (Weigelt et al., 2013).

*Table 1.1: Basic mission parameters of CHAMP, GRACE and GOCE and one example of current static satellite-only gravity field models.*

	CHAMP	GRACE	GOCE
Altitude	450 km (decaying to 300 km)	500 km (decaying to 400 km)	260 km (decaying to 230 km in 4 steps)
Inclination	87°	89°	97° (sun-synchronous)
Measurement concept	high-low SST	high-low SST and low-low SST	high-low SST and SGG
Inter satellite distance	-	200 km	-
Gravity field model	ULux_CHAMP2013s Weigelt et al. (2013)	GGM05S Tapley et al. (2013)	CO_CONS_GCF_2_TIM_R5 Brockmann et al. (2014)

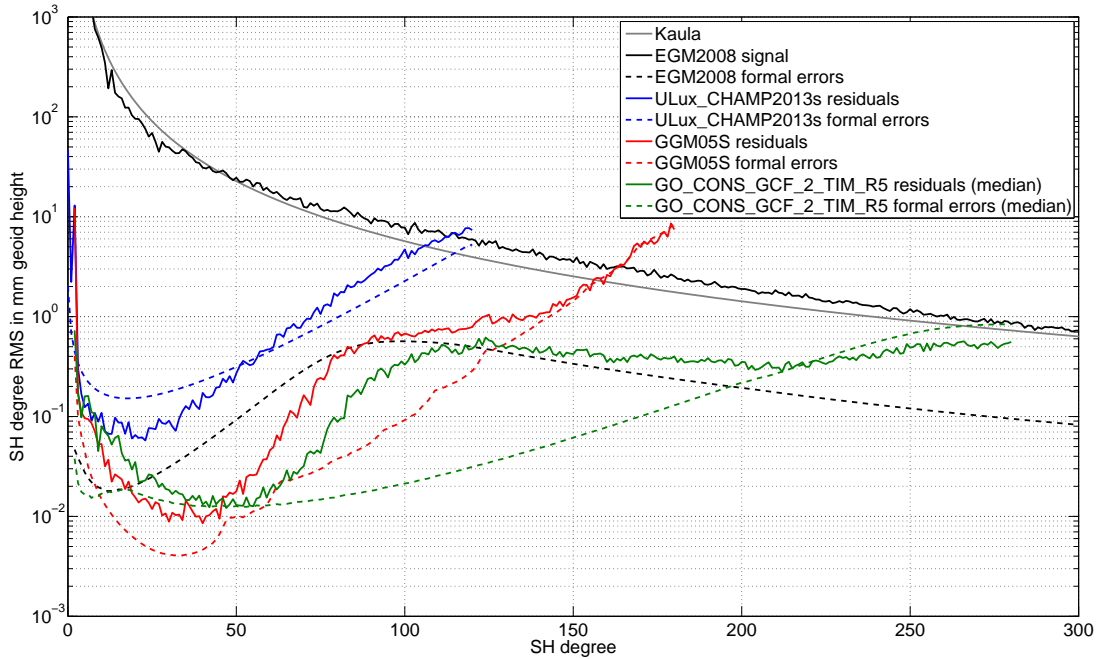


Figure 1.1: SH degree RMS for current satellite-only models compared with EGM2008 (Pavlis et al., 2012). For the GOCE model the median is used instead of the RMS because of the polar gap.

The Gravity Recovery and Climate Experiment (GRACE) mission has been in orbit now for nearly 13 years (Tapley et al., 2004). Its main focus is the observation of the temporal variations of the Earth’s gravity field. It is sensitive to such variations with a spatial resolution of approximately 300 km and a temporal resolution between 10 and 30 days (Tapley et al., 2013). The static gravity field is observed with GRACE down to a resolution of approximately 120 km. The key instrument to reach this increased accuracy compared to CHAMP is a microwave inter-satellite ranging instrument. It measures the biased ranges between two twin satellites in polar orbits with a mean along-track separation of 200 km (SST in low-low mode). As CHAMP both GRACE satellites have an accelerometer and GNSS receiver on board.

The third dedicated gravity satellite mission in orbit was the Gravity and Ocean Circulation Explorer (GOCE). After the launch of GOCE in March 2009 the mission phase ended in November 2013. Besides precise position and attitude observations the low orbit altitude of less than 260 km and the satellite gravity gradiometer are the key characteristics of this mission. The gradiometer consists of 6 accelerometers placed on three orthogonal axes around the center of mass (CoM) of the satellite (Drinkwater et al., 2003). With these instruments the second derivatives of the Earth’s gravitational potential (gravity gradients) can be measured. This is why this measurement concept is called satellite gravity gradiometry (SGG). The static gravity field can be estimated with GOCE down to a spatial resolution of approximately 80 km (Brockmann et al., 2014). Table 1.1 shows the basic mission parameters of CHAMP, GRACE and GOCE.

In Fig. 1.1 the three static gravity field models listed in Tab. 1.1 are compared with the combined gravity field model EGM2008 (Pavlis et al., 2012) in terms of Spherical Harmonic (SH) degree RMS in geoid heights (cf. Sec. 2.1). As GOCE-only models suffer from the polar gap (inclination of  $97^\circ$ ), the median is used instead of the RMS for CO\_CONS\_GCF\_2\_TIM\_R5. For each model the formal errors of the SH coefficients and the residuals with respect to (wrt.) EGM2008 are shown. Both consist of error information of the model per SH degree  $l$ . Comparing the three models among each other, two main characteristics of gravity field determination from satellite observations become visible. Signal attenuation with satellite altitude increases the errors especially in high SH degrees, i.e. high spatial resolution. The observation type affect this increase as well. As GOCE has the lowest orbit and measures the second derivatives of the gravitational potential the errors of CO\_CONS\_GCF\_2\_TIM\_R5

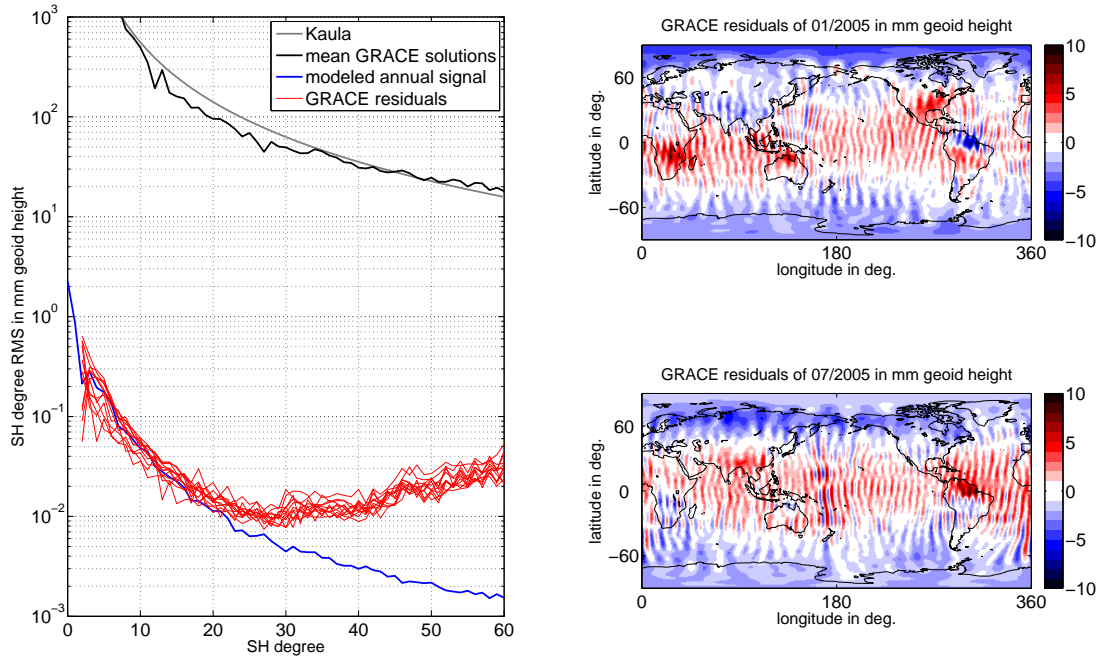


Figure 1.2: Left: SH degree RMS in mm geoid height for monthly CSR Release 05 solutions compared with modeled annual mass variations (hydrology, ice and solid Earth of Gruber et al. (2011)) in 2005. The GRACE residuals are computed with respect to the mean of the monthly solutions in 2005. The annual mass variations are represented by the absolute annual amplitude estimated from the model with 6 hour sampling. Right: unfiltered GRACE residuals of January (top) and July (bottom) in mm geoid height up to  $l_{\max} = 60$ .

increase less strongly in high degrees compared to ULux\_CHAMP2013s and GGM05S. Furthermore, low-low SST seems to be more sensitive to low SH degrees than SGG. In a combined gravity field model using GRACE and GOCE data, GRACE dominates the low SH degrees and GOCE contributes significantly above  $l = 100$  and dominates above  $l = 150$  (Pail et al., 2010; Brockmann et al., 2014). The differences between the formal errors and the residuals indicate where the analysed models contains new signal compared to EGM2008. Hence, with respect to EGM2008 GOCE contributed mainly to  $l > 60$ . The formal errors of EGM2008 support this assumption, because the residuals of GGM05S and CO\_CONS\_GCF\_2\_TIM\_R5 show similar behaviour for  $l > 100$ .

With GRACE also temporal variations of the Earth's gravity field can be observed. The comparison of current monthly GRACE solutions with modeled mass variations give an idea of the resolution, to which GRACE is sensitive to mass variations. Figure 1.2 (left) shows such a comparison of the monthly CSR Release 05 solutions (Tapley et al., 2013) and a mass variation model (Gruber et al., 2011) in terms of SH degree RMS. The residuals are computed with respect to the mean of the monthly solutions in 2005. The annual mass variations are represented by the absolute annual amplitude estimated from the 6 hour sampled model. The residuals consist of the mean monthly mass variations and of the GRACE errors. The GRACE gravity fields suffer not only from instrument errors but also from temporal aliasing. Temporal aliasing due to under sampling of high-frequency signal contents from both the observed signals and from background model errors. This effect is pronounced by the not optimal observation geometry of the GRACE mission. Both GRACE satellites in in-line formation fly in nearly the same polar orbit only separated by the mean anomaly. Except for the polar areas the line of sight between the two satellites is north-south directed leading to anisotropic errors. A typical error characteristic of GRACE can be seen in the right images in Fig. 1.2. Global geoid height residuals with respect to the mean are shown for two months in 2005 (top: January, bottom: July). The annual variations of the large continental hydrological mass variations are visible when comparing the two months (e.g. the Amazon and Congo region). These signals are superimposed with errors of north-south directed striping patterns. Without any post-processing the mass variations can be estimated significantly up to

$l = 30$  (approximately 700 km spatial resolution). Reducing the striping patterns with post-processing filtering strategies, this resolution can be increased to 300 km (Tapley et al., 2013).

The next gravity satellite mission in orbit will be GRACE Follow-On (GRACE-FO) with a proposed launch date in 2017 (Sheard et al., 2012). It is planned to have the same orbit configuration as GRACE. An improved gravity retrieval performance is expected with respect to (wrt.) GRACE, because in addition to the inter-satellite microwave ranging instrument GRACE-FO will carry an inter-satellite laser ranging interferometer (LRI) with an improved measurement accuracy. Nevertheless the microwave instrument is the primary instrument, the LRI is included as a demonstrator experiment (Sheard et al., 2012).

Comprehensive discussions of future gravity satellite missions from a technological and geodetic point of view can be found in Reubelt et al. (2014), Gruber et al. (2014), Wiese et al. (2012), Elsaka (2012) and Iran Pour (2013). The findings of this thesis are partly based on the results of these studies. New insight is given for example in the definition of mission objectives from science requirements and the optimization of the orbit choice regarding error effects from temporal aliasing.

## 1.2 Subject of this Thesis

In this thesis, issues of a Next Generation Gravity Mission (NGGM) are discussed. Most of the technical aspects like instrument accuracies refer to a launch date around 2030. This NGGM aims to observe the Earth's gravity field and especially its temporal variations. The conclusions are drawn mainly based on the results of two types of gravity retrieval simulations (Sec. 2.4). Using the semi-analytical approach (Sneeuw, 2000) spectral instrument noise characteristics are propagated onto the SH spectrum (Sec. 2.4.1). The results of this approach used in this thesis are formal errors of SH coefficients. The second numerical simulation environment is a numerical closed-loop based on full normal equation matrices (Sec. 2.4.2).

The main results are optimal virtual constellations of NGGMs (Chap. 8). The optimization focuses on the best fulfilment of science requirements. Therein different functionals of the gravity potential like geoid heights and gravity anomalies are analysed. This thesis focuses on geodetic aspects, but the proposed concepts satisfy technical conditions of a NGGM with a launch date around 2030 as well.

After explaining the theoretical principles needed for this thesis (Chap. 2), the mission objectives are derived from a consolidated set of science requirements (Chap. 3). The mission objectives contain maximum cumulative geoid errors for specific spatial and temporal resolution. Other mission requirement aspects are mission duration, groundtrack coverage and sub-cycle assessment. In Chap. 4 based on semi-analytical simulations instrument requirements for selected basic scenarios are derived. These requirements in terms of amplitude spectral densities assure the reference scenarios to be sensitive to the target signals with the required temporal and spatial resolution.

The scenario performance simulations are based on instrument noise assumptions for the key instruments of the different observing techniques. For a GRACE-like low-low SST mission, for example, the main noise contributions for the gravitational observations come from the microwave ranging instrument and from the accelerometer. In Chap. 5 the gravity retrieval error contributions of other sources are simulated and discussed. Besides star sensor and GNSS-positioning sensor errors the effects of so-called tone errors are analysed. Tone errors mainly result from temperature variations within the satellite leading to harmonic signals with the orbital frequency, i.e.  $(\text{revolution time})^{-1}$  and integer multiples of it. With closed loop simulations requirements for the tone error amplitudes for the NGGM can be derived (Gruber et al., 2014).

Current monthly GRACE gravity fields (and most likely for short term GRACE-FO solutions) suffer from temporal aliasing from background model errors. In the standard GRACE processing the high frequency signals from ocean tides and non-tidal oceanic and atmospheric mass variations are reduced

---

from the GRACE observations using model information (Tapley et al., 2013). The errors of such state-of-the-art models restrict the quality of monthly GRACE solutions to lower accuracies than it could be expected from the instrument accuracy. In Chap. 6 the mechanism of temporal aliasing is described in general. And based on model error assumptions the effects are analysed in both, the spectral and spatial domain. One of the main characteristics of temporal aliasing are resonances on specific SH order bands (Murböck et al., 2014). As these bands mainly depend on the orbital altitude, optimal altitude bands regarding temporal aliasing can be derived (Chap. 7). Herein it is focused on how double pair constellations can help to reduce temporal aliasing effects. Special emphasis is put on optimal SH order dependent weighting.

Finally, mission concepts for the reference scenarios are set up (Chap. 8), taking into account the findings in this thesis, to fulfil the science requirements. Besides a validation of the gravity field retrieval, technical and financial aspects are discussed as well. This chapter directly leads to the overall summary and conclusions including an outlook to additional scientific aspects (Chap. 9).



## 2 Theory

### 2.1 The Earth's Gravity Field in Spherical Harmonics

The Earth's gravity field is defined by its gravitational potential. The gradient of this potential gives the gravitational force. Together with the centrifugal force due to the Earth's rotation this is called gravity (Heiskanen and Moritz, 1967). Regarding the Earth as a solid body its gravitational potential  $V$  can be formulated as an integral over the entire Earth (Heiskanen and Moritz, 1967)

$$V = G \iiint_{\text{Earth}} \frac{dM}{\rho}. \quad (2.1)$$

Here,  $G$  is the Newtonian constant of gravitation with a value of  $6.674 \cdot 10^{-11} \text{m}^3 \text{kg}^{-1} \text{s}^{-2}$  (Mohr et al., 2012),  $dM$  is an element of mass, and  $\rho$  is the distance between  $dM$  and the attracted point. Outside the attracting masses the gravitational potential is a harmonic function and meets Laplace's equation  $\Delta V = 0$ . Furthermore, any harmonic function is continuous and has continuous derivatives of any order (Heiskanen and Moritz, 1967).

The term  $1/\rho$  in Eq. (2.1) can be expressed with Legendre polynomials  $P_l(\cos \psi)$  of degree  $l$  with the central angle  $\psi$  between  $dM$  and the attracted point leading to (Torge, 2003)

$$\frac{1}{\rho} = \frac{1}{R} \sum_{l=0}^{\infty} \left(\frac{R}{r}\right)^{l+1} P_l(\cos \psi). \quad (2.2)$$

Through the addition theorem  $P_l(\cos \psi)$  can be expressed in a geocentric spherical reference frame with coordinates longitude  $\lambda$  and co-latitude  $\theta$ . Thereby associated Legendre polynomials of the first kind  $P_{lm}(\cos \theta)$  (degree  $l$  and order  $m$ ) are used which are order  $m$  derivatives of  $P_l(\cos \psi)$  with respect to  $\cos \theta$ . This together with Eq. (2.2) gives the Spherical Harmonic (SH) expansion of the reciprocal distance  $1/\rho$ . With SH base functions the Earth's gravitational potential  $V$  can be expressed by the series expansion (Heiskanen and Moritz, 1967)

$$V(r, \theta, \lambda) = \frac{GM}{R} \sum_{l=0}^{\infty} \left(\frac{R}{r}\right)^{l+1} \sum_{m=0}^l \bar{P}_{lm}(\cos \theta) (\bar{C}_{lm} \cos m\lambda + \bar{S}_{lm} \sin m\lambda), \quad (2.3)$$

with

$(r, \theta, \lambda)$	the spherical coordinates (radius, co-latitude, longitude),
$GM$	the product of gravitational constant and the Earth's mass,
$R$	the Earth's equatorial radius,
$(l, m)$	the SH degree and order,
$\bar{P}_{lm}(\cos \theta)$	the fully normalized associated Legendre functions and
$(\bar{C}_{lm}, \bar{S}_{lm})$	the fully normalized SH coefficients.

If not denoted otherwise, for  $R$ ,  $GM$  and also for the other two defining physical constants of a Geodetic Reference System (GRS), the Earth's flattening term  $J_2$  and the angular velocity of rotation  $\omega_E$ , the following values of GRS80 are used:

$$\begin{aligned} R &= 6.378137 \cdot 10^6 \text{ m} \\ GM &= 3.986005 \cdot 10^{14} \frac{\text{m}^3}{\text{s}^2} \\ J_2 &= 1.08263 \cdot 10^{-3} \\ \omega_E &= 7.292115 \cdot 10^{-5} \frac{\text{rad}}{\text{s}}. \end{aligned} \quad (2.4)$$

A short notation for SH coefficients and base functions using complex valued quantities is also used in this thesis. Hence, the gravitational potential is (Sneeuw, 2000)

$$V(r, \theta, \lambda) = \frac{GM}{R} \sum_{l=0}^{\infty} \left(\frac{R}{r}\right)^{l+1} \sum_{m=-l}^l \bar{K}_{lm} \bar{Y}_{lm}(\theta, \lambda) \quad (2.5)$$

with

$$\bar{Y}_{lm}(\theta, \lambda) = \bar{P}_{lm}(\cos \theta) e^{im\lambda} \quad (2.6)$$

and the SH coefficients  $\bar{K}_{lm}$  associated with  $\bar{Y}_{lm}(\theta, \lambda)$ . For  $m < 0$  the fully normalized Legendre functions are  $(-1)^m \bar{P}_{l, -m}(\cos \theta)$ .

Thereby it is

$$\bar{Y}_{lm}(\theta, \lambda) = \bar{P}_{|m|}(\cos \theta) \begin{cases} \cos m\lambda, & m \geq 0 \\ \sin |m|\lambda, & m < 0 \end{cases} \quad (2.7)$$

and the relation for the coefficients reads

$$\bar{K}_{lm} = \begin{cases} (-1)^m (\bar{C}_{lm} - i\bar{S}_{lm}) / \sqrt{2}, & m > 0 \\ \bar{C}_{lm}, & m = 0 \\ (\bar{C}_{lm} + i\bar{S}_{lm}) / \sqrt{2}, & m < 0 \end{cases} \quad (2.8)$$

The normalization is defined in a way, that the integral over the surface of a unit sphere of the squares  $\bar{Y}_{lm}^2$  is  $4\pi$ . Furthermore, the SH base functions fulfil orthogonality, i.e.

$$\frac{1}{4\pi} \iint_{\sigma} \bar{Y}_{l,m} \bar{Y}_{l',m'}^* d\sigma = \delta_{ll'} \delta_{mm'} \quad (2.9)$$

In order to quantify the signal/error in a set of SH coefficients per SH degree and SH order different quantities are used. Equations (2.10) and (2.11) give the notations and formulas for the unit-less quantities for SH degree and order respectively. The variances (var), amplitudes (amp) and cumulative amplitudes (cum) represent full signal/error information for all coefficients of each degree/order. And the RMS (rms) and median (med) values represent the information per degree/order and per coefficient. The measures are formulated for SH coefficients  $\{\bar{C}_{lm}, \bar{S}_{lm}\}$ , but are used analogously for their error information  $\{\sigma_{\bar{C}_{lm}}, \sigma_{\bar{S}_{lm}}\}$  as well. Except the SH degree/order variances each of these measures can be expressed in terms of geoid heights by applying a factor  $R$ .

$$\begin{aligned} \kappa_{\text{var}}(l) &= \sum_{m=0}^l (\bar{C}_{lm}^2 + \bar{S}_{lm}^2) \\ \kappa_{\text{amp}}(l) &= \sqrt{\kappa_{\text{var}}(l)} \\ \kappa_{\text{rms}}(l) &= \sqrt{\frac{\kappa_{\text{var}}(l)}{2l+1}} \\ \kappa_{\text{med}}(l) &= \text{median}_l (|\bar{C}_{lm}|, |\bar{S}_{lm}|) \quad , \text{ for } 0 \leq m \leq l \\ \kappa_{\text{cum}}(l) &= \sqrt{\sum_{l_{\text{min}}}^l \kappa_{\text{var}}(l)} \end{aligned} \quad (2.10)$$

$$\begin{aligned}
\kappa_{\text{var}}(m) &= \sum_{l=m}^{l_{\text{max}}} (\bar{C}_{lm}^2 + \bar{S}_{lm}^2) \\
\kappa_{\text{amp}}(m) &= \sqrt{\kappa_{\text{var}}(m)} \\
\kappa_{\text{rms}}(m) &= \sqrt{\frac{\kappa_{\text{var}}(m)}{2^{\min(m,1)} (l_{\text{max}} + 1 - m)}} \\
\kappa_{\text{med}}(m) &= \text{median}_m (|\bar{C}_{lm}|, |\bar{S}_{lm}|) \quad , \text{ for } m \leq l \leq l_{\text{max}} \\
\kappa_{\text{cum}}(m) &= \sqrt{\sum_{m_{\text{min}}}^m \kappa_{\text{var}}(m)}
\end{aligned} \tag{2.11}$$

## 2.2 Least Squares Adjustment

Equation (2.3) is the basis of the functional models of global gravity field determination. The goal is the determination of all SH coefficients  $\bar{C}_{lm}$  and  $\bar{S}_{lm}$  up to a maximum SH degree  $l_{\text{max}}$  from gravitational observations (various functionals of the gravitational potential). This is done in a least squares adjustment (LSA) minimizing the squared residuals in the  $L_2$ -norm (Gauss-Markov model).

In a LSA parameters  $\mathbf{x}$  (number of parameters  $u$ ) are estimated from observations  $\mathbf{l}$  (number of observations  $n > u$ ) based on a functional and a stochastic model resulting in the parameter estimates  $\hat{\mathbf{x}}$ . The functional model  $\mathbf{l} + \hat{\mathbf{v}} = \mathbf{f}(\hat{\mathbf{x}})$  gives the relation between  $\hat{\mathbf{x}}$  and  $\hat{\mathbf{l}} = \mathbf{l} + \hat{\mathbf{v}}$  with the residuals  $\hat{\mathbf{v}}$ . In this context the hat  $\hat{\cdot}$  marks an estimated quantity. The stochastic model is described with the first two statistical moments of  $\mathbf{v}$ . The expectation value of  $\mathbf{v}$  is assumed to be zero, i.e.  $E\{\mathbf{v}\} = 0$ . The variance covariance matrix (VCM) of  $\mathbf{v}$  ( $\mathbf{Q}_{\mathbf{v}\mathbf{v}}$ ) is the expectation value of  $\mathbf{v}\mathbf{v}^T$ , i.e.  $D\{\mathbf{v}\} = E\{\mathbf{v}\mathbf{v}^T\} = \mathbf{Q}_{\mathbf{v}\mathbf{v}}$ . Thereby, normal distribution is assumed for  $\mathbf{v}$ .

The a priori variance covariance matrix (VCM) of the observations is  $\mathbf{Q}_{\mathbf{ll}}$  which is the inverse of the weighting matrix  $\mathbf{P} = \mathbf{Q}_{\mathbf{ll}}^{-1}$ . Hence, minimizing  $\mathbf{v}^T \mathbf{P} \mathbf{v}$ , a best linear unbiased estimate of  $\mathbf{x}$  is given by

$$\hat{\mathbf{x}} = (\mathbf{A}^T \mathbf{P} \mathbf{A})^{-1} \mathbf{A}^T \mathbf{P} \mathbf{l} \tag{2.12}$$

with the design matrix  $\mathbf{A}$  containing the partial derivatives  $\partial f(\mathbf{x}) / \partial \mathbf{x}$ . This is the basic formula of LSA. It has to be modified, for example, when conditions in general or conditions between the unknowns are introduced. The inverse of the normal matrix  $\mathbf{A}^T \mathbf{P} \mathbf{A}$  is the a priori VCM of the parameters

$$\mathbf{Q}_{\hat{\mathbf{x}}\hat{\mathbf{x}}} = (\mathbf{A}^T \mathbf{P} \mathbf{A})^{-1}. \tag{2.13}$$

The residuals read

$$\hat{\mathbf{v}} = \mathbf{A} \hat{\mathbf{x}} - \mathbf{l} \tag{2.14}$$

and the unit weight variance is

$$\hat{\sigma}_0^2 = \frac{\hat{\mathbf{v}}^T \mathbf{P} \hat{\mathbf{v}}}{n - u}. \tag{2.15}$$

With  $\hat{\sigma}_0^2$  the formal VCMs  $\mathbf{Q}$  of the observations, the unknowns and the residuals are scaled to get the VCMs  $\hat{\Sigma}$ .

$$\begin{aligned}
\hat{\Sigma}_{\hat{\mathbf{x}}\hat{\mathbf{x}}} &= \hat{\sigma}_0^2 \mathbf{Q}_{\hat{\mathbf{x}}\hat{\mathbf{x}}} = \hat{\sigma}_0^2 (\mathbf{A}^T \mathbf{P} \mathbf{A})^{-1} \\
\hat{\Sigma}_{\hat{\mathbf{v}}\hat{\mathbf{v}}} &= \hat{\sigma}_0^2 \mathbf{Q}_{\hat{\mathbf{v}}\hat{\mathbf{v}}} = \hat{\sigma}_0^2 (\mathbf{Q}_{\mathbf{ll}} - \mathbf{A} \mathbf{Q}_{\hat{\mathbf{x}}\hat{\mathbf{x}}} \mathbf{A}^T) \\
\hat{\Sigma}_{\mathbf{ll}} &= \hat{\sigma}_0^2 \mathbf{Q}_{\mathbf{ll}} = \hat{\sigma}_0^2 \mathbf{A} \mathbf{Q}_{\hat{\mathbf{x}}\hat{\mathbf{x}}} \mathbf{A}^T
\end{aligned} \tag{2.16}$$

Having more than one set of uncorrelated observations, e.g.  $\mathbf{l}_1$  and  $\mathbf{l}_2$ , the unknown parameters  $\mathbf{x}$  are estimated in a combination at normal equation level with the corresponding design and weighting matrices evaluating

$$\hat{\mathbf{x}} = (\mathbf{A}_1^T \mathbf{P}_1 \mathbf{A}_1 + \mathbf{A}_2^T \mathbf{P}_2 \mathbf{A}_2)^{-1} (\mathbf{A}_1^T \mathbf{P}_1 \mathbf{l}_1 + \mathbf{A}_2^T \mathbf{P}_2 \mathbf{l}_2). \quad (2.17)$$

In reality  $\mathbf{Q}_{\mathbf{l}}$  is not known. The simplest case are independent and equally accurate observations with standard deviation  $\sigma_1$ . Then  $\mathbf{Q}_{\mathbf{l}}$  is the identity matrix scaled with  $\sigma_1^{-2}$ . It is also possible to approximate  $\mathbf{Q}_{\mathbf{l}}$  in an iterative LSA analysing the residuals  $\hat{\mathbf{v}}$ .

An alternative approach to model  $\mathbf{Q}_{\mathbf{l}}$  or the inverse of it as weighting matrix  $\mathbf{P}$  is the use of autoregressive moving-average (ARMA) filters (Schuh, 1996; Siemes, 2008). In this context, the observations and the columns of the design matrix are filtered in order to decorrelate the system. In general, a digital filter represented by filter coefficients  $a_k$  and  $b_k$  is applied to a series of numbers  $x[j]$  with  $j = \{1, 2, \dots, J\}$  resulting in the filtered series (Schuh, 1996)

$$\bar{x}[j] = \frac{1}{a_0} \left( \sum_{k=0}^{K_b} b_k x[j-k] - \sum_{k=1}^{K_a} a_k \bar{x}[j-k] \right). \quad (2.18)$$

If  $K_a = 0$ , it is a moving average (MA) filter ( $K_b > 0$ ), if  $K_b = 0$  it is an auto-regressive (AR) filter ( $K_a > 0$ ) and if  $K_a > 0$  and  $K_b > 0$  it is an ARMA filter. The complex valued frequency response of the filter is given by

$$H(e^{i\omega}) = \frac{\sum_{k=0}^{K_b} b_k e^{-ik\omega}}{\sum_{k=0}^{K_a} a_k e^{-ik\omega}}. \quad (2.19)$$

The filtering can also be represented by the multiplication by matrix  $\mathbf{F}$ . The filtered Eq. (2.14) is

$$\mathbf{F}\hat{\mathbf{v}} = \mathbf{F}\mathbf{A}\hat{\mathbf{x}} - \mathbf{F}\mathbf{l}. \quad (2.20)$$

and  $\mathbf{F}$  is chosen in such a way, that  $\mathbf{F}^T \mathbf{F}$  approximates  $\mathbf{P}$ . Then Eq. (2.12) becomes

$$\begin{aligned} \hat{\mathbf{x}} &= (\mathbf{A}^T \mathbf{F}^T \mathbf{F} \mathbf{A})^{-1} \mathbf{A}^T \mathbf{F}^T \mathbf{F} \mathbf{l} \\ \hat{\mathbf{x}} &= (\bar{\mathbf{A}}^T \bar{\mathbf{A}})^{-1} \bar{\mathbf{A}}^T \bar{\mathbf{l}} \end{aligned} \quad (2.21)$$

with the filtered observations  $\bar{\mathbf{l}} = \mathbf{F}\mathbf{l}$  and the filtered design matrix  $\bar{\mathbf{A}} = \mathbf{F}\mathbf{A}$ .

There are different ways to estimate the filter in order to decorrelate  $\mathbf{l}$ . This is done in the spectral domain. The coefficients  $b_k$  and  $a_k$  are chosen in a way, that the absolute frequency response of the filter approximates the inverse of the amplitude spectrum of the noise in  $\mathbf{l}$ . As mentioned before, this noise is not known in real gravity field determination from satellite observations. In a simulation environment of course it is, and in reality it can be estimated iteratively from the analysis of the residuals of the LSA. An example with such a stochastic modeling is shown in Sec. 2.4.3 comparing the two simulation procedures.

## 2.3 Satellite Orbits

The orbit trajectory of a satellite is determined by the integration of all forces acting on the satellite. These forces can be divided into gravitational (conservative) forces mainly from Earth, Moon and Sun (incl. solid Earth and ocean tides), and non-gravitational forces, e.g. atmospheric drag and solar and Earth radiation. The magnitudes of the different forces depend mainly on the orbital altitude of the satellite. For Low Earth orbiters (LEO) in altitudes between 200 and 500 km the largest forces are due to  $\bar{C}_{00}$  and  $\bar{C}_{20}$  of the Earth's gravity field with average magnitudes of 9 m/s<sup>2</sup> ( $\bar{C}_{00}$ ) and 0.1 m/s<sup>2</sup> ( $\bar{C}_{20}$ ), respectively. Depending on solar activity atmospheric drag reaches 10<sup>-7</sup> to 10<sup>-5</sup> m/s<sup>2</sup> for LEOs (cf. Sec. 5.1).

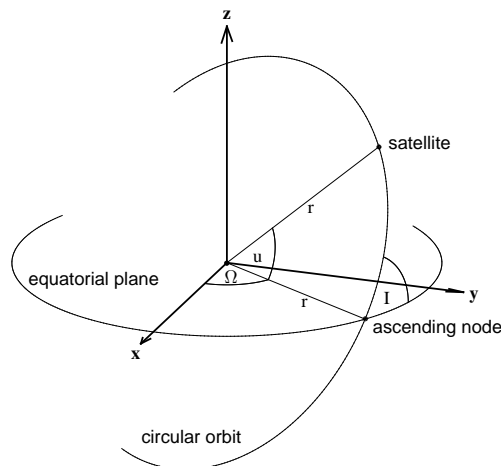


Figure 2.1: Circular satellite orbit in space-fixed frame with Keplerian elements  $r$ ,  $I$ ,  $\Omega$  and  $u$ .

In this thesis satellite orbits are approximated by only taking into account the  $\bar{C}_{00}$  and  $\bar{C}_{20}$  terms leading to precessing ellipsoidal orbits. Based on Kepler's three laws of planetary motion such elliptic orbits are modeled by six Keplerian elements. The six elements are

- the semi-major axis  $a$ ,
- the eccentricity  $e$ ,
- the inclination  $I$ ,
- the right ascension of the ascending node  $\Omega$ ,
- the argument of the perigee  $\omega$ , and
- the mean anomaly  $M$ .

The  $\bar{C}_{20}$  term is connected to the Earth's flattening term  $J_2 = -\sqrt{5}\bar{C}_{2,0}$  and causes the precession of the orbit with constant  $\dot{\Omega}$ . As in this thesis only circular orbits ( $e = 0$ ) are analysed  $a$  is replaced by the radius  $r$  and  $M$  is equal to the true anomaly  $\nu$  and the eccentric anomaly  $E$ . Furthermore, there is the orbital element of the argument of latitude  $u$  which is the sum of  $\omega$  and  $\nu$ .

A graphical representation of these elements for a circular orbit is shown in Fig. 2.1. The right ascension of the ascending node  $\Omega$  is counted positive from the  $\mathbf{x}$ -axis of the space-fixed frame. The argument of latitude  $u$  and the inclination  $I$  are counted positive from the equatorial plane. The Earth-fixed longitude of the ascending node is  $\Lambda = \Omega - \Theta$  with Greenwich sidereal time  $\Theta$ . From Kepler's third law the mean motion of the satellite is given by

$$n = \sqrt{\frac{GM}{r^3}}. \quad (2.22)$$

Hence, the argument of latitude is

$$u = \omega + M = \omega + n(t - t_0) \quad (2.23)$$

with the epoch of the passage through the perigee  $t_0$ . From these elements the geocentric space-fixed positions  $\mathbf{r}_S$  are determined

$$\mathbf{r}_S = r \begin{pmatrix} \cos u \cos \Omega - \sin u \sin \Omega \cos I \\ \cos u \sin \Omega - \sin u \cos \Omega \cos I \\ \sin u \sin I \end{pmatrix}. \quad (2.24)$$

The transformation from the space-fixed to the Earth-fixed reference frame is approximated by a rotation around the  $z$ -axis with rotation angle  $\Theta$  with  $\dot{\Theta} = \omega_E$ . A more accurate model of this transformation is recommended in the International Earth Rotation and Reference System Service (IERS) conventions (Petit and Luzum, 2010). Here this transformation is described with three transformation matrices according to the motion of the celestial pole, Earth rotation and the Earth's polar motion.

### 2.3.1 Repeat Cycles

Global gravity field determination requires global coverage of satellite groundtracks. This is assured when having a repeat cycle. An orbit with a repeat cycle reaches the same Earth-fixed position after a certain integer repeat period of  $N_{\text{day}}$  nodal days. This means that it performs an integer number of revolutions  $N_{\text{rev}}$  in one repeat period. It is a real repeat orbit when  $N_{\text{day}}$  and  $N_{\text{rev}}$  have no common divisors and it is also denoted as  $N_{\text{day}}/N_{\text{rev}}$  repeat cycle. One nodal day is the time interval after which the same meridian of the Earth crosses the ascending node of the orbit. Because of the precession of  $\Omega$  due to Earth's flattening nodal days differ from solar days except for sun-synchronous orbits. For LEOs on polar orbits the nodal day is shorter than the solar day by 4 minutes (shorter by 15 minutes for  $I = 70^\circ$  and shorter by 20 minutes for  $I = 60^\circ$ ).

The radius  $r$  of an orbit with repeat cycle (repeat orbit) with a given number of revolutions  $N_{\text{rev}}$  in  $N_{\text{day}}$  days can be determined iteratively (Vallado, 2013). The initial value for the mean motion  $n_0$  is

$$n_0 = \frac{N_{\text{rev}}}{N_{\text{day}}} \omega_E \quad (2.25)$$

The initial value for  $r$  is

$$r_0 = \left( \frac{GM}{n_0^2} \right)^{1/3}. \quad (2.26)$$

In the iteration steps for  $r_i$  the rates for the orbital parameters  $\dot{\Omega}$ ,  $\dot{\omega}$  and  $\dot{M}$  are computed from Eq. (2.32) for  $n_i$  and  $r_i$  ( $i = \{0, 1, \dots, i_{\text{max}}\}$ ). And  $r_i$  is derived from Eq. (2.26) with the new value for the mean motion

$$n_i = \frac{N_{\text{rev}}}{N_{\text{day}}} (\omega_E - \dot{\Omega}) - (\dot{M} + \dot{\omega}). \quad (2.27)$$

In the case of a sun-synchronous orbit the rates for the orbital parameters are computed for the inclination  $I_{\text{sun-sync.}i}$  with

$$I_{\text{sun-sync.}i} = \arccos \left( -\frac{2\dot{\Omega}_{\text{sun-sync.}}}{3R^2 J_2} \sqrt{\frac{r_i^7}{GM}} \right). \quad (2.28)$$

Thereby  $\dot{\Omega}_{\text{sun-sync.}}$  is the required node rate for a sun-synchronous orbit with a value of  $2\pi/365.2422$  days =  $1.991064 \cdot 10^{-7}$  rad/s.

*Table 2.1: Altitude difference in km of orbits with the same repeat cycle for selected inclinations and sun-synchronous orbits with respect to polar altitudes (positive values belong to higher altitudes than the polar orbits).*

Polar altitude in km	Inclination in deg.			
	60	70	89	sun-synchronous
500	-42.9	-30.6	-1.69	13.0
400	-44.6	-31.8	-1.76	12.8
300	-46.5	-33.1	-1.82	12.6

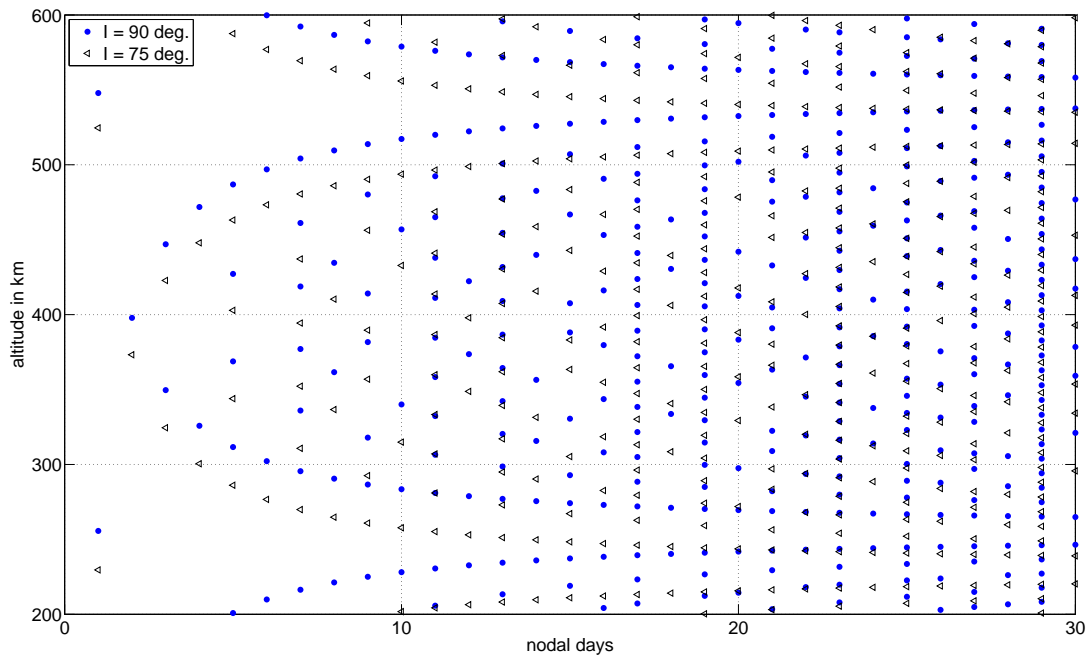


Figure 2.2: Repeat cycles of LEOs for  $I \in \{90^\circ, 75^\circ\}$ .

Repeat orbits with the same repeat cycle ( $N_{\text{rev}}$  revolutions in  $N_{\text{day}}$  days) are found in different altitudes depending on the inclination (Tab. 2.1). Figure 2.2 shows repeat cycles for LEOs with nodal days between  $N_{\text{day}} = 1$  and  $N_{\text{day}} = 30$  for two different inclinations. For the polar orbits it can be seen that in this altitude range there are two 1 day repeat cycles with 15 revolutions at 548 km altitude and with 16 revolutions at 256 km altitude. At 398 km altitude there is the 2 day repeat cycle with 31 revolutions. The cycles with larger repeat period result in a characteristic pattern which is also related to the resonance analyses in Chap. 7.

### 2.3.2 Spatio-Temporal Sampling

The spatio-temporal sampling of a repeat orbit defines the temporal evolution of the global coverage of the orbit. One important parameter in order to get an idea of the spatio-temporal sampling is the Earth-fixed longitude of the ascending equator crossings during one repeat cycle. For LEOs with circular repeat orbits the evolution of these longitudes are monotonously decreasing ( $\dot{\Omega} = 0$ ) by

$$\Delta\lambda = -\frac{2\pi N_{\text{day}}}{N_{\text{rev}}}. \quad (2.29)$$

With the initial longitude  $\lambda_0$  the longitude at the equator after revolution  $i$  is  $\lambda_0 + i\Delta\lambda$  and at the end of the repeat cycle the orbit closes at the same longitude

$$\text{mod}(\lambda_0 + N_{\text{rev}}\Delta\lambda, 2\pi) = \text{mod}(\lambda_0 - 2\pi N_{\text{day}}, 2\pi) = \lambda_0.$$

With the analysis of the gap evolution based on the equator crossing longitudes the repeat orbits can be divided into fast- and slow-skipping orbits (Iran Pour, 2013). For fast-skipping orbits the largest gaps between the equator crossings drop to small values already after a few days. Therefore fast-skipping orbits are favored for the NGGM with the aim of detecting the temporal gravity variations on a global scale. The period of  $N_{\text{sub}} < N_{\text{day}}$  nodal days after which the largest gap drop to a smaller value is the period of a sub-cycle. The periods of all sub-cycles of a repeat cycle can be derived from the two integers  $N_{\text{day}}$  and  $N_{\text{rev}}$ .

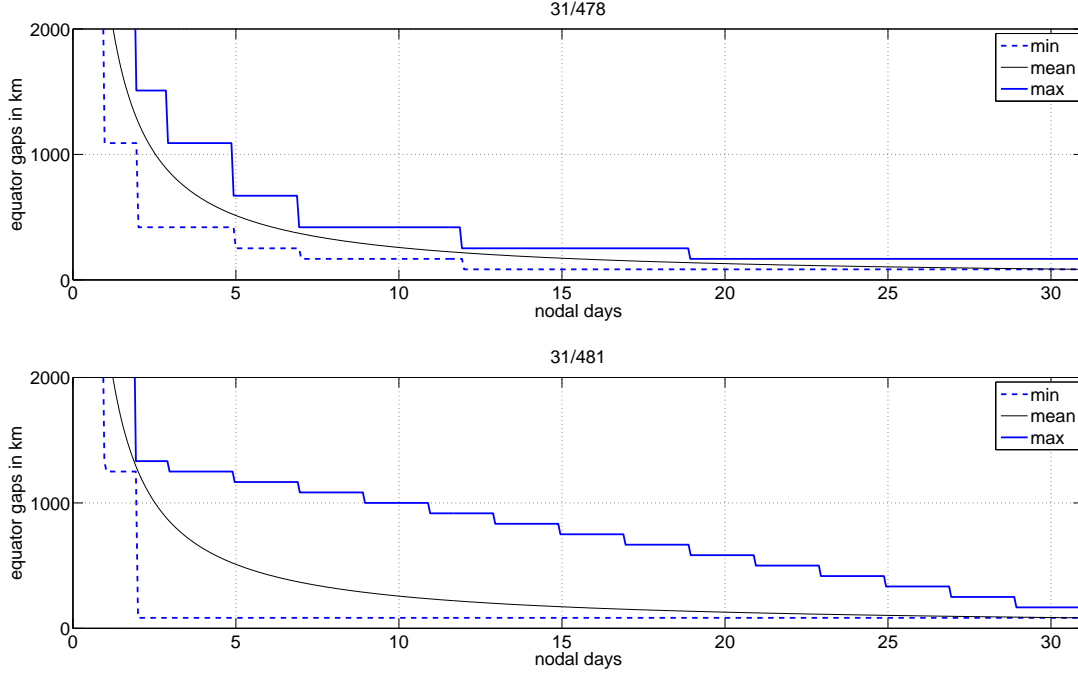


Figure 2.3: Evolution of the equator gap statistics for two 31 day repeat cycles (Top: 478 revolutions. Bottom: 481 revolutions).

The period of the first sub-cycle  $p_1$  is the only integer with

$$p_1 N_{\text{rev}} = N_{\text{day}} n - 1 \quad (2.30)$$

for  $n \in \{1, 2, \dots, N_{\text{rev}}\}$ . The repeat period  $N_{\text{day}}$  is considered as the 0th sub-cycle period  $p_0$ . Then the next sub-cycle periods  $p_j$  for  $j \in \{2, \dots, J\}$  can be found iteratively by

$$p_j = |p_{j-2} - p_{j-1}|. \quad (2.31)$$

The following hypothesis is formulated without a complete mathematical proof. For all real repeat orbits (no common divisors of  $N_{\text{day}}$  and  $N_{\text{rev}}$ ), there is exactly one integer  $p_1$  in Eq. (2.30) for  $N_{\text{day}} > 1$  and the iteration in Eq. (2.31) leads to a  $J < \infty$  (with  $p_j \in \{0, 1\}$  for all  $j \geq J$ ).

Figure 2.3 shows the evolution of the equator gap statistic for two 31 day cycles. According to Iran Pour (2013) the orbit in the top is a fast- and the one in the bottom is a slow-skipping orbit. The drops of the minimum gap lines clearly indicate the different sub-cycles. Equation (2.30) leads to  $p_1 = 19$  for the 31/478 cycle ( $19 \cdot 478 = 31 \cdot 293 - 1$ ) and  $p_1 = 29$  for the 31/481 cycle ( $29 \cdot 481 = 31 \cdot 450 - 1$ ). Thereby the two sub-cycles are reached after 293 and 450 revolutions respectively. Then the iteration of Eq. (2.31) leads to the series of sub-cycles in Tab. 2.2. For the 31/478 cycle it is  $J = 8$  and for 31/481 it

Table 2.2: Sub-cycles of the 31/478 and the 31/481 repeat cycle in nodal days according to Eq. (2.31).

$j$	1	2	3	4	5	6	7	8	9	10	11	12	13	14	15	
31/478	19	12	7	5	2	3	1	2	1	1	0	1	1	0	1	...
31/481	29	2	27	25	2	23	21	2	19	17	2	15	13	2	11	
$j$	16	17	18	19	20	21	22	23	24	25	26	27	28	29	30	
31/481	9	2	7	5	2	3	1	2	1	1	0	1	1	0	1	...

is  $J = 23$ . There are 8 unique numbers  $p_j$  ( $0 \leq j \leq J$ ) for 31/478 and 17 for 31/481, which correspond to the drops of the minimum gap lines in Fig. 2.3. Both the total number  $J$  and the number of unique sub-cycles in relation to  $N_{\text{day}}$  seem to be an indication for the repeat cycle being a fast- (small  $J/N_{\text{day}}$ ) or a slow-skipping (large  $J/N_{\text{day}}$ ) orbit. For LEOs the relation  $J/N_{\text{day}}$  has values between 0 and 1.5 and for the relation with unique sub-cycles it is between 0 and 1. From such an analysis one could divide the repeat cycles into groups according to this unique sub-cycle relation which approaches with increasing  $N_{\text{day}}$  the values  $1/k$  ( $1.5/k$  for  $J/N_{\text{day}}$ ) with positive integer  $k$ .

In this field there seem to be a lot more interesting questions related to number theory. In this thesis the most important conclusion from these repeat cycle and sub-cycle analyses is the following. In the search space of LEOs for the NGGM there are many fast-skipping orbits which are sufficient to provide homogeneously distributed global observations even after a few days. A more detailed selection of optimal orbits will be discussed in Chap. 7.

## 2.4 Simulation Environment

### 2.4.1 Semi-analytical Approach

The semi-analytical approach (Sneeuw, 2000) is used to estimate the VCM of unknown gravity field SH coefficients in a least squares sense according to gravitational observations along a satellite orbit. Assuming a circular repeat orbit with constant inclination the Earth's gravitational potential can be expressed by a SH expansion in a local orbit reference frame. With these simplifications the rates of the Keplerian elements due to the Earth's oblateness can be computed with (Kaula, 1966)

$$\begin{aligned}
 \dot{\Omega} &= -\frac{3}{2}nJ_2 \left(\frac{R}{r}\right)^2 \cos I \\
 \dot{\omega} &= \frac{3}{4}nJ_2 \left(\frac{R}{r}\right)^2 (5 \cos^2 I - 1) \\
 \dot{M} &= n + \frac{3}{4}nJ_2 \left(\frac{R}{r}\right)^2 (3 \cos^2 I - 1) \\
 \dot{u} &= \dot{\omega} + \dot{M} = n + \frac{3}{2}nJ_2 \left(\frac{R}{r}\right)^2 (4 \cos^2 I - 1) \\
 \dot{\Lambda} &= \dot{\Omega} - \omega_E = -\frac{3}{2}nJ_2 \left(\frac{R}{r}\right)^2 \cos I - \omega_E
 \end{aligned} \tag{2.32}$$

The right-handed local orbit reference frame is defined with its equator in the orbital plane ( $x$ -axis radial outwards,  $y$ -axis in along-track and  $z$ -axis in cross-track direction). Rotating the SH expansion of the Earth's gravitational potential  $V$  from the Earth-fixed to this local frame (coordinates  $r$ ,  $u$  and  $\Lambda$ ) a third sum over the index  $k$  is introduced, it reads (Sneeuw, 2000)

$$V(r, u, \Lambda) = \sum_{m=-\infty}^{\infty} \sum_{k=-\infty}^{\infty} A_{mk} e^{i(ku+m\Lambda)} = \sum_{m=-\infty}^{\infty} \sum_{k=-\infty}^{\infty} \sum_{l=\max(|m|, |k|)}^{\infty} H_{lmk} \bar{K}_{lm} e^{i(ku+m\Lambda)}. \tag{2.33}$$

Equation (2.33) represents a 2D Fourier expression of  $V$  with the Fourier coefficients  $A_{mk}$ . The  $A_{mk}$  consist of a sum over SH degree  $l$  and are also called *lumped* coefficients. For each  $l$  it is a product of transfer coefficients  $H_{lmk}$  and the SH coefficients of the Earth's gravitational potential  $\bar{K}_{lm}$ . For the gravitational potential  $V$  the transfer coefficients are

$$H_{lmk} = \frac{GM}{R} \left(\frac{R}{r}\right)^{l+1} \bar{F}_{lmk}(I) \tag{2.34}$$

with the inclination functions  $\bar{F}_{lmk}$ . If  $I$  and  $r$  are constant, Eq. (2.32) may be applied and the coordinates  $u$  and  $\Lambda$  can be written as  $\dot{u}t$  and  $\dot{\Lambda}t$ , respectively (Sneeuw, 2000). Hence, the Fourier coefficients  $A_{mk}$  become constant as well, because the exponent depends linearly on  $t$ .

In the same way the corresponding transfer coefficients of other functionals of  $V$  can be set up. The transfer coefficients for SGG are computed from the second derivatives of  $V$  with respect to radial, along-track and cross-track direction. Hence, the  $V_{rr}$  transfer coefficients read (Sneeuw, 2000)

$$H_{lmk}^{V_{rr}} = \frac{GM}{R^3} \left(\frac{R}{r}\right)^{l+3} (l+1)(l+2) \bar{F}_{lmk}(I). \quad (2.35)$$

High-low SST is assessed in terms of 3D orbit perturbations in the preferred coordinate frame with  $x$ -axis in along-track,  $y$ -axis in cross-track, and  $z$ -axis in radial direction. This frame is obtained by a permutation of the axes of the local orbit frame to which  $V$  is rotated (Eq. (2.33)). The transfer for the orbit perturbations  $(\Delta x, \Delta y, \Delta z)$  is derived based on linearized Hill equations with harmonic force term. With the normalized frequencies (Sneeuw, 2000)

$$\beta_{mk} = \frac{k\dot{u} + m\dot{\Lambda}}{n} = k + m\frac{\dot{\Lambda}}{\dot{u}} \quad (2.36)$$

the transfer coefficients for high-low SST are (Sneeuw, 2000)

$$\begin{aligned} H_{lmk}^{\Delta x} &= R \left(\frac{R}{r}\right)^{l-1} i \frac{2(l+1)\beta_{mk} - k(\beta_{mk}^2 + 3)}{\beta_{mk}^2(\beta_{mk}^2 - 1)} \bar{F}_{lmk}(I) \\ H_{lmk}^{\Delta y} &= R \left(\frac{R}{r}\right)^{l-1} \frac{1}{1 - \beta_{mk}^2} \bar{F}_{lmk}^*(I) \\ H_{lmk}^{\Delta z} &= R \left(\frac{R}{r}\right)^{l-1} \frac{(l+1)\beta_{mk} - 2k}{\beta_{mk}(\beta_{mk}^2 - 1)} \bar{F}_{lmk}(I). \end{aligned} \quad (2.37)$$

For the cross-track high-low SST component  $\Delta y$  the cross-track inclination function  $\bar{F}_{lmk}^*(I)$  is used which is the cross-track derivative of  $\bar{F}_{lmk}(I)$ .

The transfer coefficients for low-low SST in terms of inter-satellite ranges  $\Delta\rho$  are a combination of the along-track and radial orbit perturbation transfer coefficients (in-line pair) making use of the inter-satellite distance  $\rho = 2r \sin \eta$  with half opening angle  $\eta$ . It is (Sneeuw, 2000)

$$H_{lmk}^{\Delta\rho} = 2i \cos \eta \sin(\eta\beta_{mk}) H_{lmk}^{\Delta x} + 2 \sin \eta \cos(\eta\beta_{mk}) H_{lmk}^{\Delta z}. \quad (2.38)$$

In contrast to a low-low SST in-line formation in a so-called Pendulum formation the trailing satellite performs periodic movements in cross-track direction wrt. the leading satellite. Hence, for a Pendulum pair the cross-track orbit perturbation transfer coefficients contribute to the low-low SST transfer as well. Furthermore, the time derivatives of the ranges, i.e. range rates and range accelerations are implemented applying a factor  $i n \beta_{mk}$  and  $-n^2 \beta_{mk}^2$  to  $H_{lmk}^{\Delta\rho}$ , respectively.

The semi-analytical approach (SANA) in this thesis is used to estimate the VCM of SH coefficients  $\mathbf{Q}_{\hat{x}\hat{x}}$  from the inversion of normal equation matrices (cf. Eq. 2.13) up to maximum SH degree  $l_{\max}$ . The above described transfer coefficients are computed in the spectral domain and fill the design matrix of the least squares system. The corresponding stochastic model is computed from the amplitude spectral density (ASD) of the observation noise. The ASD of a stationary time series  $x(t)$  is the square-root of the power spectral density (PSD). The PSD is the Fourier Transform of the autocorrelation function of  $x$ . For ARMA filters the PSD is given by the absolute square of the frequency response (2.19), i.e.  $|H(e^{i\omega})|^2$ . In this thesis all ASDs of time series are derived from PSDs computed with Welch's method (Welch, 1967).

The inversion of the normal equation matrix is done independently for each SH order  $m$ , which makes the SANA computationally fast. In real gravity field determination with GOCE this approach was

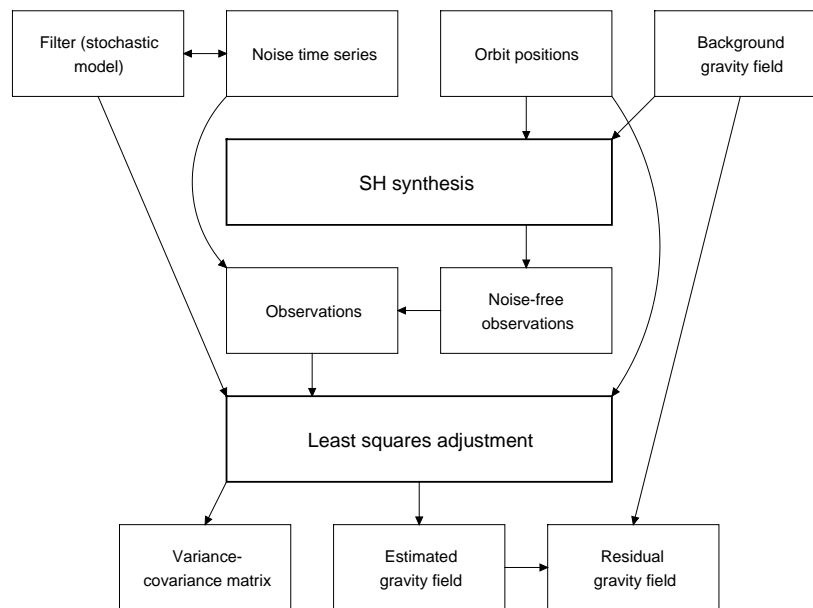


Figure 2.4: Scheme of the linear closed-loop simulation (cf. Murböck et al. (2014)). The four boxes in the top represent the main input and the three boxes in the bottom represent the main output. The main processing steps are the SH synthesis and the least squares adjustment.

successfully implemented with iterative processing (Pail et al., 2007). In this thesis, the SANA is used to estimate the formal errors of SH coefficients, not the coefficients themselves. Therefore no observations are needed and hence no deterministic observation contents, e.g. temporal aliasing, can be assessed. More details and several simulation examples can be found in Sneeuw (2000) and Murböck (2011).

## 2.4.2 Linear Closed-loop Approach

The second simulation environment used in this thesis is a numerical linear closed-loop approach (LCLA). The observations are computed from static and time varying background gravity field models for each epoch up to  $l_{\max}$ . In a LSA the unknown gravity field parameters together with their variance-covariance information are estimated from the inversion of a full normal equation matrix. The functional model for the gravitational potential  $V$  is given by Eq. (2.3) with the gravity field parameters  $\hat{C}_{lm}$  and  $\hat{S}_{lm}$  to be estimated. For SGG, only the radial component is shown here, which is the second derivative of  $V$  with respect to  $r$

$$\hat{\mathbf{I}}_{V_{rr}}(r, \theta, \lambda) = \frac{GM}{R^3} \sum_{l=0}^{l_{\max}} (l+1)(l+2) \left(\frac{R}{r}\right)^{l+3} \sum_{m=0}^l \bar{P}_{lm}(\cos \theta) \left( \hat{C}_{lm} \cos m\lambda + \hat{S}_{lm} \sin m\lambda \right). \quad (2.39)$$

The functional model for low-low SST is formulated in terms of inter-satellite gravitational acceleration differences along the line of sight (LoS), it reads

$$\hat{\mathbf{I}}_{\text{low-low SST}} = \langle \Delta \mathbf{a}_{\text{grav.}}, \Delta \mathbf{r}_0 \rangle. \quad (2.40)$$

Here the  $\Delta$  means the difference between the two satellites,  $\Delta \mathbf{a}_{\text{grav.}}$  are the gravitational acceleration differences containing the gravitational potential gradient differences, and  $\Delta \mathbf{r}_0$  is the unit vector pointing from one satellite to the other.

In all NGGM low-low SST simulations with the LCLA the error contributions of the two main instruments are taken into account, i.e. the laser ranging instrument (LRI) and the accelerometer (ACC). The

LRI measures the total contribution to the LoS acceleration differences from which the non-gravitational part has to be subtracted with ACC observations, i.e.

$$\langle \Delta \mathbf{a}_{\text{grav.}}, \Delta \mathbf{r}_0 \rangle = \langle \Delta \mathbf{a}_{\text{total}}, \Delta \mathbf{r}_0 \rangle - \langle \Delta \mathbf{a}_{\text{non-grav.}}, \Delta \mathbf{r}_0 \rangle. \quad (2.41)$$

The total LoS acceleration differences contain a range dependent term and a term depending on the velocity differences between the two satellites. It reads

$$\langle \Delta \mathbf{a}_{\text{total}}, \Delta \mathbf{r}_0 \rangle = \ddot{\rho} + \frac{\dot{\rho}^2 - \|\Delta \dot{\mathbf{r}}\|^2}{\rho} \quad (2.42)$$

and the very right part of Eq. (2.42) is called the velocity term. The error contribution of the velocity term is neglected in this thesis, it is assumed that the total error is dominated by the range dependent part  $\ddot{\rho}$  and therefore by the LRI noise. This is a major simplification according to Rummel (1979); Jekeli (1999); Sharifi (2004); Keller and Sharifi (2005); Reubelt et al. (2006). Methods in order to approximate the velocity term with range observations are described in Chen et al. (2008); Liu (2008); Liu et al. (2010). However, the SANA low-low SST functional model is derived from orbit perturbations (Eq. 2.38) and therefore contains the velocity term contribution. In Sec. 2.4.3 comparable low-low SST SANA and LCLA results are shown based on the same noise assumptions for  $\Delta \ddot{\rho}$  (Eq. 2.38) and  $\hat{\mathbf{I}}_{\text{low-low SST}}$  (Eq. 2.40), respectively. Therefore this simplification is assumed to be not critical.

As for SGG, the LoS acceleration differences depend linearly on the unknown gravity field parameters, no iteration, no linearization and no a priori gravity field information are needed. Figure 2.4 shows the scheme of this LCLA. In contrast to the previous discussed SANA simulations, here the observations are used to estimate not only the formal errors but also the gravity field parameters. Here, the stochastic model is applied with ARMA filters according to Eq. 2.21. The inverse frequency response of the filter approximates the ASD of the introduced noise time series.

The comparison of variance-covariance information with the residuals between the estimated and the reference background gravity field carries important information. The stochastic model is represented

*Table 2.3: Static and time varying background gravity field models used in this thesis.*

	Name	Reference	$l_{\text{max}}$
Static gravity	CO_CONS_GCF_2_TIM5	Brockmann et al. (2014)	280
	GGM05S	Tapley et al. (2013)	180
	ULux_CHAMP2013s	Weigelt et al. (2013)	120
	EGM2008	Pavlis et al. (2012)	2190
	ITG-Grace2010s	Mayer-Gürr et al. (2010)	180
	GOCO02S	Pail et al. (2010)	250
	EIGEN-GL04C	Förste et al. (2006)	360
Monthly GRACE solutions	CSR RL05	Tapley et al. (2013)	96
	GFZ RL05	Dahle et al. (2014)	90
	JPL RL05	Watkins and Yuan (2012)	90
	ITSG-Grace2014	Mayer-Gürr (2014)	90
Ocean tides	EOT08a	Savcenko and Bosch (2008)	80
	FES2004	Lyard et al. (2006)	80
Non-tidal temporal gravity	ESA-AOHIS	Gruber et al. (2011)	180
	upd-ESA-AOHIS	Dobslaw et al. (2014)	180

by an ARMA filter (cf. Sec. 2.2). If the true errors of the observations are modeled adequately by this filter, the variance-covariance matrix of the unknowns model also the true errors of the unknowns. This is the case if the observations contain only stochastic noise and the absolute frequency response of the filter coincides with the noise ASD. The situation is different when the background gravity field is time varying. Then the residuals between unknowns (mean gravity field for observation duration) and the mean background gravity field are not only stochastic and contain also deterministic signal from temporal aliasing (cf. Chap. 6 and 7).

The background gravity field consists of up to three parts, i.e. a static gravity field model, an ocean tide model and a non-tidal time varying gravity field model. Table 2.3 shows the background gravity models used in this thesis. From these models the observations for each epoch  $t$  are computed by SH synthesis from SH coefficients

$$\bar{K}_{lm}(t) = \bar{K}_{lm}^{\text{static}} + \bar{K}_{lm}^{\text{ocean tides}}(t) + \bar{K}_{lm}^{\text{non-tidal temporal}}(t). \quad (2.43)$$

For each tidal constituent the SH coefficients for the ocean tides  $\bar{K}_{lm}^{\text{ocean tides}}(t)$  are computed from pro- and retrograde ocean tide coefficients. Thereby the six Doodson variables are used, which denote fundamental arguments of the orbit of the Sun and the Moon (Montenbruck and Gill, 2005). In this thesis the eight major diurnal and semi-diurnal constituents are used from the ocean tide models in Tab. 2.3. The SH coefficients for the non-tidal temporal variations  $\bar{K}_{lm}^{\text{non-tidal temporal}}(t)$  are computed from the models in Tab. 2.3 which are provided with 6 hours sampling. The models represent mass distributions in Atmosphere (A), Ocean (O), continental Hydrology (H), Ice (I) and Solid Earth (S), and they are linearly interpolated to the observation epochs.

### 2.4.3 Simulation Approach Comparison

Sections 2.4.1 and 2.4.2 give the basis for two independent simulation approaches. Here, their results are compared for low-low SST and radial SGG observations. A similar comparison for low-low SST can be found in Murböck and Pail (2014), and comparisons of these two approaches with other independent simulation procedures are given in Gruber et al. (2014).

Three test cases are used for different aspects of this comparison (cf. Tab. 2.4). A spectral representation of the observation noise for all three cases in terms of ASDs is shown in Fig. 2.5. These noise spectra are directly used to form the weighting matrices in the spectral domain for the normal equations of the SANA. For the LCLA an ARMA filter model is adjusted to these spectra according to Eq. (2.21). The absolute error scale of all simulations in this section depends linearly on the scale of the noise ASDs. Case 1 is the comparison for the radial SGG component  $V_{rr}$  for a monthly (29/462) circular polar repeat orbit in 273 km altitude. The ASD of the observation noise  $a_{V_{rr}}$  is shown in comparison with a GOCE-like  $V_{rr}$  accuracy (left). The analytical noise model is

$$a_{V_{rr}}(f) = 10^{-4} \cdot \sqrt{\left(\frac{0.001 \text{ Hz}}{f}\right)^4 + 1 + \left(\frac{f}{0.1 \text{ Hz}}\right)^4} \frac{\text{E}}{\sqrt{\text{Hz}}} \quad (2.44)$$

with 1 Eötvös Unit = 1 E =  $10^{-9}\text{s}^{-2}$ . Hence, the SGG instrument for Case 1 is much more sensitive than a GOCE-like gradiometer. The white noise part at  $0.1 \text{ mE}/\sqrt{\text{Hz}}$  is smaller than the GOCE-like white noise level by a factor of 200 and it is broader (down to 1 mHz instead of 5 mHz for GOCE-like).

Figure 2.6 shows the formal errors (top left) compared with the residuals (top right) wrt. the static reference model EIGEN-GL04C (Förste et al., 2006) in the SH domain up to  $l_{\text{max}} = 60$ . Because of two reasons both approaches give the same formal errors for Case 1. First, a circular repeat orbit with constant inclination satisfies the conditions of the SANA. Second, for  $V_{rr}$  the functional model is the same in both approaches, although it is evaluated in the spectral domain for the SANA and in the spatial domain for the LCLA (bottom left). The weakness of  $V_{rr}$  for large spatial scales is reflected in larger errors for low SH degrees.

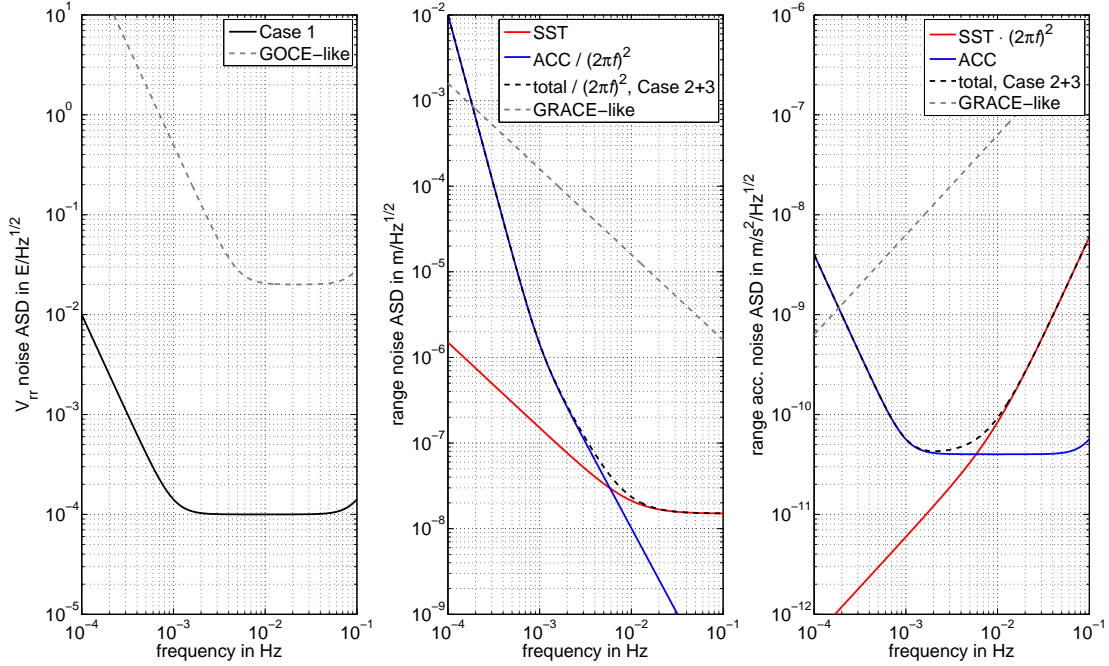


Figure 2.5: Noise ASDs for the three simulation cases (cf. Tab. 2.4) of radial SGG (left) in  $E$  ( $1 E \ddot{\text{o}}tv\ddot{\text{o}}s \text{ Unit} = 1 E = 10^{-9} \text{s}^{-2}$ ) and low-low SST noise contributions in terms of ranges (center) and range accelerations (right).

An analysis with white  $V_{rr}$  noise would lead to an isotropic error spectrum. The colored noise used in Case 1 makes the error spectra in Fig. 2.6 (top) anisotropic especially for the low SH degrees. Here the errors increase with increasing  $m$  resulting in larger errors for sectorial ( $m = l$ ) than for zonal ( $m = 0$ ) coefficients. The good matching of the formal errors with the LCLA residuals indicates a realistic stochastic model, which is in accordance with the actual noise behaviour.

The SH degree RMS curves (bottom left) representing global mean geoid errors emphasize, that the two simulation approaches lead to realistic comparable results for radial SGG. An error propagation of the block-diagonal variance-covariance matrices lead to the cumulative geoid error depending on the latitude  $\phi$  for the SANA (bottom right). For the LCLA the Root-Mean-Square (RMS) rms for each latitude of global ( $1^\circ \times 1^\circ$  grid) geoid height residuals  $\delta_N$  is shown. It reads

$$\text{rms}(\phi) = \sqrt{\frac{1}{n} \sum_{i=1}^n \delta_{N,i}^2} \quad (2.45)$$

Table 2.4: Simulation cases for the inter-comparison of the semi-analytical and the linear closed-loop approach.

	Observation	$l_{\max}$	Scenario	Orbit	Noise ASD
Case 1	$V_{rr}$	60	single polar ( $I = 89^\circ$ )	29/462 repeat orbit (273 km alt.)	Figure 2.5 left
Case 2	low-low SST (range acc.)	100	single polar pair ( $I = 89^\circ$ )	31/478 repeat orbit (420 km alt.)	Figure 2.5 right
Case 3	low-low SST (range acc.)	150	double pair, polar ( $I = 89^\circ$ ) and inclined ( $I = 70^\circ$ )	realistic orbits (32 days), 420 km (polar) and 429 km (inclined) alt.	Figure 2.5 right

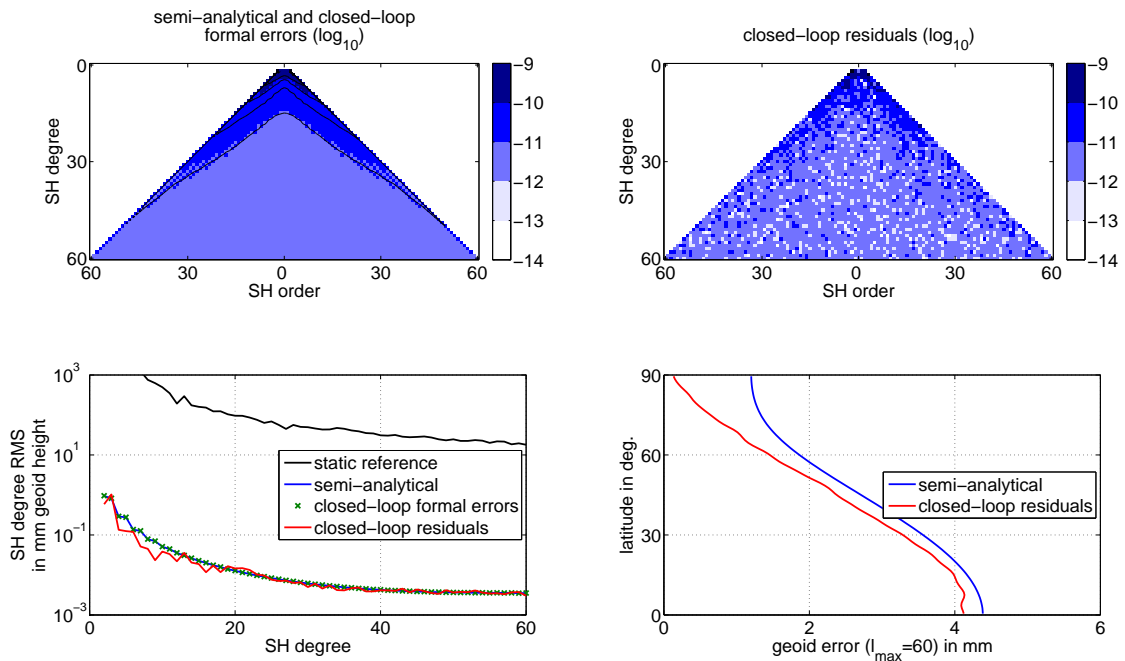


Figure 2.6: Simulation comparison for radial SGG  $V_{rr}$  for a circular repeat orbit. Top:  $\log_{10}$ -scaled formal errors (left) and residuals of the closed-loop simulation with respect to the static reference (right). Bottom left: SH degree RMS in mm geoid height. Bottom right: geoid error ( $l_{\max} = 60$ ) depending on the latitude.

with  $n = 180$  longitudinal grid points. The geoid error decreases with increasing latitude because of increasing spatial observation density (bottom right). For the SANA this cumulative geoid error up to  $l_{\max} = 60$  is larger than for the LCLA by approximately 10% for low to medium latitudes. This is mainly due to lower residuals compared with the formal errors in the low SH degrees (cf. Fig. 2.6, bottom left).

The Case 2 scenario (cf. Tab. 2.4) is a single polar low-low SST pair with a monthly repeat cycle (31/478, cf. Fig. 2.3) in a mean altitude of 420 km. Both Case 2 and 3 contain a GRACE-like in-line formation which means that the two satellites are on the same orbit with a constant shift in the mean anomaly. Therefore the LoS has mainly along-track components and the error spectrum is anisotropic. The inter-satellite distance is 100 km and the ranging instrument is assumed to be a laser interferometer similar to the one on GRACE-FO with an ASD of (Gruber et al., 2014)

$$a_{\text{SST}}(f) = 1.5 \cdot 10^{-8} \cdot \sqrt{\left(\frac{0.01 \text{ Hz}}{f}\right)^2 + 1} \frac{\text{m}}{\sqrt{\text{Hz}}}. \quad (2.46)$$

The noise ASD for low-low SST in terms of range rates and range accelerations then is given by the multiplication of  $a_{\text{SST}}(f)$  with  $2\pi f$  and  $(2\pi f)^2$ , respectively. The accelerometers (ACC) measuring the non-gravitational forces acting on both satellites are the second dominating error source. The ACC noise ASD assumption is also taken from (Gruber et al., 2014) with

$$a_{\text{ACC}}(f) = 4 \cdot 10^{-11} \cdot \sqrt{\left(\frac{0.001 \text{ Hz}}{f}\right)^4 + 1 + \left(\frac{f}{0.1 \text{ Hz}}\right)^4} \frac{\text{m}}{\text{s}^2 \sqrt{\text{Hz}}}. \quad (2.47)$$

Then the total low-low SST noise ASD in terms of range accelerations is given by

$$a_{\text{total}}(f) = \sqrt{\left(a_{\text{SST}}(f) \cdot (2\pi f)^2\right)^2 + a_{\text{ACC}}^2(f)} \frac{\text{m}}{\text{s}^2 \sqrt{\text{Hz}}}. \quad (2.48)$$

At this point other noise contributions in a low-low SST satellite mission as for example the attitude errors are neglected (cf. Chap. 5). Figure 2.5 shows the total noise ASD for Case 2 and 3 with its two

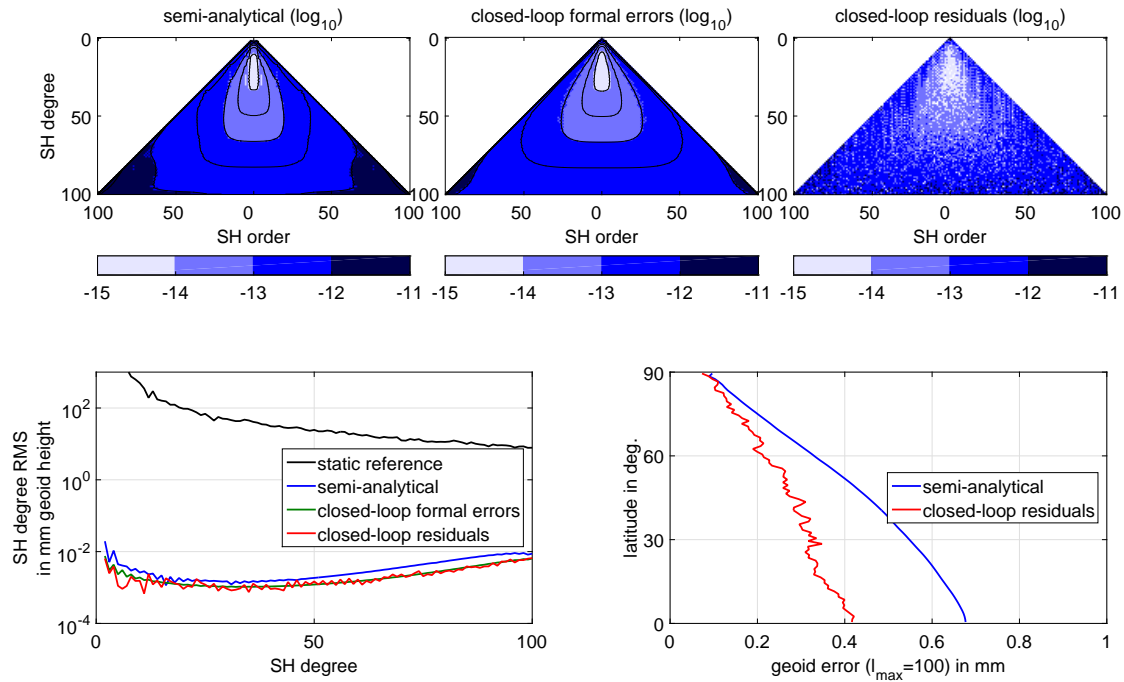


Figure 2.7: Simulation comparison for low-low SST for a circular repeat orbit. Top:  $\log_{10}$ -scaled formal errors of the semi-analytical (left) the linear closed-loop approach (center) and  $\log_{10}$ -scaled residuals of the closed-loop simulation with respect to the static reference (right). Bottom left: SH degree RMS in mm geoid height. Bottom right: geoid error ( $l_{\max} = 100$ ) depending on the latitude.

components in comparison with a GRACE-like range rate accuracy of  $1 \mu\text{m/s}$ , transformed to ranges and range accelerations respectively (center and right). The ACC noise dominates below  $f = 6 \text{ mHz}$  and the SST noise above. The GRACE-like noise ASD is higher than the total noise ASD by up to 3 orders of magnitude.

As in Case 1 the orbits are repeat orbits, but now different functional models for the range acceleration observations are used in the two simulators (cf. Sec. 2.4.1 and 2.4.2). Nevertheless, the two approaches lead to comparable results in terms of formal errors ( $l_{\max} = 100$ ) with typical GRACE-like error characteristics with high sensitivity (low formal errors) for the zonal and low sensitivity for the sectorial coefficients (cf. Fig. 2.7, top). The formal errors of the SANA (left) are larger than the ones of the LCLA (center) by up to a factor of 2 around the sectorials, around the zonals they match. Due to larger errors around the sectorials the SH degree RMS of the SANA formal errors are larger than the formal errors and residuals of the LCLA by a factor between 1.2 and 1.8. The geoid errors per latitude (bottom right) show the largest differences at the equator with a factor of 1.8. These deviations give an estimate of how realistic the results of the two simulators are for low-low SST.

In this thesis only simplified circular orbits are used for the simulations (cf. Sec. 2.3). Simulation comparison Case 3 shows that the results are realistic up to  $l_{\max} = 150$  despite this simplification. Furthermore it proves that the differences between the two approaches for a double low-low SST pair are smaller than for a single polar in-line pair. This double low-low SST pair is in a Bender-type constellation (Bender et al., 2008) with one polar and one inclined pair. The inclined pair of Case 3 has an inclination of 70 degrees. The realistically integrated 32 days orbits for the LCLA are also used in the final full-scale simulations in Gruber et al. (2014). For the SANA 32 day repeat orbits are chosen with the same altitudes as the realistic orbits (cf. Tab. 2.4).

The noise ASD for both pairs of Case 3 is the same as in Case 2. Figure 2.8 shows the spectral error characteristics for the single polar (top row) and inclined pair (center row) and for the combined solution (bottom row). As the residuals (right column) fit the formal errors the stochastic model is correct. As in Case 2 the formal errors of both approaches (left and center) show small differences around the

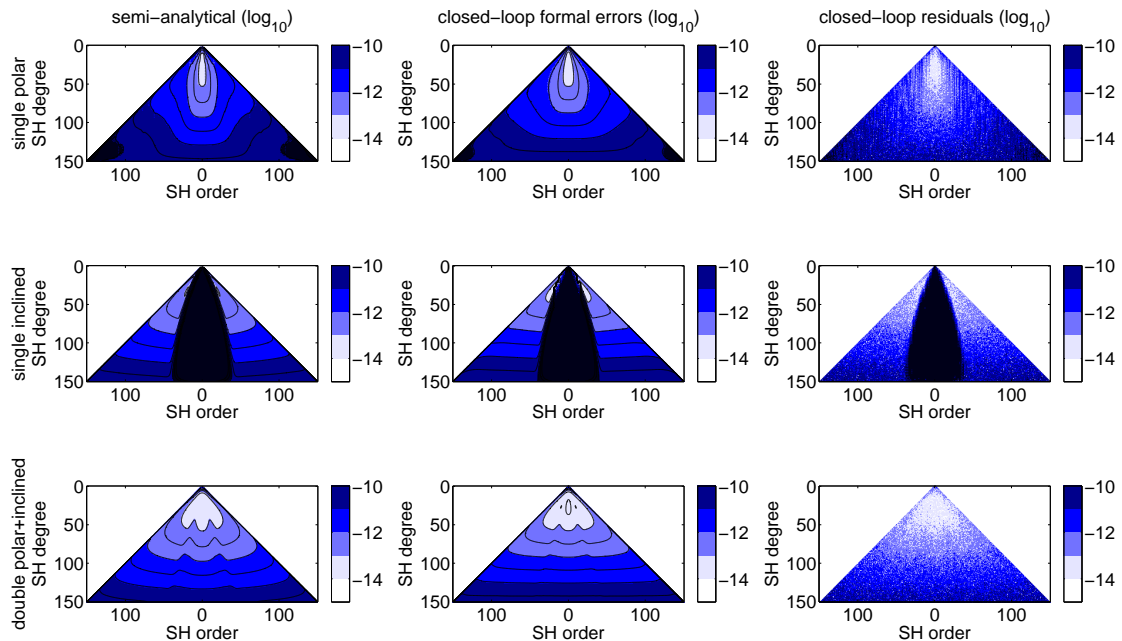


Figure 2.8: Simulation comparison for double low-low SST mission on realistic orbits in terms of  $\log_{10}$ -scaled formal errors of the semi-analytical (left column) and the linear closed-loop approach (center column) and  $\log_{10}$ -scaled residuals of the closed-loop simulation with respect to the static reference (right column). The top row shows the error spectra of the single polar, the center row for the single inclined and the bottom row for the combined double pair.

sectorials. For the inclined pair the deviations are smaller. The effects of the polar gap for the inclined pair can be seen in large errors around the zonals. The combined solution shows the advantage of this Bender-type scenario. The sectorial coefficients benefit from high sensitivity of the inclined pair, and the zonals benefit from the polar pair. This makes the error spectrum more isotropic compared to a single in-line pair.

The geoid errors in terms of SH degree RMS and the cumulative ( $l_{\max} = 150$ ) geoid errors depending on the latitude are shown in Fig. 2.9. Again the formal errors for the SANA are compared with the RMS of the LCLA residuals. For the polar pair the relative error characteristics of the two approaches are the same as in Case 2. The SH degree RMS curves for the double pair solutions approach each other with increasing SH degree. This results in a good agreement of the cumulative geoid errors per latitude (max. deviations at low latitudes up to 15%). The single inclined solution of the LCLA results in very large errors for the polar gap but for low latitudes the geoid errors are smaller than for the single polar solution.

With these three simulation cases it is shown that both approaches lead to comparable results for both radial SGG and low-low SST. The largest deviations are observed for single in-line polar solutions. In this thesis, the computationally fast SANA is used to estimate the sensitivity of different scenarios up to high SH degrees and orders. In chap. 4 the instrument requirements are derived from SANA simulations in comparison with the mission objectives. With the LCLA effects of non-stochastic processes, e.g. temporal aliasing from tidal and non-tidal mass variations, are assessed (Chap. 7). The different error sources addressed in this thesis are stochastic instrument noise as in the above examples and non-stochastic temporal aliasing errors.

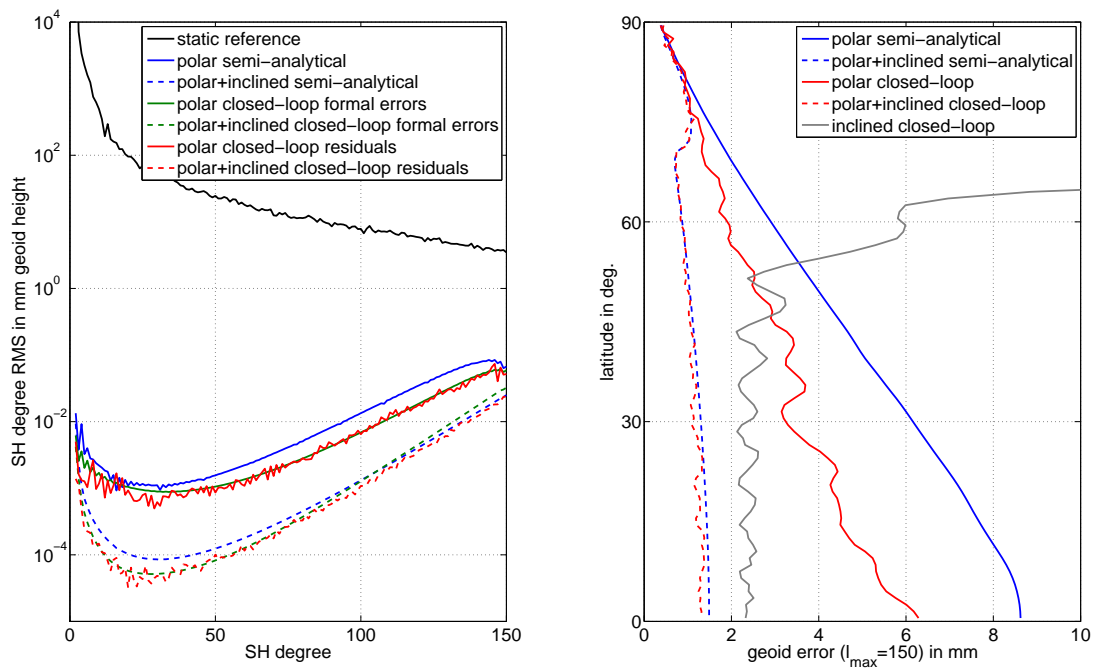


Figure 2.9: Simulation comparison for double low-low SST mission on realistic orbits in terms of SH degree RMS in mm geoid height (left) and geoid error ( $l_{\max} = 150$ ) depending on the latitude.

## 3 From Science Requirements to Mission Objectives

In this chapter the mission objectives (MO) of the NGGM are derived from the science requirements (SR). The starting point are consolidated SR for different sub-systems of the Earth. The SR are defined in terms of required accuracies for specific spatial and temporal resolutions for different signals of interest. After the conversion to geoid heights (depending on the spatial resolution, Sec. 3.1) they are converted to requirements for the basic temporal resolution of 1 month. For this the SR for static and trend signals are translated based on formal error propagation (sec. 3.2). The SR are shown in Tab. 3.2. The MO are defined in Sec. 3.3 taking into account current mission accuracies and signal attenuation due to the orbital altitude.

### 3.1 Translation to Geoid Heights

The SR formulated in required accuracies for required temporal and spatial resolutions for specific (geophysical) signals of interest can be found in Sneeuw et al. (2005), Panet et al. (2013), and Gruber et al. (2014). Four different physical units are used in these studies for the different signals in the fields of hydrology, cryosphere, ocean, solid Earth, and geodesy. These units are geoid heights  $N$  in m, gravity anomalies  $\Delta g$  in Gal ( $1 \text{ Gal} = 10^{-2} \text{ m/s}^2$ ), radial gravity gradients  $V_{rr}$  in E ( $1 \text{ E} = 10^{-9} \text{ s}^{-2}$ ) and surface densities  $S$  in  $\text{kg/m}^2$ . In this thesis surface densities are regarded as equivalent water heights (EWH) in m, i.e. 1 mm of EWH corresponds to a surface density of  $1 \text{ kg/m}^2$ . In spherical approximation the SH expansions of  $N$ ,  $\Delta g$ ,  $V_{rr}$  and  $S$  are given in Eq. (3.1) using the short notation for the SH coefficients and base functions in Eq. (2.5).

$$\begin{aligned}
 N(\theta, \lambda) &= R \sum_{l=0}^{l_{\max}} \sum_{m=0}^l \bar{K}_{lm} \bar{Y}_{lm}(\theta, \lambda) \\
 \Delta g(\theta, \lambda) &= \frac{GM}{R^2} \sum_{l=0}^{l_{\max}} (l-1) \sum_{m=0}^l \bar{K}_{lm} \bar{Y}_{lm}(\theta, \lambda) \\
 V_{rr}(\theta, \lambda) &= \frac{GM}{R^3} \sum_{l=0}^{l_{\max}} (l+1)(l+2) \sum_{m=0}^l \bar{K}_{lm} \bar{Y}_{lm}(\theta, \lambda) \\
 S(\theta, \lambda) &= \frac{M}{4\pi R^2} \sum_{l=0}^{l_{\max}} \frac{2l+1}{1+k'} \sum_{m=0}^l \bar{K}_{lm} \bar{Y}_{lm}(\theta, \lambda)
 \end{aligned} \tag{3.1}$$

In order to compare different signals of different units with each other, a conversion can be derived from Eq. (3.1) from the relation between the cumulative degree variances up to a specific SH degree  $l_{\max}$ . This max. degree corresponds to a spatial resolution on the Earth's surface of  $\pi R/l_{\max} \approx 20,000 \text{ km}/l_{\max}$ . Figure 3.1 and Tab. 3.1 give the graphical and numerical representations of this conversion, respectively. This analytical approach gives comparable values as numerical simulations based on Gaussian bell shaped signals in Panet et al. (2013).

Table 3.1: Conversion between geoid heights in mm, gravity anomalies in  $\mu\text{Gal}$ , gravity gradients in mE and EWH in cm depending on the spatial resolution in km.

spatial res. in km	SH degree	1 mm geoid height			1 $\mu\text{Gal}$ gravity anomaly			1 mE gravity gradient			1 cm EWH		
		gravity anomaly in $\mu\text{Gal}$	gravity gradient in mE	EWH in cm	geoid height in mm	gravity gradient in mE	EWH in cm	geoid height in mm	gravity anomaly in $\mu\text{Gal}$	EWH in cm	geoid height in mm	gravity anomaly in $\mu\text{Gal}$	gravity gradient in mE
10	2,004	218	560	520	0.00460	2.57	2.39	0.00179	0.389	0.930	0.00192	0.418	1.08
20	1,002	109	140	260	0.00920	1.29	2.40	0.00713	0.776	1.86	0.00384	0.417	0.538
30	668	72.4	62.4	174	0.0138	0.862	2.40	0.0160	1.16	2.79	0.00574	0.416	0.359
40	501	54.3	35.2	131	0.0184	0.648	2.41	0.0284	1.54	3.71	0.00765	0.415	0.269
50	401	43.4	22.6	105	0.0230	0.520	2.41	0.0443	1.92	4.64	0.00955	0.415	0.216
60	334	36.2	15.7	87.4	0.0276	0.434	2.42	0.0636	2.30	5.56	0.0114	0.414	0.180
70	286	31.0	11.6	75.0	0.0323	0.373	2.42	0.0864	2.68	6.48	0.0133	0.413	0.154
80	250	27.1	8.88	65.7	0.0369	0.328	2.43	0.113	3.05	7.40	0.0152	0.412	0.135
90	223	24.1	7.03	58.5	0.0415	0.292	2.43	0.142	3.42	8.32	0.0171	0.412	0.120
100	200	21.7	5.71	52.7	0.0462	0.263	2.43	0.175	3.80	9.24	0.0190	0.411	0.108
200	100	10.8	1.46	26.7	0.0928	0.135	2.48	0.686	7.39	18.3	0.0374	0.403	0.0546
300	67	7.15	0.662	18.1	0.140	0.0926	2.53	1.51	10.8	27.3	0.0554	0.396	0.0367
400	50	5.34	0.380	13.7	0.187	0.0713	2.57	2.63	14.0	36.0	0.0729	0.389	0.0278
500	40	4.25	0.249	11.1	0.235	0.0585	2.61	4.02	17.1	44.6	0.0902	0.383	0.0224
600	33	3.53	0.176	9.34	0.284	0.0500	2.65	5.67	20.0	52.9	0.107	0.378	0.0189
700	29	3.01	0.132	8.08	0.332	0.0440	2.69	7.56	22.7	61.0	0.124	0.372	0.0164
800	25	2.62	0.103	7.13	0.382	0.0395	2.72	9.67	25.3	68.9	0.140	0.367	0.0145
900	22	2.32	0.0835	6.39	0.431	0.0360	2.76	12.0	27.8	76.6	0.156	0.363	0.0131
1,000	20	2.08	0.0690	5.80	0.481	0.0332	2.79	14.5	30.1	84.1	0.172	0.358	0.0119
2,000	10	0.997	0.0210	3.15	1.00	0.0211	3.16	47.6	47.5	150	0.318	0.317	0.00667
3,000	7	0.643	0.0113	2.30	1.56	0.0176	3.58	89.2	56.9	204	0.436	0.279	0.00491
4,000	5	0.464	0.00752	1.89	2.16	0.0162	4.09	133	61.6	252	0.528	0.245	0.00397
5,000	4	0.359	0.00568	1.68	2.79	0.0158	4.68	176	63.2	295	0.596	0.214	0.00339
6,000		0.297	0.00475	1.56	3.47	0.0160	5.37	216	62.3	334	0.642	0.189	0.00302
7,000	3	0.245	0.00401	1.47	4.17	0.0164	6.10	252	60.9	370	0.681	0.166	0.00272
8,000		0.215	0.00364	1.42	4.95	0.0172	6.93	283	58.4	399	0.706	0.150	0.00254
9,000		0.185	0.00327	1.37	5.72	0.0180	7.76	314	55.8	428	0.731	0.133	0.00237
10,000	2	0.154	0.00290	1.32	6.49	0.0188	8.60	345	53.2	457	0.755	0.116	0.00219

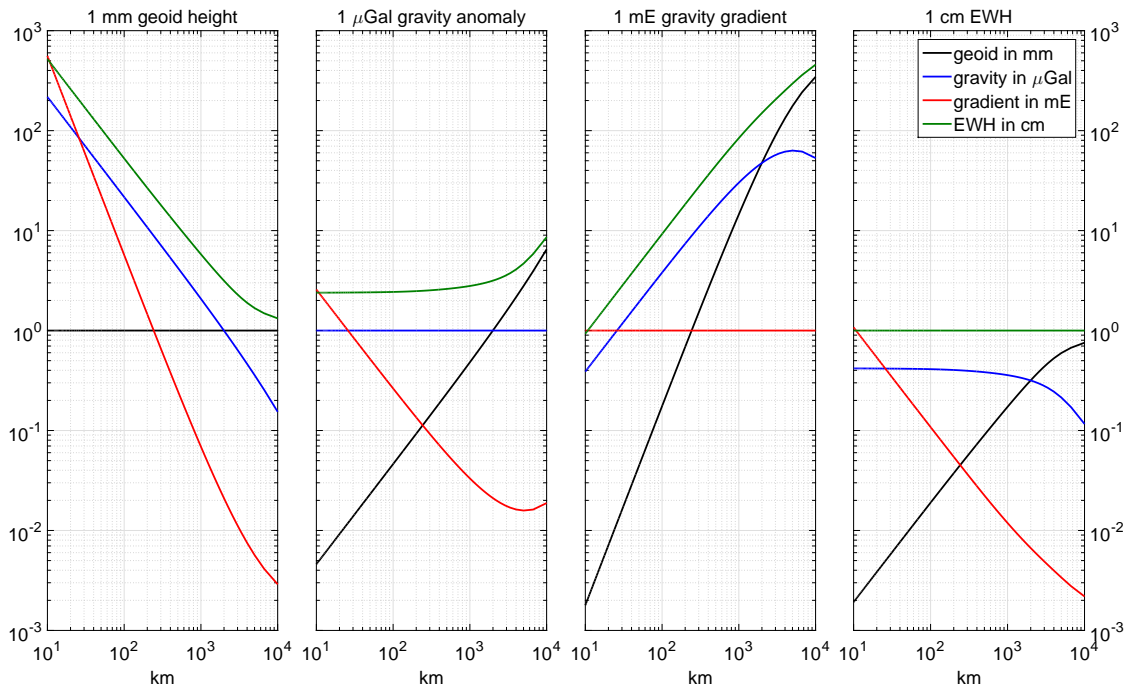


Figure 3.1: Conversion between geoid heights in mm, gravity anomalies in  $\mu\text{Gal}$ , gravity gradients in mE and EWH in cm depending on the spatial resolution in km. For example, 1 mm geoid height (left) corresponds to the blue line in terms of gravity anomalies in  $\mu\text{Gal}$ .

## 3.2 Translation to Monthly Resolution

The next step is the translation of the different required temporal resolutions to the basic temporal resolution of 1 month. This period is chosen because of the max. required spatial resolution in the SR of 50 km (cf. Tab. 3.2). Assuming a homogenous global groundtrack pattern, this requires a minimum number of revolutions of 401. And for satellite altitudes lower than 500 km (more than 15 revolutions per day), this is reached after 1 month at the latest.

The MO of course must take into account also the temporal resolutions of the SR, which are higher than one month, i.e. 1 and 10 days (cf. Tab. 3.2). After 1 day any satellite with an altitude smaller than 500 km will reach a near homogeneous global coverage. This also holds for periods around 10 days if the orbit of the NGGM has a sub-cycle with this period. Furthermore, science requirements regarding static and trend signals require a long mission duration of at least 11 years. As this covers one full solar cycle, it helps to separate the results from systematic effects related to external disturbances (e.g. atmospheric drag and solar radiation).

With formal error propagation the translation to the basic temporal resolution is assessed. A time depending signal with unit U is observed with a regular temporal sampling ( $k$  observations per year) over a period of  $N$  years. Hence, in total there are  $n = k \cdot N$  observations. The observations  $\hat{\mathbf{I}}$  are assumed to be independent and to have the same accuracy. For this time series a constant and linear term  $\hat{p}_0$  and  $\hat{p}_1$  shall be estimated in a least-squares sense. The functional model is  $\hat{\mathbf{I}} = \hat{p}_0 + \hat{p}_1 \cdot t$  with the time vector  $t_i = (i - n/2)/k$  years (reference epoch  $t = 0$  in the middle of the period) and  $i = 0, \dots, n - 1$ . The formal errors of the parameters  $\hat{p}_0$  and  $\hat{p}_1$  are the square root of the diagonal of the inverse normal equation matrix, i.e. the variance co-variance matrix of the unknown parameters  $Q_{\hat{p}\hat{p}}$ . The matrix  $Q_{\hat{p}\hat{p}}$  can be derived analytically to

$$Q_{\hat{p}\hat{p}} = \frac{1}{n \sum t_i^2 - (\sum t_i)^2} \begin{pmatrix} \sum t_i^2 & -\sum t_i \\ -\sum t_i & n \end{pmatrix}. \quad (3.2)$$

Thereof, depending on the standard deviation of each single observation  $\sigma_i$  with unit U the standard

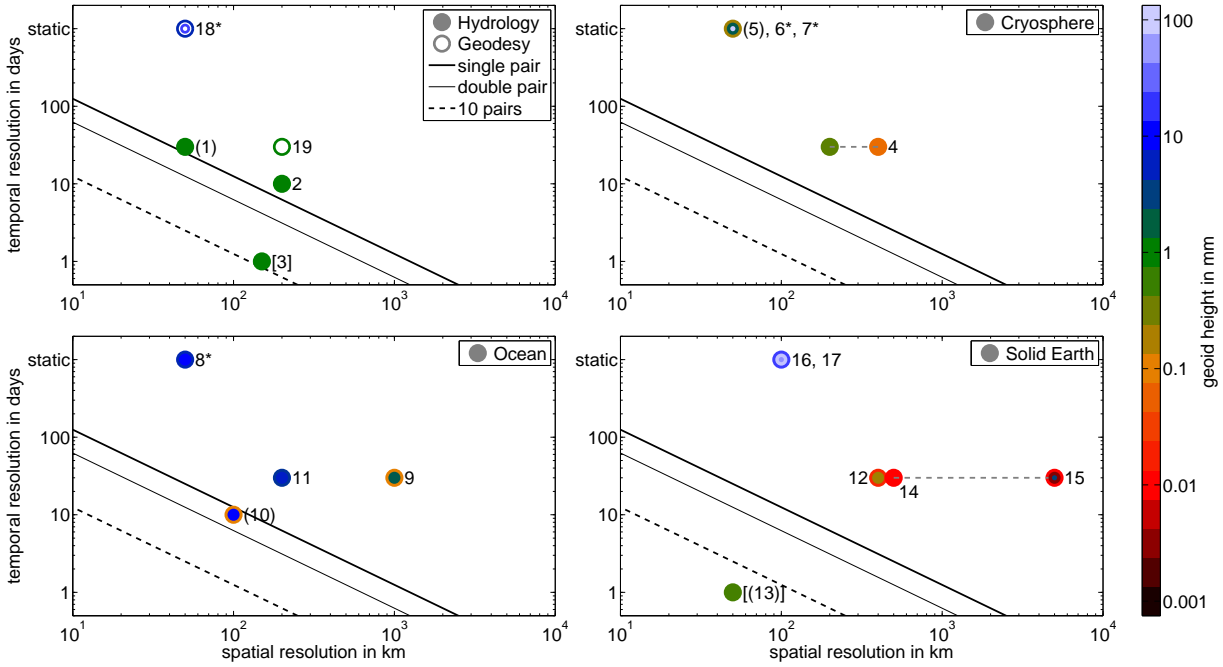


Figure 3.2: Science requirements for the five different areas in mm geoid heights. Top left: hydrology and geodesy. Top right: cryosphere. Bottom left: ocean. Bottom right: solid Earth. The SR, which are not achievable with the specified temporal and spatial resolution with the NGGM are marked with [ ] (cf. Fig. 3.2). The SR, which are not achievable with the required accuracy with the NGGM are marked with ( ). And the requirements, which are only achievable with the NGGM fulfilling the optimal mission objectives are marked with \* (cf. Fig. 3.3).

deviations for the constant term  $\sigma_{\hat{p}_0}$  and the linear term  $\sigma_{\hat{p}_1}$  result in

$$\begin{aligned}\sigma_{\hat{p}_0} &= \sigma_i \sqrt{\frac{n^2 + 2}{n(n^2 - 1)}} \\ \sigma_{\hat{p}_1} &= \sigma_i \sqrt{\frac{12k^2}{n(n^2 - 1)}}.\end{aligned}\tag{3.3}$$

The unit for  $\sigma_{\hat{p}_0}$  is U and for  $\sigma_{\hat{p}_1}$  it is U/year. With Eq. (3.3) the science requirements for all static and secular signals are converted to monthly requirements. With monthly observations ( $k = 12$ ) and a 11 years mission duration ( $N = 11$ ,  $n = kN = 132$ ) a formal standard deviation of the trend of  $\sigma_{\hat{p}_1} = 1$  U/year is reached for standard deviations for each monthly observation of  $\sigma_i = 36.5$  U. And a formal standard deviation of the mean of  $\sigma_{\hat{p}_0} = 1$  U is reached for  $\sigma_i = 11.5$  U. For the conversion of the science requirements a safety factor of 2 is applied leading to  $\sigma_i (\sigma_{\hat{p}_1} = 1 \text{ U/year}) = 20$  U and  $\sigma_i (\sigma_{\hat{p}_0} = 1 \text{ U}) = 6$  U (one significant digit). The safety factor accounts for error effects, which are neglected here (e.g. correlated observations, imperfect homogenous global coverage, estimation of harmonic signals in addition to  $\hat{p}_0$  and  $\hat{p}_1$ ).

For the signals with higher required temporal resolution than 1 month a simple  $\sqrt{n}$ -rule is applied for the translation to monthly requirements. To derive the monthly requirement for ground water (SR2) for example the 10 days requirement is divided by  $\sqrt{3}$  as there are three times more observations.

The consolidated SR in terms of signals of interest with required spatial and temporal resolution and required accuracy and with the translated monthly geoid accuracy are shown in Tab. 3.2. The selection of these signals is based on Sneeuw et al. (2005), Gruber et al. (2014), and Panet et al. (2013). A graphical representation of the SR in geoid heights is shown in Fig. 3.2. The maximum required spatial resolutions is 50 km (e.g. for ice sheets) and the max. temporal resolution is daily (e.g. for soil moisture).

The values are compared with the achievable spatio-temporal resolution of a single- and double-pair (solid black lines). These lines are derived from the assumption that a single satellite performs 16 revo-

*Table 3.2: Science requirements (SR) for the NGGM in five different areas with required spatial and temporal resolution and the required accuracy. The last column contains the required monthly geoid accuracy derived from unit conversion (cf. Fig. 3.1) and scaling according to formal error propagation. The SR, which are not achievable with the required temporal and spatial resolution with the NGGM are marked with [ ] (cf. Fig. 3.2). The SR, which are not achievable with the required accuracy with the NGGM are marked with ( ). And the requirements, which are only achievable with the NGGM fulfilling the optimal mission objectives are marked with \* (cf. Fig. 3.3).*

Area	SR Number	Signal	Required spatial resolution in km	Required temporal resolution	Required accuracy	Required monthly geoid accuracy in mm	
Hydrology	(1)	Snow, precipitation, dams, run-off, evapo-transpiration	50	monthly	1 mm geoid	1	
	2	Ground water	200	10 days	1 mm geoid	0.6	
	[3]	Soil moisture	150	1 day	1 mm geoid	0.2	
	3 <sup>r</sup>	Soil moisture (r=reduced res.)	150	5 days	1 mm geoid	0.4	
Cryosphere	4	Ice mass balance	200 to 400	monthly	1 to 10 cm EWH	0.07 to 0.4	
	(5)	Bottom topography, ice compaction	50	quasi-static	0.01 to 0.1 mGal gravity	1 to 10	
	6*	Geoid for sea ice thickness	50	static	100 mm geoid	600	
Ocean	7*	Ice sheets (rock basement)	50	static	1 to 5 mGal gravity	100 to 600	
	8*	Narrow currents, topographic control, coastal currents, eddies, ocean fronts	50	quasi-static	5 to 10 mm geoid	30 to 60	
	9	Basin scale mass change	1,000	monthly	0.1 to 2 mm geoid	0.1 to 2	
	(10)	Bottom barotropic currents	100	10 days	0.1 to 10 mm geoid	0.06 to 6	
	11	Global sea level change	200	secular	0.2 to 0.3 mm/year geoid	4 to 6	
	Solid Earth	12	Glacial isostatic adjustment	400	secular	1 to 10 $\mu\text{m}/\text{year}$ geoid	0.02 to 0.2
		[(13)]	Co-/Postseismic deformation, slow silent earthquakes	50	1 day	0.5 mm geoid	0.1
	Geodesy	14	Plate tectonics, mantle convection, volcanos	500 to 5,000	monthly	0.01 mm geoid	0.01
		15	Core motion	5,000	monthly	1 nGal to 1 $\mu\text{Gal}$ gravity	0.003 to 3
		16	Lithosphere (continental and oceanic)	100	static	0.5 to 2 mGal gravity	100 to 500
17		Seismic hazards	100	static	1 mGal gravity	300	
18*		GNSS leveling	50 km	static	5 to 20 mm geoid	30 to 100	
	19	Unified height systems, satellite orbits	200 km	monthly	1 mm geoid	1	

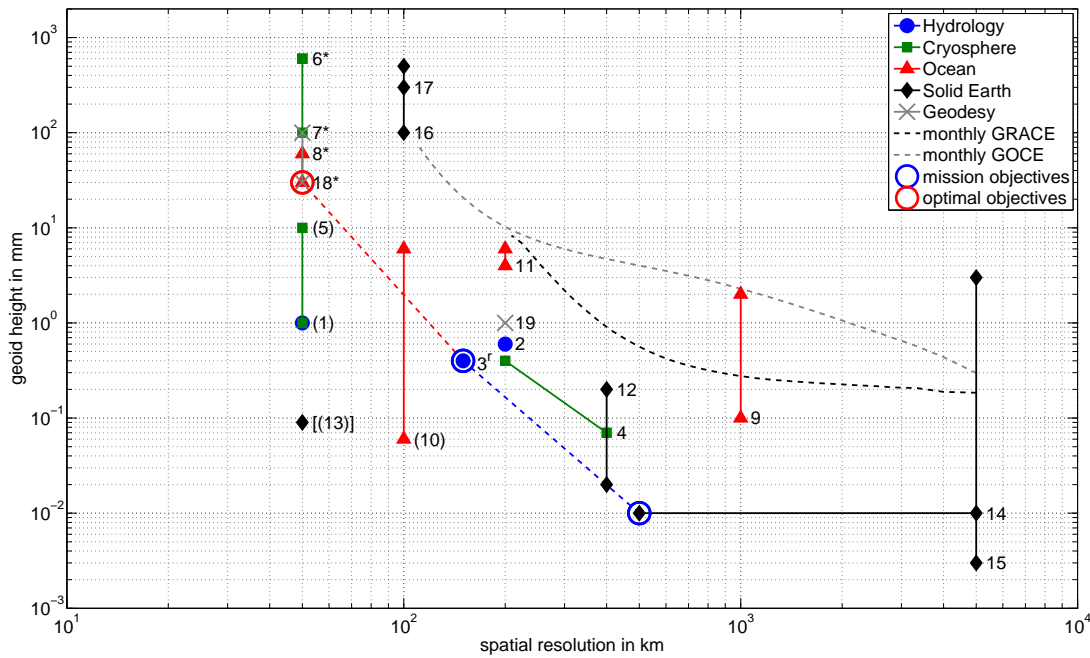


Figure 3.3: Monthly requirements in mm geoid heights and mission objectives. The SR, which are not achievable with the specified temporal and spatial resolution with the NGGM are marked with [ ] (cf. Fig. 3.2). The SR, which are not achievable with the required accuracy with the NGGM are marked with ( ). And the requirements, which are only achievable with the NGGM fulfilling the optimal mission objectives are marked with \* (cf. Fig. 3.3).

lutions per day and that this is sufficient to estimate a global gravity field up to  $l_{max} = 16$  corresponding to a spatial resolution of 1,250 km. With a second orbit which doesn't follow the same groundtrack the spatial resolution is doubled. It can be seen, that SR3 (soil moisture) and SR13 (co-/postseismic deformation, slow silent earthquakes) are not achievable with a single- and a double-pair with the specified resolution. By decreasing the temporal resolution of these two requirements to the double-pair line, the achievable values for the NGGM can be approximated. This leads to achievable temporal resolutions of 5 days for SR3 (cf. SR3<sup>r</sup>) and 10 days for SR13. Doing so, it is clear that a NGGM with only one satellite or satellite pair will fulfil these SR only with reduced resolution (temporal and/or spatial). The translated monthly geoid requirements for the NGGM are shown numerically in the last column of Tab. 3.2.

### 3.3 Mission Objectives

In this section the mission objectives (MO) of the NGGM are derived from the SR. At first there is a need for a general MO assuring global coverage of the resulting gravity field models. This requires at least 1 polar orbit for the NGGM. The required geoid accuracy is formulated for different spatial resolutions for the basic temporal resolution of 1 month. The monthly SR are shown in the last column of Tab. 3.2 and in Fig. 3.3. Here, the SR are compared with mean monthly GRACE and GOCE-like (monthly repeat cycle) cumulative geoid errors. Compared to these current baselines, the NGGM shall fulfil significantly more SR.

A reasonable choice with respect to technical limits taking into account also the signal attenuation in satellite altitude are the chosen MO shown in blue and red circles. The blue circles mark the basic MO at spatial resolutions of 500 and 150 km. For the max. spatial resolution of the SR of 50 km the red circle represents the optimum high resolution MO. With the basic MO in blue more than half of the SR are fulfilled with the required temporal resolution (SR without brackets and \*) and with the optimal MO nearly 3/4 (SR without brackets). The signals related to the not fulfilled SR can only be

---

*Table 3.3: Mission Objectives (MO) for the NGGM.*

---

MO1	The gravity field solutions for different periods must provide global coverage.
MO2	The maximum monthly cumulative geoid error of the NGGM is 0.01 mm at a spatial resolution of 500 km and 0.4 mm at 150 km. Really nice to have would be a NGGM with 30 mm geoid accuracy for a spatial resolution of 50 km.
MO3	The orbital groundtrack distribution must be sufficient to retrieve global gravity field models after 5 days down to a spatial resolution of 150 km and after 10 days down to a spatial resolution of 100 km.
MO4	The minimum mission duration is 11 years (one solar cycle).

---

observed with reduced resolution or accuracy. To account for the higher temporal resolution of SR2, SR3<sup>r</sup>, SR10, and SR13 the third MO of the NGGM requires a homogenous global coverage after 5 and 10 days which is achievable by a proper sub-cycle choice. The condition for the formal error propagation in the previous section is a minimum mission duration of 11 years, which is the last MO. The MO for the NGGM are given in Tab. 3.3.

A single satellite (pair) is not able to provide the required spatial resolution for the short term MO3. With the approximation of the previous section a spatial resolution of 250 km can be reached with a single LEO after 5 days and 130 km after 10 days. This means that a constellation of at least two satellites or satellite pairs is required providing spatial resolutions of 130 km and 63 km after 5 and 10 days respectively. From this point of view the max. required spatial resolution after one month of 50 km is not crucial. Theoretically even a single satellite (pair) with monthly repeat cycle provides enough observations to estimate SH coefficients at least up to  $l_{\max} = 400$ , corresponding to a spatial resolution of 50 km.



## 4 Basic Scenarios and Instrument Requirements

In this chapter requirements are derived for the key sensors for selected basic mission scenarios (Sec. 4.1). These requirements ensure that each scenario is able to fulfil the science requirements and mission objectives defined in Chap. 3. In Sec. 4.2 typical noise characteristics are analyzed. Based on these sensor noise ASDs instrument requirements are determined from semi-analytical simulation results for selected mission scenarios.

### 4.1 Basic Scenarios

A large number of different NGGM scenarios are analysed for both low-low SST and SGG missions, e.g. in Anselmi (2010), Wiese et al. (2012), Elsaka (2012), Iran Pour (2013), Reubelt et al. (2014), and Gruber et al. (2014). The most promising scenarios with respect to both scientific and technical issues are low-low SST missions (single and double pairs) with a laser ranging instrument. For single low-low SST pairs the weakness of an in-line formation is reduced with so-called Pendulum formations. Adding a second pair in an inclined orbit (Bender-type formation) further increases the isotropy of the error spectrum, and a higher resolution can be achieved. The third chosen basic scenario in this thesis is the combination of low-low SST and radial SGG.

The inter-satellite vectors of other low-low SST scenarios like the so-called Cartwheel or Helix (Wiese et al., 2009; Anselmi, 2010; Reubelt et al., 2014) contain also a radial component. But the technological complexity of these scenarios is much higher. This is why they are not addressed in this thesis. Furthermore, there is a promising next NGGM concept developed in the context of the GETRIS project (Schlicht et al., 2014). One component of GETRIS are links between geostationary (GEO) satellites and LEOs with which the range is determined with micrometer accuracy. First simulations based on the LCLA show that such a precise high-low SST outperforms a GRACE-like scenario (Schlie et al., 2014). This is reasonable, because the inter-satellite vector between LEO and GEO contains more isotropic radial information especially at low latitudes than a polar in-line low-low SST pair. This study show another big advantage of this precise GEO-LEO tracking concept for gravity field determination. If more LEOs are tracked from the GEOs, the temporal resolution can be increased down to a few days.

For each of the basic scenarios repeat cycles are determined according to the mission objectives. It is required to have a monthly repeat orbit with sub-cycles of approximately 5 and 10 days. In general,

*Table 4.1: Parameters for the four basic repeat orbits. Polar orbits ( $I = 89^\circ$ ) are marked with p, inclined orbits ( $I = 70^\circ$ ) with i.*

Name	$N_{\text{day}}$	$N_{\text{rev}}$	Altitude in km	
			polar	inclined
ORB1p/ORB1i	31	491	299	268
ORB2p/i	31	484	363	333
ORB3p/i	31	478	420	390
ORB4p/i	31	471	487	458

the lowest altitude is the best for the NGGM. But the assessment of a NGGM always has not only scientific requirements, but also technical and financial constraints. Therefore for each possible NGGM the choice of the orbital altitude is restricted to higher altitudes than a specific threshold. From a technical point of view the main effects of having a lower altitude is increasing demand of power or fuel and decreasing mission duration.

Another impact of orbital altitude are SH order resonances which increase the temporal aliasing error effect at specific SH order bands. This effect is described in Murböck et al. (2014) and further addressed in Chap. 6 and 7. The main conclusions of Murböck et al. (2014) contain four optimal orbital altitude bands for polar orbits. The repeat cycles within these bands lead to the smallest temporal aliasing error effects. For each of these four bands one repeat cycle is chosen with the required properties regarding sub-cycles. The parameters of the four basic polar and inclined repeat orbits are given in Tab. 4.1. Each of them is a fast-skipping orbit (cf. Iran Pour (2013) and Sec. 2.3.2) and has subcycles of 5 and approximately 10 days. Each of the four repeat cycles is chosen from a set of near monthly repeat cycles in one of the four altitude bands. There are several other possible orbit choices which lead to very similar results. Of course for 31 days more repeat cycles in one altitude band can be found, because it is a prime. The noise ASDs defined in Sec. 2.4.3 are the basic noise models for the ranging instrument (Eq. (2.46)), the accelerometers (Eq. (2.47)) and the gradiometer (Eq. (2.44)). With this simulation setup in the following the instrument requirements are estimated for the four altitudes.

For each low-low SST pair a reference inter-satellite distance of  $\rho_0 = 100$  km is defined. On the one hand a larger distance increases the sensitivity especially in the low SH degrees (Gruber et al., 2014). On the other hand there is the effect of common mode attenuation which leads to increased errors for SH degrees (Sneeuw, 2000)  $l \approx k2\pi R/\rho_0$  with integer  $k$ . As for the NGGM a max. spatial resolution of 50 km is formulated (MO2), there shall be no attenuation for  $l < 400$ . Hence it is  $\rho_0 < 100$  km. Of course the choice of the distance has also technical constraints, because the laser ranging instrument accuracy depends on the absolute range as well. For the laser described in Gruber et al. (2014) 100 km was chosen, fulfilling the defined instrument requirement.

#### 4.1.1 Double pair (Bender-type)

The low-low SST double pair in a Bender-type constellation has big advantages compared to a single in-line pair (Bender et al., 2008). It has been studied in Visser et al. (2010), Anselmi (2010), Wiese et al. (2012), Elsaka (2012), and Reubelt et al. (2014). The Bender-type constellation provides more isotropic measurements and the temporal (spatial) resolution is doubled for the same spatial (temporal) resolution. For the NGGM one polar pair is needed because global coverage is required. The selection of an optimal inclination  $I_{\text{opt}}$  of the inclined pair can be assessed with respect to different parameters. For smaller  $I_{\text{opt}}$  the combined solution gets more isotropic but the errors in high latitudes (observations only from the polar pair) increase. Although the MOs (Tab. 3.3) are formulated in terms of global mean geoid accuracy requirements the SRs must not be forgotten. Especially the SRs for the cryosphere concern the polar areas and Greenland.

Wiese et al. (2012) and Gruber et al. (2014) estimate from independent simulations an optimal inclination of the inclined pair of  $70^\circ$  to  $75^\circ$ . For this thesis  $70^\circ$  is chosen for which in Fig. 2.8 semi-analytical simulation results are shown for ORB3p/i. The SH degree RMS curves show an average improvement by a factor of 10 when adding the inclined to the polar pair. At a spatial resolution of 150 km the factor is decreased to 5. The improvement is even larger for non-stochastic error contributions like temporal aliasing from background model errors. Different independent simulations in Gruber et al. (2014) taking such errors into account estimate a factor of 20 for the same spatial resolution.

In Tab. 4.1 the double pair for each altitude consists of two pairs with the same repeat cycle. The same repeat cycle with different inclination is found in a different altitude, in this case the inclined orbits are 30 km lower than the polar ones. The choice of the repeat cycle in this case is driven by the MOs (Tab. 3.3). Further investigations could also take gravity field retrieval performances into account.

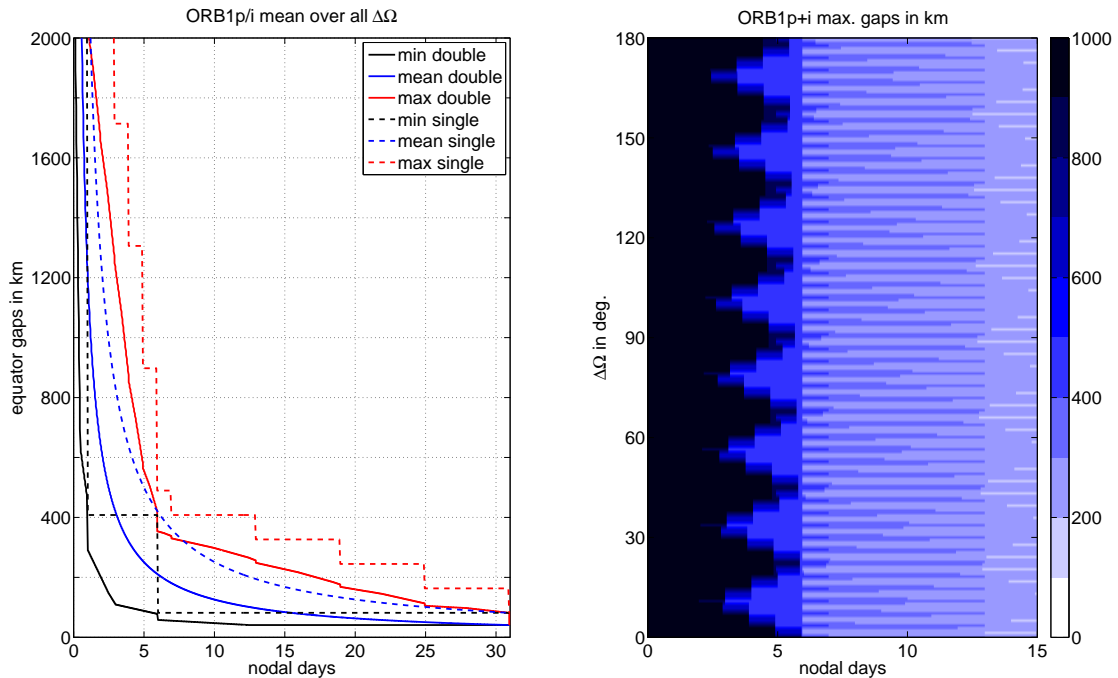


Figure 4.1: Equator gap statistics for the single polar and the double Bender-type pair of ORB1 (cf. Tab. 4.1). Left: mean over all  $\Delta\Omega$  (cf. Eq. (4.1)) for single and double pair. Right: max. gaps for the double pair and  $\Delta\Omega < 180^\circ$ .

Especially for certain processing strategies with the aim of reducing temporal aliasing the choice of the two repeat cycles should be further elaborated. An example for such a strategy is the estimation of low resolution gravity fields at short time intervals as described in Wiese et al. (2011). In Sec. 6.2 there is a discussion of this method regarding the variances of geophysical signals at certain frequencies.

With a double pair the spatial resolution can be doubled compared to a single pair for the same temporal resolution. Having the same repeat cycles for the polar and inclined pair as defined in Tab. 4.1 this is simply ensured by putting the inclined pair orbit tracks between the polar ones. The separation between two consecutive ascending tracks after one full repeat cycle is  $360/N_{\text{rev}}$  for both pairs. Doubled spatial resolution with homogeneous groundtrack coverage is reached for the double pair if the separation between the ascending nodes is

$$\Delta\Omega = (2k - 1) \pi / N_{\text{rev}} \quad (4.1)$$

with integer  $k$ . Hence, analogously to Fig. 2.3 for a single pair, Fig. 4.1 shows the equator gap statistic for the double pair of ORB1. The evolution averaged over all  $\Delta\Omega$  (left) compares the single polar with the double pair. The sub-cycles can clearly be seen in the single pair max. gaps line (red dashed). After the full cycle all lines (min, mean and max) for the single and double pair coincide at 82 km and 41 km, respectively. The max. gaps dependency on  $\Delta\Omega$  (right) is nearly periodic with  $22.5^\circ = 360^\circ/16$  which is related to the number of revolutions per day. In the first 6 days within each  $22.5^\circ$  there are smaller max. gaps for  $\Delta\Omega$  close to  $180^\circ/16$ . Above 6 days the dependency of the max. gaps on  $\Delta\Omega$  is not so strong which is of course driven by the gap statistic of the single pair (left).

### 4.1.2 Pendulum

The Pendulum scenario is investigated and analysed regarding gravity field retrieval performance in Anselmi (2010), Elsaka (2012), and Reubelt et al. (2014). In a Pendulum formation with two satellites at the same altitude the trailing satellite performs periodic movements in cross-track direction with respect to the leading satellite. Therefore it leads to global multidirectional observations along the LoS between the two satellites. It is favorable to implement the Pendulum with a constant shift in  $\Omega$  and not in  $I$ . A shift in  $\Omega$  improves the observation geometry in lower latitudes whereas the shift in  $I$

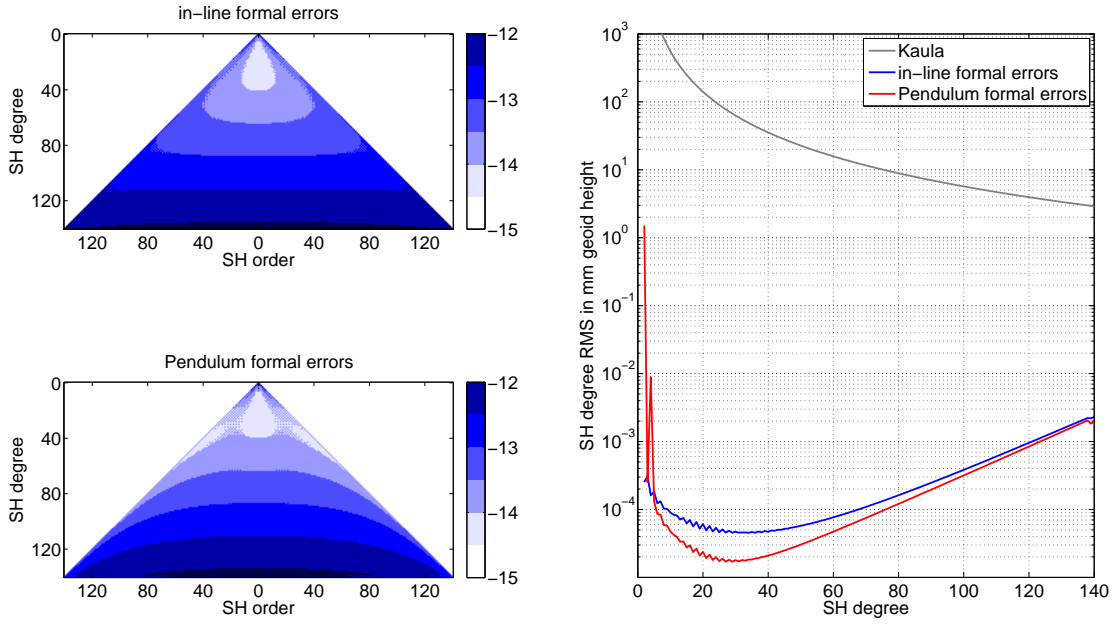


Figure 4.2: Unit-less formal errors ( $\log_{10}$ ) for low-low SST in an in-line (top left) and a Pendulum (bottom left) formation with opening angle of  $23^\circ$  on ORB1p (cf. Tab. 4.1). Both single pairs use the same observation noise assumption (Fig. 4.5 for ORB1). Right: SH degree RMS in mm geoid height for the two formations in comparison with static Kaula-rule.

has this effect in high latitudes. However, at high latitudes the observations during one repeat period are anyhow multidirectional, because satellites cross the poles along different meridians. Furthermore different  $I$  would require more orbit control manoeuvres over a long period in order to keep a stable formation, because of different ascending node precession due to the Earth's flattening. The magnitude of the pendulum motion depends on the angle  $0^\circ \leq \alpha < 90^\circ$ , which is the smallest angle between the LoS and the velocity vector of the leading satellite. For  $\Omega$  shifted Pendulum scenarios the largest  $\alpha$  occurs at the equator. The most isotropic observations for a Pendulum are reached for  $\alpha = 45^\circ$ . Hence for a polar orbit during one repeat cycle the LoS vectors for ascending tracks are perpendicular to descending ones in low latitudes.

But there is a technical constraint for  $\alpha$ . For increasing  $\alpha$  the absolute range rate  $\dot{\rho}$  increases to more than 40 m/s for LEO Pendulum scenarios with  $\alpha = 45^\circ$ . For an inter-satellite laser interferometer as on GRACE-FO and assumed in Reubelt et al. (2014) the limit for the absolute range rate  $|\dot{\rho}|$  is 10 m/s. For a constant along-track separation  $\rho_x$  (constant  $\Delta M$ ) the range depending on the argument of latitude  $u$  can be approximated by

$$\rho(u) = \frac{\rho_x}{2} \left( \frac{1}{\cos \alpha} + 1 \right) + \frac{\rho_x}{2} \left( \frac{1}{\cos \alpha} - 1 \right) \cos(2u). \quad (4.2)$$

Then the range rate reads

$$\dot{\rho}(u) = \rho_x n \left( 1 - \frac{1}{\cos \alpha} \right) \sin(2u) \quad (4.3)$$

with the mean motion  $n$  from Eq. (2.22).

From Eq. (4.2) and (4.3) it is clear that the extreme range values for a polar Pendulum occur at the equator (maximum) and at the poles (minimum). There, the range rate is zero, and it reaches its absolute maxima at latitudes of  $\pm 45^\circ$ . Hence, for polar Pendulum formations between 200 and 600 km altitude with  $\rho_x = 100$  km the technical constraint of  $|\dot{\rho}| < 10$  m/s is satisfied for  $\alpha < 24^\circ$ . In Gruber et al. (2014) there is a comparison of polar Pendulum formations ( $\alpha \in \{7^\circ, 24^\circ, 45^\circ\}$ ) with a double Bender-type low-low SST pair at the same altitude. For the inclined pair of the double pair  $I = 70^\circ$  is chosen. The simulations take the same colored instrument noise for all pairs and also deterministic

error contributions from temporal aliasing into account. Up to  $l_{\max} = 90$  the double pair exceeds the  $24^\circ$ -Pendulum by a factor of 2 and the  $7^\circ$ -Pendulum by a factor of 5.

A comparison of the in-line formation with the Pendulum formation with  $\alpha = 23^\circ$  for the basic single polar orbit ORB1p is assessed with the LCLA up to  $l_{\max} = 140$ . Assuming the same observation noise according to Fig. 4.5 with this comparison the effects of the improved observation geometry can be analysed. Figure 4.2 shows the unit-less formal errors ( $\log_{10}$ ) of the two formations for each SH coefficient (left) and in terms of SH degree RMS (right). The improved observation geometry of the Pendulum formation (bottom left) leads to decreased formal errors mainly in the sectorials (where the in-line formation is less sensitive). The formal errors at the sectorials for constant SH degree are even smaller than the ones at the zonals.

The SH degree RMS curves show an improved sensitivity of the Pendulum wrt. the in-line formation nearly for all SH degrees (maximum around  $l = 30$  by a factor of more than 2.5). The improvement decreases with SH degree to nearly the same sensitivity at  $l = 140$ . But for the SH degree 2 and 4 the Pendulum shows worse sensitivity which is due to the two zonal coefficients  $\bar{C}_{20}$  and  $\bar{C}_{40}$  (cf. Fig. 4.2, bottom left).

Due to a more complex attitude and orbit control from a technological point of view the Pendulum formation is more difficult to realize than a Bender-type double pair. But of course for a double-pair more resources are needed because of having four satellites instead of two. Furthermore, to put the satellites in different inclinations a second launch vehicle might be required.

### 4.1.3 Combination of low-low SST and radial SGG

Another possibility to overcome the weak observation geometry of a single in-line pair is the combination with radial SGG. Because of its isotropic characteristic, radial SGG ( $V_{rr}$ ) with sufficient accuracy helps to increase sensitivity especially in the sectorials where the single in-line pair is weak. The simulation environment consists of a low-low SST pair like ORB1p (cf. Tab. 4.1) with total observation noise ASD from Eq. (2.48) combined with radial SGG observations on one of the two satellites.

The  $V_{rr}$  accuracy must be on the level of  $1.2 \cdot 10^{-5} \text{ E}/\sqrt{\text{Hz}}$  to reach equal contribution as low-low SST to the total cumulative geoid error up to  $l_{\max} = 134$  of 0.7 mm. The results of the SANA simulations on this combination is shown in Fig. 4.3. The typical error characteristics of the two contributions can clearly be seen when comparing the formal errors (left, top and center). The SH degree RMS curves (right) indicate that the  $V_{rr}$ -only solution exceeds low-low SST-only above  $l = 30$ . Compared to the low-low SST solution the combined solution is improved by a factor of approximately 4. A more detailed view on the contribution of  $V_{rr}$  to this combination is given by the relation between the variances of the combined and the  $V_{rr}$ -only solution (bottom left). For a wide spectrum around the zonals the  $V_{rr}$ -contribution is less than 20%, but it increases to 100% for the sectorials.

The SH degree RMS error curves in Fig. 4.3 (right) are compared with an approximation of the signal SH degree variances of the Earth's gravity field given by Kaula,

$$\sigma^2(l) = \frac{1.6 \cdot 10^{10}}{l^3}. \quad (4.4)$$

Hence, the Kaula-rule for SH degree RMS reads

$$\sqrt{\frac{\sigma^2(l)}{2l+1}}. \quad (4.5)$$

As radial SGG in general has less error increase with increasing SH degree as low-low SST, the contribution of  $V_{rr}$  to such a combination increases with the SH degree. Furthermore, the impact of radial SGG is larger in the case of deterministic errors such as, for example, temporal aliasing. An analysis on this issue is elaborated in Anselmi (2010). On the one hand this means that, aiming for a high

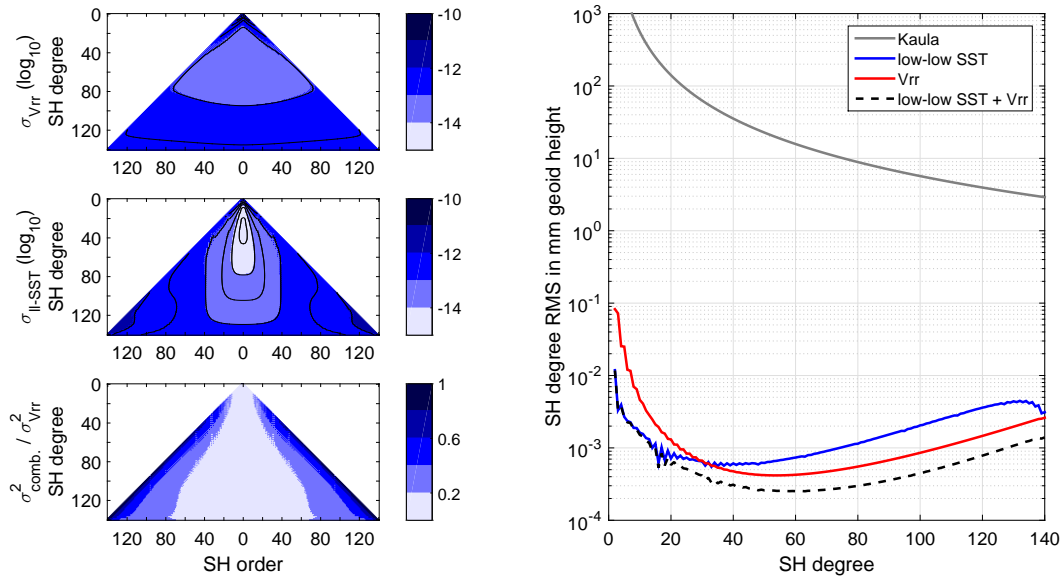


Figure 4.3: Unit-less formal errors ( $\log_{10}$ ) and contribution analysis for the combination of low-low SST and  $V_{rr}$  on ORB1p (cf. Tab. 4.1). The noise ASD of the low-low SST observations is given in Eq. (2.48). For  $V_{rr}$  the noise ASD in Eq. (2.44) is scaled to reach 50% of the total combined cumulative geoid error at  $l = 134$  ( $1.2 \cdot 10^{-5} \text{ E}/\sqrt{\text{Hz}}$  for  $1 \text{ mHz} < f < 100 \text{ mHz}$ ). Left: formal errors for  $V_{rr}$  (top) and low-low SST (center) and the contribution of  $V_{rr}$  to the combined solution. Right: SH degree RMS in mm geoid height of the two contributions and the combination in comparison with static Kaula-rule.

spatial resolution gravity field (down to 50 km) this combination might be a promising candidate for the NGGM. But on the other hand, due to current technical limits it is not reasonable to assume an accuracy for the NGGM  $V_{rr}$ -accuracy more than 1,000 times better than that of GOCE. A gradiometer design with improved sensitivity compared to the GOCE gradiometer by a factor of 10 is described in Zhu et al. (2013).

## 4.2 Instrument Requirements

This thesis deals with mission scenarios with similar instrument concepts as the successfully flown and planned mission scenarios GOCE and GRACE-FO. There are other promising instrument concepts, which in the future might be able to reduce the noise level of current instruments. In Reubelt et al. (2014) alternative ranging measurement concepts are discussed as, for example, interferometry with optical frequency combs (Cui et al., 2009). But in this thesis the currently available instrument concepts are selected. Furthermore, in this section only the key instruments are addressed, which do not include Global Navigation Satellite System (GNSS) receivers. Their contribution to the total error budget and corresponding requirements are discussed in Chap. 5.

The instrument requirements for all basic scenarios (Pendulum, Double pair Bender-type and SST-SGG combination) are derived for the weakest scenario, the single polar in-line pair. Hence, the instrument requirements assure that all scenarios have lower cumulative geoid errors than required in MO2. MO2 is divided regarding spatial resolution: there are two objectives for low and medium resolution (500 and 150 km) and one for high resolution (50 km). At the end of this section the high resolution requirement is addressed, but the instrument requirements at first are determined for low and medium spatial resolution based on SANA simulations. The approach for this investigation is the following (cf. Tab. 4.2).

The total observation noise of a polar in-line single-pair depends mainly on the errors of the two key instruments, i.e., the ranging instrument (SST) and the accelerometers (ACC). The reference noise ASDs for these noise contributions are given in Eq. (2.46) and (2.47). Applying a safety factor of 2 the total geoid error must not sum up to more than 50% of the requirements formulated in MO2. The error

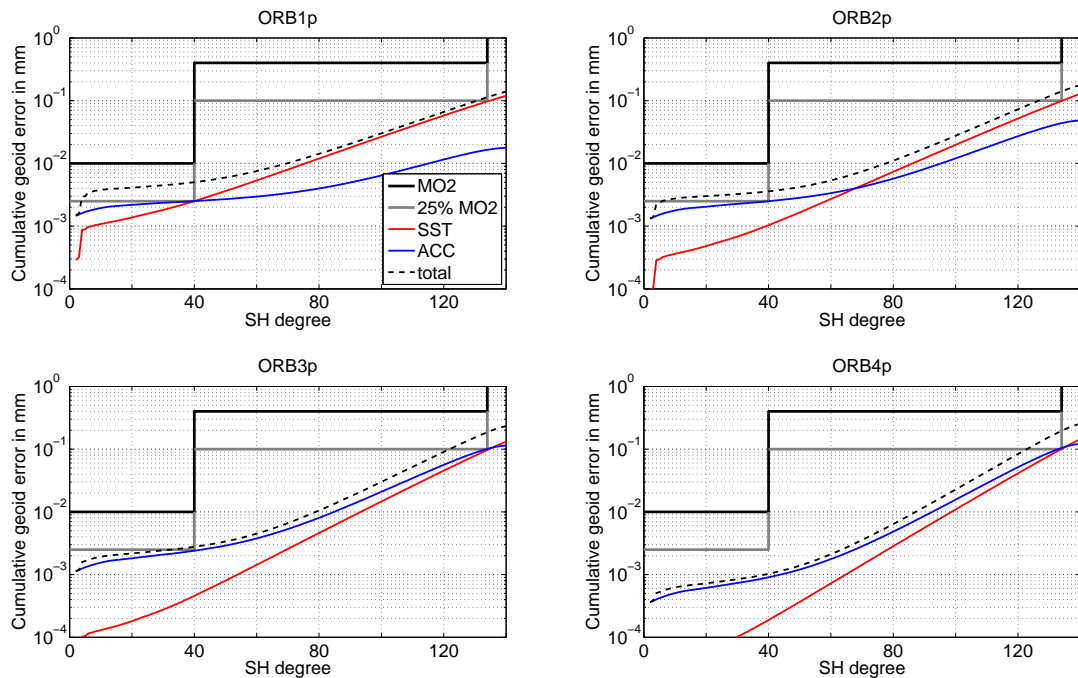


Figure 4.4: Cumulative geoid errors in mm for the 4 basic single polar in-line pairs (cf. Tab. 4.1) with required noise levels for the ranging instrument (SST), the accelerometer (ACC) and the total noise. The required noise levels of SST and ACC are scaled in order to reach 25% of MO2 for 500 km ( $l = 40$ ) and 150 km ( $l = 134$ ) spatial resolution.

contributions of SST and ACC then account for 25% each. As the formal errors depend linearly on the scale factor of the noise ASDs, the instrument requirements can be determined from only one set of simulations based on the reference noise ASDs. With the SANA the formal errors for the four polar in-line pairs (cf. Tab. 4.1) are estimated up to  $l_{\max} = 140$  separately for SST and ACC. Then the scale factors are determined from dividing the 25% MO2 values ( $2.5 \mu\text{m}$  for  $l = 40$  and  $0.1 \text{ mm}$  for  $l = 134$ ) by the cumulative geoid errors. As the cumulative errors must be below both requirements for  $l = 40$  and  $l = 134$ , the smallest scale factor is needed to determine the instrument requirements.

Figure 4.4 shows the cumulative geoid error for the four single in-line polar pairs with the corresponding scale factors applied. Therefore the SST and ACC error curves meet one of the 25% requirements exactly. It can be seen that this approach leads to different error contributions of the two sensors. Whereas for the two lower pairs (ORB1p and ORB2p) the ACC geoid error contribution dominates only the lower SH degrees, it dominates nearly the whole degree range for the higher pairs. Furthermore it can be seen, that the total error reaches at the maximum 50% of the requirements of MO2. As the other basic scenarios have improved sensitivity compared to a single in-line polar pair, they fulfil MO2 for 500 and 150 km spatial resolution as well.

Table 4.2: Approach for deriving the NGGM instrument requirements for the two key instruments, the ranging instrument (SST) and the accelerometer (ACC).

1. Basic single polar in-line pairs (Tab. 4.1).
2. Reference SST/ACC noise ASDs (Eq. (2.46) and (2.47)).
3. SANA simulations separately for SST and ACC.
4. Cumulative geoid errors  $\kappa_{\text{cum}}(l = 40, l = 134)$  for reference SST/ACC noise (Eq. (2.10)).
5. Scale factors  $f(l = 40, l = 134) = 25\% \text{ MO2}(l = 40, l = 134) / \kappa_{\text{cum}}(l = 40, l = 134)$
6. SST/ACC instrument requirements: reference noise ASD scaled by  $\min(f(l = 40, l = 134))$

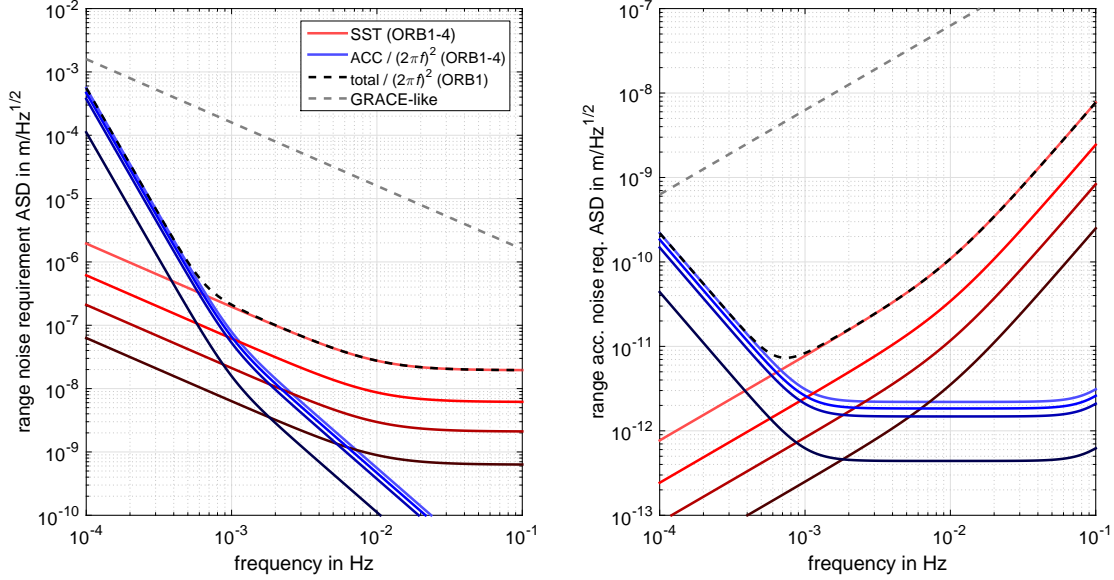


Figure 4.5: Required noise ASDs for SST and ACC compared with a GRACE-like accuracy in terms of ranges (left) and range accelerations (right). The SST and ACC noise ASD requirements for ORB1 to ORB4 are shown from light to dark in red and blue respectively (cf. Tab. 4.3)

The corresponding required noise levels for SST and ACC are given in Tab. 4.3. For each scenario (altitude) the given number for SST replaces the factor  $1.5 \cdot 10^{-8}$  of the noise ASD in Eq. (2.46). For ACC it replaces the factor  $4 \cdot 10^{-11}$  in Eq. (2.47). A graphical representation of the noise ACC requirements for the four scenarios is shown in Fig. 4.5 in comparison with a GRACE-like range rate accuracy of  $1 \mu\text{m/s}$ , transformed to ranges and range accelerations respectively.

Obviously, to reach the same cumulative geoid error with a higher low-low SST scenario increased instrument accuracies are necessary. The required SST noise level for ORB1 (299 km polar altitude) is nearly the same as assumed in Gruber et al. (2014). The required ACC noise level is similar to the accuracy reached with the GOCE accelerometers, and one order of magnitude smaller than the ACC requirement in Gruber et al. (2014). For ORB2 and ORB3 (363 km and 420 km polar altitude respectively) the required ACC noise levels are similar as for ORB1. But the SST requirements are significantly more stringent,  $2 \text{ nm}/\sqrt{\text{Hz}}$  for ORB3 instead of  $20 \text{ nm}/\sqrt{\text{Hz}}$  for ORB1. With current technical limits for laser ranging and accelerometers it seems not to be realistic to reach MO2 at an altitude of ORB4 (487 km polar altitude). Therefore this scenario is not considered further in this thesis.

Figure 4.6 shows cumulative geoid errors up to  $l_{\text{max}} = 401$  for the single polar and double Bender-type pair of ORB1 with the required total noise (cf. Tab. 4.3 and Fig. 4.5) in comparison with the three geoid accuracy requirements of MO2, i.e. 0.01 mm at  $l = 40$ , 0.4 mm at  $l = 134$  and 30 mm at  $l = 401$ . It can

Table 4.3: Required noise levels for the basic noise ASDs (Eq. (2.46) and (2.47)) in order to reach MO2 with the four basic single polar in-line pairs.

	SST in $\text{m}/\sqrt{\text{Hz}}$	ACC in $\text{m}/\text{s}^2/\sqrt{\text{Hz}}$
ORB1p	$2.0 \cdot 10^{-8}$	$2.2 \cdot 10^{-12}$
ORB2p	$6.2 \cdot 10^{-9}$	$1.8 \cdot 10^{-12}$
ORB3p	$2.1 \cdot 10^{-9}$	$1.5 \cdot 10^{-12}$
ORB4p	$6.3 \cdot 10^{-10}$	$4.4 \cdot 10^{-13}$

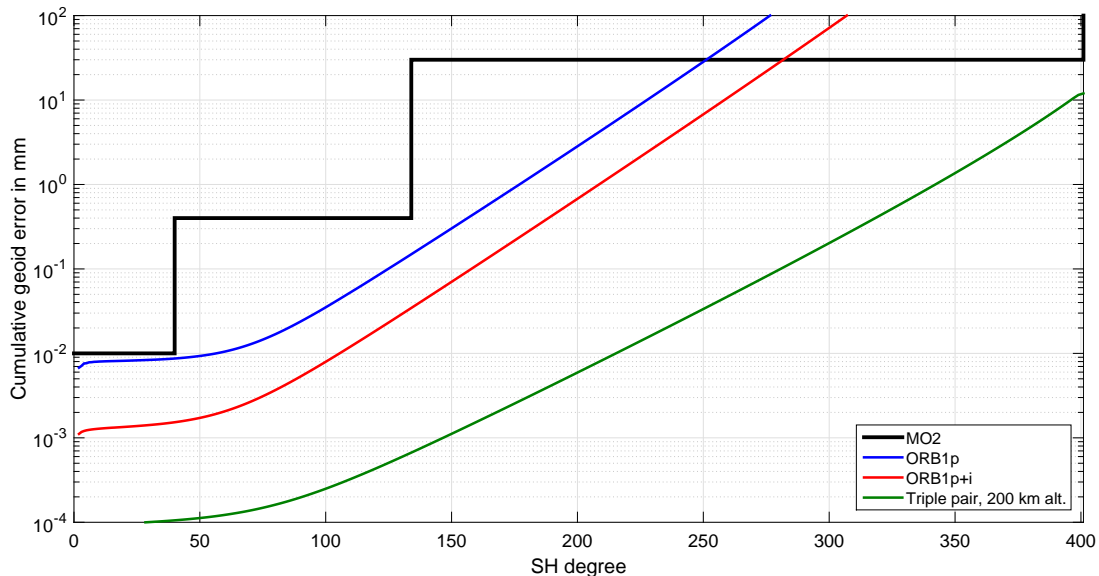


Figure 4.6: Cumulative geoid errors in mm of the single polar and double Bender-type pair of ORB1 with required total noise (cf. Tab. 4.3 and Fig. 4.5) in comparison with MO2 and of a possible triple pair scenario fulfilling the 50 km spatial resolution requirement of MO2.

be seen that even the double Bender-type pair of ORB1 cannot fulfil the high resolution requirement ( $l = 401$  corresponding to 50 km spatial resolution). The single pair reaches 30 mm approximately at 80 km ( $l = 252$ ) and the double pair at 70 km ( $l = 282$ ) resolution. To reach the 50 km requirement with ORB1 the total noise would have to be decreased by more than 2 (3) orders of magnitude for the double Bender-type (single polar) pair.

A possible scenario which could reach the 50 km requirement is a triple pair (polar,  $80^\circ$  and  $70^\circ$  inclined) on 200 km altitude with an instrument accuracy 10 times better than the ORB1 requirements, i.e.  $2.0 \cdot 10^{-9}$  m/ $\sqrt{\text{Hz}}$  for SST and  $2.2 \cdot 10^{-13}$  m/s<sup>2</sup>/ $\sqrt{\text{Hz}}$  for ACC. But, as discussed before, such instrument requirements are not realistic to be reached for the NGGM, possibly for the generation thereafter. Therefore the 50 km requirement is not further discussed in this thesis. But the science requirements show that definitely there is a need for 50 km spatial resolution.

At this point it has to be emphasized that the gravity field retrieval performance in this chapter is addressed only with the formal errors of a rigorous solution. These errors represent the true errors of the scenarios observing a static gravity field. With temporal variations deterministic errors are introduced and the retrieval performance cannot only be assessed with formal errors. Temporal aliasing as the major deterministic error contribution is discussed in Chap. 6 and 7. But it is reasonable not to include temporal aliasing effects in the instrument requirements estimation. This is because the Earth's time varying gravity field which leads to temporal aliasing contains many signals which the NGGM should observe, e.g. mass variations in the global water cycle.



## 5 Other Error Contributions

In this chapter other error contributions are discussed which are neither taken into account in the derivation of the instrument requirements in the last chapter nor in the gravity field retrieval performance simulations in the following chapters. Therefore requirements have to be determined in order to assure the results to be realistic. On the one hand these error contributions belong to other sensors on the satellites, i.e. star sensors and GNSS receivers. On the other hand error contributions of environmental variations and couplings of such variations with the key sensors are analysed.

### 5.1 Star Sensors

The NGGM requires a good knowledge of the inertial attitude of all satellites for which star sensor (usually 2 or 3 on each satellite) observations are used. In addition, on a low-low SST pair with a laser ranging instrument attitude information can also be retrieved from specific laser interferometer data, the so-called differential wave front sensing (Gruber et al., 2014). But in this section only the star sensor error contribution to the attitude determination is discussed and star sensor requirements are derived from error propagation.

For a low-low SST pair with laser ranging instrument there are already high attitude requirements ( $10^{-4}$  rad in Gruber et al. (2014)) in order to assure laser link acquisition. But there is also a direct connection from attitude angles to the gravitational observations via the accelerometer (ACC). Optimally the ACC is placed in the center of mass of the satellite and measures the non-gravitational forces acting on the satellite. The projection of this observed acceleration vector onto the LoS between the two satellites has to be subtracted from the total acceleration differences (derived from the SST observations), i.e.

$$\langle \Delta \mathbf{a}_{\text{grav.}}, \Delta \mathbf{r}_0 \rangle = \langle \Delta \mathbf{a}_{\text{SST}}, \Delta \mathbf{r}_0 \rangle - \langle \Delta \mathbf{a}_{\text{ACC}}, \Delta \mathbf{r}_0 \rangle. \quad (5.1)$$

Neglecting misalignment and scale factor errors of the three ACC axes, in the following the star sensor errors in terms of attitude angle errors are propagated onto the LoS acceleration differences. Figure 5.1 shows a sketch of a low-low SST pair in space-fixed frame with local LoS fixed frame and ACC reference frames. The non-gravitational accelerations are measured in the ACC reference frame and have to be rotated into the LoS reference frame with rotation angles  $\alpha_{1/2}$ ,  $\beta_{1/2}$ ,  $\gamma_{1/2}$ . These angles belong to rotations around the LoS-axes along-track or roll axis ( $\mathbf{x}_{\text{LoS}}$ ), cross-track or pitch axis ( $\mathbf{y}_{\text{LoS}}$ ), and radial or yaw axis ( $\mathbf{z}_{\text{LoS}}$ ), respectively. Assuming that the non-gravitational accelerations are dominated by atmospheric drag, and therefore are anti-parallel to the velocity vector, the projection of the non-gravitational accelerations is

$$\langle \Delta \mathbf{a}_{\text{ACC}}, \Delta \mathbf{r}_0 \rangle = \langle -|\mathbf{a}_{1,\text{ACC}}| \cdot R(\alpha_1, \beta_1, \gamma_1) \cdot \mathbf{v}_{1,0} + |\mathbf{a}_{2,\text{ACC}}| \cdot R(\alpha_2, \beta_2, \gamma_2) \cdot \mathbf{v}_{2,0}, \Delta \mathbf{r}_0 \rangle \quad (5.2)$$

with the rotation matrices  $R$  from ACC to LoS reference frame and with the normalized velocity vectors  $\mathbf{v}_{1/2,0}$ . The components of the normalized velocity vector in the LoS-frame are  $\mathbf{v}_0 = (\mathbf{v}_{x,0} \ \mathbf{v}_{y,0} \ \mathbf{v}_{z,0})^T$ .

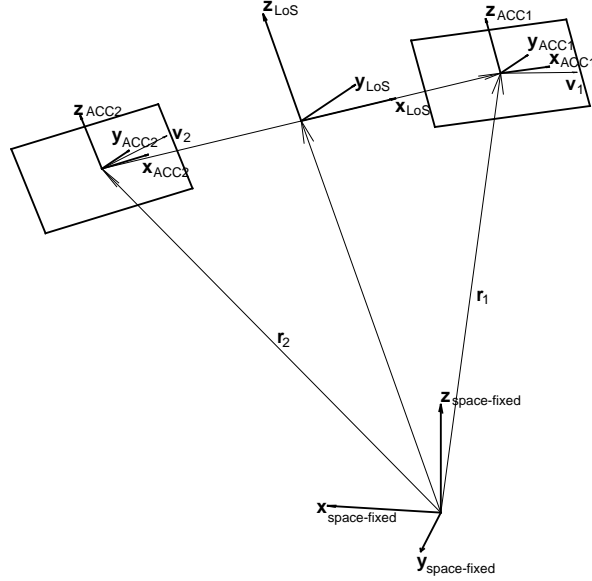


Figure 5.1: low-low SST pair in space-fixed frame, local LoS fixed frame and accelerometer reference frames ( $ACC_1, 2$ ).

The error propagation is done for each of the two satellites separately. For the variance of the non-gravitational accelerations projected on the LoS  $\sigma_{ACC-LoS}^2$  it is (leaving out indices 1 and 2 for the two satellites)

$$\begin{aligned} \frac{\sigma_{ACC-LoS}^2}{|\mathbf{a}_{ACC}|^2} &= \left\langle \frac{\partial R}{\partial \alpha} \cdot \mathbf{v}_0, \Delta \mathbf{r}_0 \right\rangle^2 \sigma_\alpha^2 + \left\langle \frac{\partial R}{\partial \beta} \cdot \mathbf{v}_0, \Delta \mathbf{r}_0 \right\rangle^2 \sigma_\beta^2 + \left\langle \frac{\partial R}{\partial \gamma} \cdot \mathbf{v}_0, \Delta \mathbf{r}_0 \right\rangle^2 \sigma_\gamma^2 \\ &= \cos^2(\angle(\mathbf{v}_0, \Delta \mathbf{r}_0)) \left( \left| \frac{\partial R}{\partial \alpha} \mathbf{v}_0 \right|^2 \cdot \sigma_\alpha^2 + \left| \frac{\partial R}{\partial \beta} \mathbf{v}_0 \right|^2 \cdot \sigma_\beta^2 + \left| \frac{\partial R}{\partial \gamma} \mathbf{v}_0 \right|^2 \cdot \sigma_\gamma^2 \right) \end{aligned} \quad (5.3)$$

with the angle between the velocity vector and the LoS  $\angle(\mathbf{v}_0, \Delta \mathbf{r}_0)$ .

The rotation matrix describes a rotation around all three axes with  $R = R_z(\gamma) \cdot R_y(\beta) \cdot R_x(\alpha)$ . Therefore the derivative of  $R$  wrt.  $\alpha$  contains zero in the first column and the derivative wrt.  $\gamma$  contains zero in the last row. Assuming a successfully acquired laser link, the rotation angles are small. Applying approximations for small angles the wanted variance in Eq. (5.3) is

$$\begin{aligned} \left( \frac{\sigma_{ACC-LoS}}{|\mathbf{a}_{ACC}| \cos(\angle(\mathbf{v}_0, \Delta \mathbf{r}_0))} \right)^2 &\approx (\mathbf{v}_{y,0}^2 + \mathbf{v}_{z,0}^2) \cdot \sigma_\alpha^2 + \\ &(\mathbf{v}_{x,0}^2 - 2\alpha \mathbf{v}_{y,0} \mathbf{v}_{z,0} + \mathbf{v}_{z,0}^2) \cdot \sigma_\beta^2 + \\ &(\mathbf{v}_{x,0}^2 + 2\alpha \mathbf{v}_{y,0} \mathbf{v}_{z,0} - 2\beta \mathbf{v}_{x,0} \mathbf{v}_{z,0} + \mathbf{v}_{y,0}^2) \cdot \sigma_\gamma^2. \end{aligned} \quad (5.4)$$

As for an in-line formation the velocity vector is nearly parallel to the LoS it can be approximated by

$$\sigma_{ACC-LoS} \approx \sqrt{2} |\mathbf{a}_{ACC}| \sigma_\beta \quad (5.5)$$

assuming  $\sigma_\beta = \sigma_\gamma$ . And because Eq. (5.5) is applied to both satellites the error propagation for both satellites is the right side of Eq. (5.5) times  $\sqrt{2}$  (assuming equal attitude angle variances on both satellites).

Table 5.1: Atmospheric densities for low and high short term activity (from CIRA-2012) and absolute drag accelerations for the altitudes of the three lower polar reference orbits (Tab. 4.1).

altitude in km	density in kg/m <sup>3</sup>		abs. drag acc. in m/s <sup>2</sup>	
	low activity	high activity	low activity	high activity
300	$5.9 \cdot 10^{-12}$	$6.2 \cdot 10^{-11}$	$1.6 \cdot 10^{-6}$	$1.7 \cdot 10^{-5}$
360	$1.2 \cdot 10^{-12}$	$2.6 \cdot 10^{-11}$	$3.3 \cdot 10^{-7}$	$7.1 \cdot 10^{-6}$
420	$2.9 \cdot 10^{-13}$	$1.2 \cdot 10^{-11}$	$7.8 \cdot 10^{-8}$	$3.2 \cdot 10^{-6}$

The error propagation depends on the absolute non-gravitational acceleration, which is dominated by atmospheric drag. The absolute drag acceleration is (Montenbruck and Gill, 2005)

$$|\mathbf{a}| = \frac{1}{2} C_D \frac{A}{m} \rho |\mathbf{v}|^2. \quad (5.6)$$

The following reference values for LEOs are used for the drag coefficient  $C_D = 2.3$ , the satellite's cross-sectional area  $A = 2 \text{ m}^2$  and the satellite mass  $m = 500 \text{ kg}$  (Montenbruck and Gill, 2005). The COSPAR (Committee on Space Research) International Reference Atmosphere (CIRA) 2012 is the fifth in the series (Rees, 1988; Rees et al., 1990) and provides total atmospheric density values  $\rho$  for low and high solar activities. With these values the absolute non-gravitational accelerations are approximated and given in Tab. 5.1.

The propagated attitude angle errors (Eq. (5.5)) of both satellites must not exceed the total ACC noise requirements in Tab. 4.3. For low solar activity this is ensured if the pitch and yaw angle standard deviation ( $\sigma_\beta = \sigma_\gamma$ ) is smaller than  $7 \cdot 10^{-7}$  rad for 300 km altitude ( $3 \cdot 10^{-6}$  and  $10^{-5}$  rad for 360 and 420 km, respectively). For high activity the requirements are  $6 \cdot 10^{-8}$ ,  $10^{-7}$  and  $2 \cdot 10^{-7}$  rad, respectively. Current accuracies of attitude angle determination from star sensors on LEOs are in the order of  $10^{-5}$  rad for GOCE (Stummer, 2013), Anselmi (2010) assumes accuracies of  $10^{-6}$  rad. The mission duration of the NGGM covers one full solar cycle. Therefore the attitude angle requirements must hold also for high solar activity. And because the attitude angle requirements for high activity are smaller than current technical star sensor limits the drag has to be compensated, e.g. with cold gas (Gruber et al., 2014) or ion thrusters (Drinkwater et al., 2003). To get attitude angle requirements in the order of  $10^{-6}$  rad the drag accelerations have to be reduced by at least a factor of 30 for 300 km altitude and by a factor of 10 for 420 km altitude (safety factor of 2 applied).

Drag compensation may be required because of another reason as well, i.e. the saturation limit of the ACCs. The maximum acceleration limits the sensitivity of the instrument. In Gruber et al. (2014) a drag compensation requirement of 200 times the ACC requirement is determined. For the NGGM in this thesis this would lead to a drag compensation requirement of approximately  $4 \cdot 10^{-10} \text{ m/s}^2$  within the measurement bandwidth for the three lower polar orbits. If no higher non-gravitational accelerations are observed by the ACC the attitude angle requirements are in the order of 2 mrad and feasible with current star sensors.

For SGG the situation is different, as a misorientation of the gradiometer directly affects the observed SGG components. In Pail (2005) the effects of different misalignments are analysed with respect to gravity field retrieval performance for GOCE. The main conclusion is, that the results are mostly affected by random misalignment errors as assumed above for low-low SST. For random errors of the three rotation angles in the order of  $10^{-5}$  rad the misalignment errors are the major error component in a GOCE-like SGG gravity field retrieval. In the case of the NGGM an approximately 1,000 times higher sensitivity of radial SGG is required to contribute significantly to a combined solution with low-low SST. Therefore, random misalignment errors in the order of  $10^{-6}$  rad (as assumed above) would dominate the  $V_{rr}$  solution and no contribution to a combined solution is expected.

The accuracies and requirements in this section are formulated independently of the frequency. In reality the attitude angle noise is not white, but it depends on the frequency. Furthermore, the requirements for the ACCs are formulated depending on the frequency as well (Fig. 4.5). Therefore the attitude angle requirements have to be applied to the measurement bandwidth of the ACC, i.e.  $1 < f < 100$  mHz. For  $f < 1$  mHz the attitude angle requirements can be considered more relaxed analogously to the ACC ASD with a  $1/f^2$  behavior.

## 5.2 GNSS Positioning

In this thesis the positions derived from Global Navigation Satellite System (GNSS) observations are not used as gravity field observations. Satellite positions on purely circular orbits are used in least squares adjustment as given error free values. Of course, in reality, precise GNSS observations of the positions of a satellite in orbit contain gravity field information because the movement of the satellite depends on gravity. This observation type uses orbit perturbations in along-track, cross-track and radial direction and is called high-low SST. The accuracy of LEO high-low SST derived from GNSS is in the order of a few centimeters (usually radial component worse than the horizontal components). For example for GOCE it amounts to a level of 2 cm (Bock et al., 2011). With these observations collected during the whole GOCE mission phase (in total approximately 3.5 years) a global gravity field (except for the polar gaps) is estimated up to  $l_{\max} = 150$  (Brockmann et al., 2014).

But the sensitivity of this observation type is not sufficient to contribute significantly to a combined gravity field solution with low-low SST laser ranging observations. Figure 5.2 shows SANA results in terms of SH degree RMS of the formal errors of high-low SST in comparison with low-low SST for ORB1 (single polar and double Bender-type pair). The high-low SST sensitivity is assessed by the combination of 3D orbit perturbation observations ( $\Delta x, \Delta y, \Delta z$ ) according to Eq. 2.37 with cm accuracy. The low-low SST formal errors assume the required noise levels for SST and ACC in Tab. 4.3. Only for the very low SH degrees high-low SST contributes to the combined solution for the single polar pair (left). For the double Bender-type pair (right) there is no significant contribution of high-low SST to the combined solution.

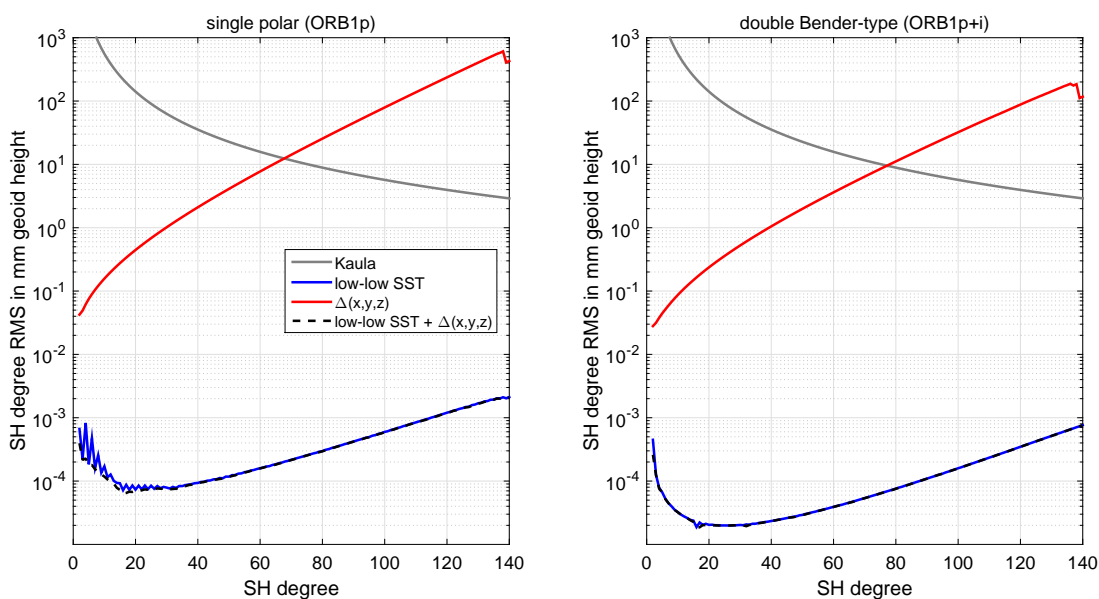


Figure 5.2: SANA simulation results in terms of SH degree RMS in mm geoid height for the single polar pair (ORB1p, left) and the double Bender-type pair (ORB1p+i, right) in comparison with static Kaula-rule. The formal errors of high-low SST (3D orbit perturbations, red), low-low SST (required SST and ACC noise from Fig. 4.5 and Tab. 4.3, blue) and the combined solution (black), respectively, are shown.

Nevertheless GNSS positioning is required for the NGGM. The NGGM studies in Elsaka (2012) and Wiese et al. (2012) use white noise assumptions for the positions of 1 and 2 cm, respectively. And, as expected, the final gravity retrieval performance simulations in these studies are not dominated by the positioning errors. Therefore it is reasonable to require GNSS positioning accuracies for the NGGM of 1 cm for the horizontal and 2 cm for the radial component.

### 5.3 Tone Errors

Tone errors are harmonic errors mainly due to temperature variations within the satellites (Gruber et al., 2014). They affect both laser ranging and accelerometer observations and contain multiples of the orbital frequency  $n \cdot f_0$ . Such signals contain periods measured in cycles per revolution (cpr). In Gruber et al. (2014) the first 6 tone errors ( $1 \leq n \leq 6$ ) with 1 to 6 cpr are addressed. This error contribution is analysed for the basic single polar pairs (Tab. 4.1). As this is a deterministic error the SANA is not able to assess it adequately, and therefore LCLA simulations are used.

Tone errors  $\tau_n$  are expressed depending on time  $t$  or argument of latitude  $u$  with

$$\begin{aligned}\tau_n(t) &= \xi_n \sin(n2\pi f_0 t + \varphi_n) \\ \tau_n(u) &= \xi_n \sin(nu + \varphi_n)\end{aligned}\tag{5.7}$$

with amplitude  $\xi_n$  and phase  $\varphi_n$ .

Figure 5.3 (top) shows normalized tone errors ( $\xi = 1$ ) for  $1 \leq n \leq 3$  (1, 2 and 3 cpr) depending on the argument of latitude  $u$  and on the phase  $\varphi$ . The mean contribution of tone errors to a global gravity field can be derived by averaging the tone errors for each co-latitude  $\theta$ . For polar orbits the co-latitude can be expressed with the argument of latitude by  $\theta = \pi - |\pi - |u - \pi/2||$ . Therefore the two tone error values for each  $\theta$  (ascending and descending) are averaged resulting in the bottom plots in Fig. 5.3. It can be seen that tone errors for odd  $n$  are averaged to zero for  $\varphi = 90^\circ$  and  $\varphi = 270^\circ$ . For even  $n$  this is the case for  $\varphi = 0^\circ$  and  $\varphi = 180^\circ$ . Hence, the largest tone error effects are expected for odd  $n$  for sine terms ( $\varphi = 0^\circ$  and  $\varphi = 180^\circ$ ) and for even  $n$  for cosine terms ( $\varphi = 90^\circ$  and  $\varphi = 270^\circ$ ). And

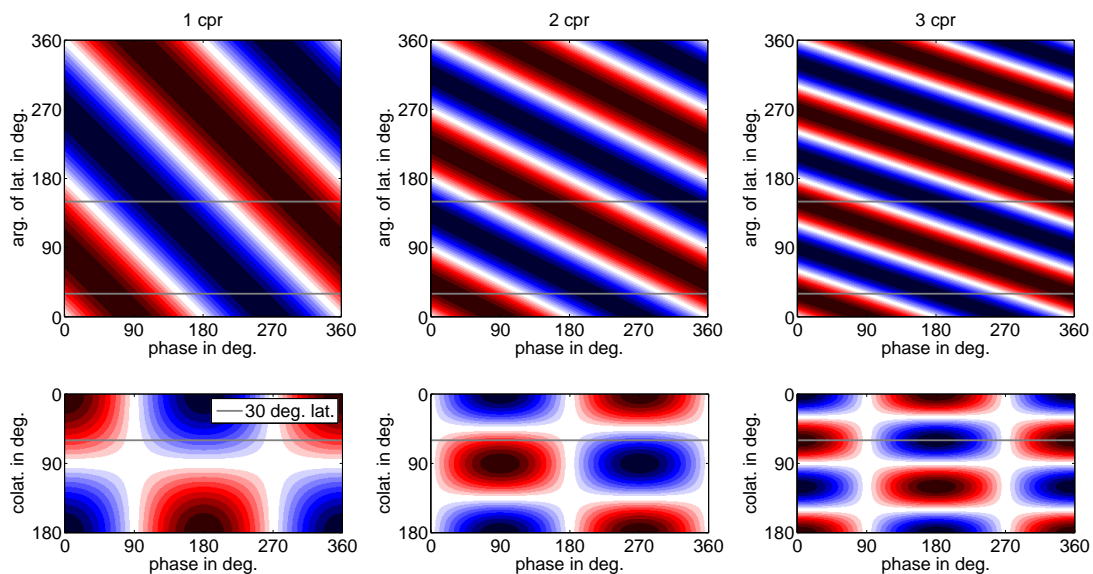


Figure 5.3: Normalized tone errors for 1 to 3 cpr depending on the argument of latitude  $u$  (top) and on the co-latitude  $\theta$  (bottom). The gray lines represent locations of the same spherical latitude  $30^\circ$  for polar orbits.

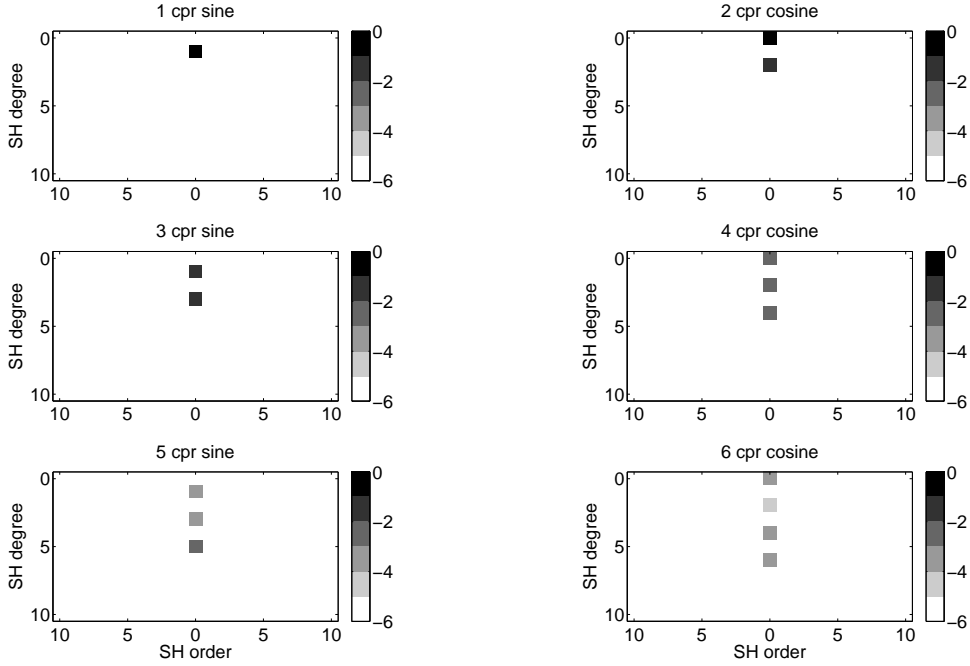


Figure 5.4: Maximum tone error geoid contribution for ORB1p in  $\log_{10}$  (mm) in the SH domain for 1 to 6 cpr.

from Fig. 5.3 (bottom) for polar orbits it can be concluded that tone errors  $\tau_n$  only affect the zonal coefficients  $\tilde{C}_{l0}$  with  $l \leq n$  (Gruber et al., 2014).

Requirements are derived for the amplitudes of the tone errors for  $1 \leq n \leq 6$  based on LCLA simulations for the basic single polar pairs. Thereby the amplitudes for different  $n$  are not assumed to be independent. In Gruber et al. (2014) it is described how the amplitudes decrease with increasing  $n$ . The reference amplitudes in terms of ranges are  $20 \cdot 5^{1-n} \mu\text{m}$  and

$$\xi_n = (n2\pi f_0)^2 \cdot 2 \cdot 10^{-5} \cdot 5^{1-n} \text{ m/s}^2 \quad (5.8)$$

in terms of range accelerations. This leads to the reference amplitudes given in Tab. 5.2 for the first 6 tone errors.

The effects of tone errors on global gravity retrievals is simulated with the LCLA applying tone errors with the reference amplitudes in Tab. 5.2 in terms of range accelerations. As the maximum effects shall be analysed, for odd  $n$  sine terms and for even  $n$  cosine terms are used. The results of the LCLA are shown in Fig. 5.4 in terms of  $\log_{10}$  scaled absolute SH coefficients in mm geoid height. As expected from Fig. 5.3 (bottom) it can be seen that tone errors  $\tau_n$  affect only zonal coefficients with  $l \leq n$ . Furthermore, odd tone errors affect only odd zonals and even tone errors affect only even zonals. As the amplitudes decrease with increasing  $n$  the SH coefficients affected by tone errors show a decrease as well.

Table 5.3 gives the geoid contributions of the tone errors with reference amplitudes for the single polar in-line pairs (cf. Tab. 4.1). The total geoid error contribution ( $l \geq 0$ ) is 0.26 mm for 1 cpr down to

Table 5.2: Tone error amplitudes for 1 to 6 cpr in terms of ranges and range accelerations.

	1 cpr	2 cpr	3 cpr	4 cpr	5 cpr	6 cpr
range amplitudes in $\mu\text{m}$	20	4.0	0.80	0.16	0.032	0.0064
range acc. amp. in $10^{-12} \text{ m/s}^2$	26	21	9.4	3.3	1.0	0.30

0.4  $\mu\text{m}$  for 6 cpr and 0.47 mm for the sum of all 6 tone errors. As with the NGGM no degree 0 and 1 coefficients are estimated, the contribution is also given for  $l \geq 2$ . Here, the total geoid error contribution of the tone errors is 0.13 mm.

This contribution has to be compared with the strongest geoid requirement of MO2, i.e. 0.01 mm for  $l = 40$ . Hence, in order to derive tone error amplitude requirements for the NGGM, the reference amplitudes in Tab. 5.2 have to be divided by 13 (130 for a safety factor of 10). As the amplitude requirements belong to the total tone errors on the LoS acceleration differences the requirements are distributed equally to the two main instruments (SST and ACC). This leads to a requirement for 1 cpr of 0.8  $\mu\text{m}$  for the laser ranging instrument and of  $4 \cdot 10^{-14}$  m/s<sup>2</sup> for the accelerometer.

On the one hand these requirements are very critical to be fulfilled from a technological point of view, especially for the accelerometers (Gruber et al., 2014). On the other hand the total tone error amplitudes on the LoS observations depend on the phase differences  $\Delta\varphi$  of the tone errors on each satellite. The total tone error on the LoS observations  $\tau_{\text{LoS}}$  is the difference between the tone errors on satellite 1 and 2, i.e.  $\tau_{1,n} - \tau_{2,n}$ . Hence, the total amplitude is

$$\xi_{\text{LoS},n} = \sqrt{\xi_{1,n}^2 + \xi_{2,n}^2 - 2\xi_{1,n}\xi_{2,n}\cos(\Delta\varphi)}. \quad (5.9)$$

For equal tone error amplitudes on both satellites  $\xi_n = \xi_{1,n} = \xi_{2,n}$  and  $\Delta\varphi$  closer than  $60^\circ$  to a multiple of  $360^\circ$  the total tone error amplitude  $\xi_{\text{LoS},n}$  is smaller than  $\xi_n$ . It is smaller than 10% of  $\xi_n$  if  $\Delta\varphi$  is closer than  $6^\circ$  to a multiple of  $360^\circ$ . As the inter-satellite distance of the NGGM is only 100 km the environmental variations on the two satellites are expected to be similar. Therefore the tone error amplitude on the LoS observation might be smaller than the amplitudes on each satellite.

Of course the tone errors can also be included in the functional model. But as the analysis in this section shows there are high correlations with the low SH degree zonal coefficients. Hence, tone error amplitude requirements are postulated for the NGGM in order to prevent larger errors in low SH degrees.

Table 5.3: Maximum tone error geoid contribution in mm for the basic single polar scenarios.

	1 cpr	2 cpr	3 cpr	4 cpr	5 cpr	6 cpr	total
$l \geq 0$	0.26	0.17	0.033	0.0082	0.0016	0.00037	0.47
$l \geq 2$	0	0.097	0.025	0.007	0.0015	0.00034	0.13



## 6 Temporal Aliasing

In this chapter temporal aliasing is discussed which is the major deterministic error contribution for the NGGM. For all the simulations in the previous chapters a static gravity field has been assumed. And only stochastic error contributions have been analysed. Obviously this is a major simplification, because the Earth's gravity field is continuous in space and time and has an infinite spectrum wrt. spatial and temporal resolution. The sampling of the gravity field can only be realized with finite spatial and temporal resolution. Therefore, both spatial and temporal aliasing cannot be avoided. Spatial aliasing is not further discussed in this thesis. In the simulations spatial aliasing is excluded by limiting the input gravity field models to the same  $l_{\max}$  as the adjusted set of SH coefficients.

In this chapter temporal aliasing is elaborated based on two numerical sampling examples. Furthermore the characteristics of the geophysical sources which are responsible for the largest temporal aliasing effects are analysed and different strategies are discussed which are able to reduce the effects of temporal aliasing.

At first the issue of temporal aliasing is visualized in the case of the discrete sampling of a 1D time series in Fig. 6.1. A continuous periodic signal  $x$  with period  $P_x = 10$  s (frequency  $f_x = 1/P_x = 0.1$  Hz) is sampled with discrete sampling intervals  $\Delta t_1 = 3$  s and  $\Delta t_2 = 8$  s. If the Nyquist frequency  $f_N = 1/(2\Delta t)$  is smaller than  $f_x$  there is temporal aliasing and  $x$  cannot be reconstructed with its sampled representation. Furthermore, the discrete Fourier transform of the under-sampled representation shows aliased amplitudes at an aliasing frequency  $f_{\text{alias}} = |\text{mod}(f_x + f_N, 2f_N) - f_N|$ . Figure 6.1 shows an example with and without temporal aliasing. With  $\Delta t_1 = 3$  s  $< P_x/2$  the signal  $x$  can be reconstructed. But in the case of temporal aliasing ( $\Delta t_2 = 8$  s  $> P_x/2$ ) the spectrum is distorted with the alias frequency  $f_{\text{alias}} = 25$  mHz ( $P_{\text{alias}} = 40$  s).

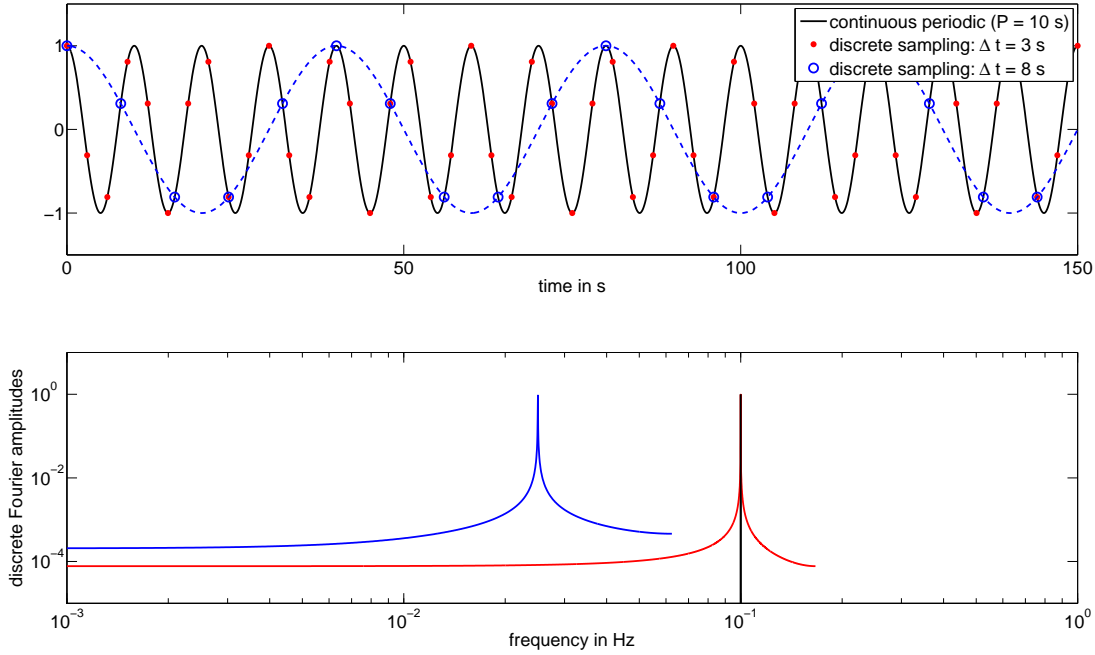


Figure 6.1: Temporal aliasing in the case of 1D time series sampling. Top: normalized continuous cosine time series with 10 s period (black) sampled with 3 s (red) and 8 s (blue) respectively. Bottom: discrete Fourier amplitudes of the three time series in the top.

## 6.1 Optimal Sampling regarding Temporal Aliasing

The next step towards a better understanding of temporal aliasing for the NGGM is a numerical simulation of the spatio-temporal sampling with single and double repeat orbits. The main characteristics of this sampling are described by the spatio-temporal function of the orbital crossings of a constant latitude. For circular orbits the longitudes of these crossings do not change with latitude. Only the time interval between two consecutive ascending and descending crossings varies. In the following temporal aliasing is analysed for direct observations of discrete time varying signals at the equator crossings for single and double pair repeat orbits.

The functional model of the time varying signal at the equator  $x(\lambda, t)$  is given in Eq. (6.1) with a combination of three Fourier series expansions in order  $m$ . One expansion describes the static signal with coefficients  $(c_m, s_m)$ . The other two describe a signal with discrete frequency  $f = 1/T$  (period  $T$ ). It contains sine and cosine amplitudes depending on the longitude  $a(\lambda)$  and  $b(\lambda)$  which are series expansions with coefficients  $(a_m^c, a_m^s)$  and  $(b_m^c, b_m^s)$ , respectively.

$$\begin{aligned}
 x(\lambda, t) &= \sum_{m=1}^{m_{\max}} (c_m \cos m\lambda + s_m \sin m\lambda) + a(\lambda) \cos\left(\frac{2\pi}{T}t\right) + b(\lambda) \sin\left(\frac{2\pi}{T}t\right) \\
 a(\lambda) &= \sum_{m=1}^{m_{\max}} (a_m^c \cos m\lambda + a_m^s \sin m\lambda) \\
 b(\lambda) &= \sum_{m=1}^{m_{\max}} (b_m^c \cos m\lambda + b_m^s \sin m\lambda).
 \end{aligned} \tag{6.1}$$

A spectral representation of the amplitudes for the static and time varying contents of Eq. (6.1) is given

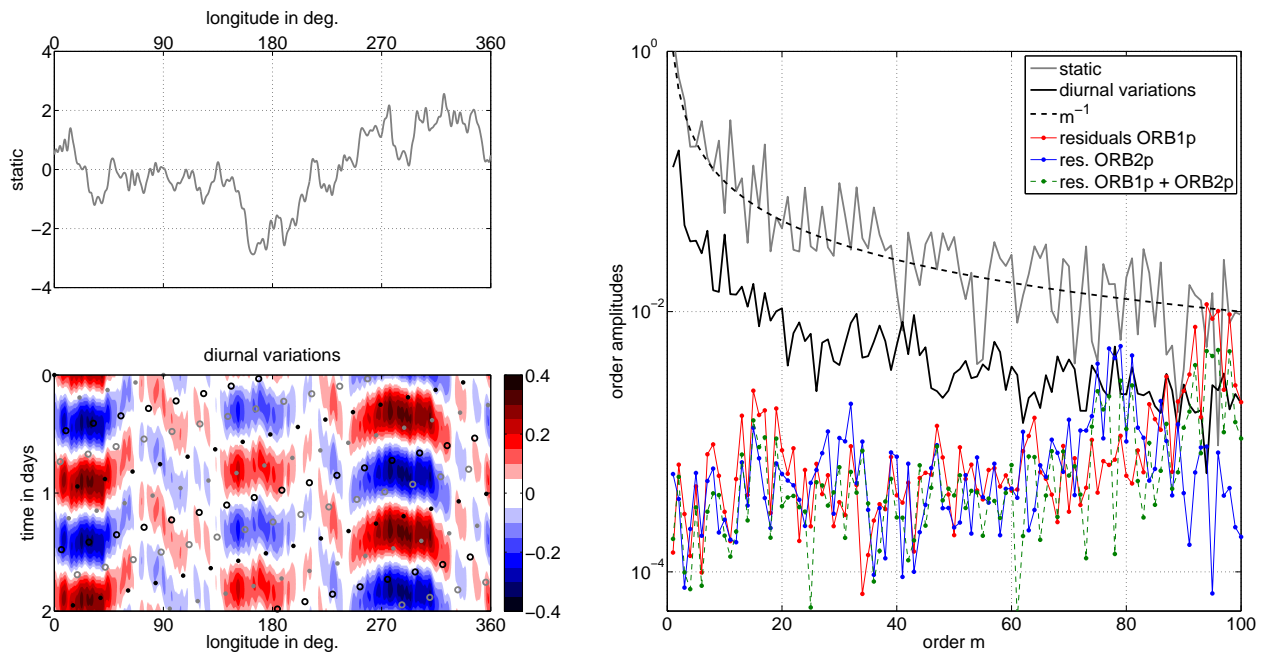


Figure 6.2: Synthetic harmonic signal (maximum order  $m_{\max} = 100$ ) at the equator with discrete time variations superimposed (1 day period) in the spatio-temporal domain (left) and the spectral domain (right, cf. Eq. (6.2)). The diurnal variations (bottom left) are shown with the ascending (dots) and descending (circles) equator crossing samples of the two orbits ORB1p (black) and ORB2p (gray) with an ascending node separation of  $90^\circ$ . The order amplitudes of the residuals of the least squares estimates wrt. the static signal are shown for the single pairs ORB1p and ORB2p and the combined solution ORB1p + ORB2p (right).

by the order amplitudes

$$\begin{aligned} \kappa_{\text{static}}(m) &= \sqrt{c_m^2 + s_m^2} \\ \kappa_{\text{temp.var.}}(m) &= \sqrt{(a_m^c)^2 + (a_m^s)^2 + (b_m^c)^2 + (b_m^s)^2}. \end{aligned} \quad (6.2)$$

For geophysical signals on the Earth a characteristic order amplitude behaviour of  $m^{-1}$  is assumed. Figure 6.2 gives a graphical representation of such a characteristic unit-less signal according to Eq. (6.1) in the spatio-temporal and the spectral domain (maximum order  $m_{\max} = 100$ , period  $T = 1$  day). The random coefficients for the static signal are scaled with  $m^{-1}$ . For the time varying signal the coefficients are scaled with  $m^{-1}/10$ . The static signal is shown as function of longitude (top left), and the diurnal signal is shown as function of longitude and time for two days (bottom left). The order amplitudes (right) show the static signal in gray, the diurnal signal in black.

For the initial longitude  $\lambda_0$  the spatio-temporal sampling with a repeat orbit depends on  $N_{\text{day}}$  and  $N_{\text{rev}}$ . The longitude of the ascending equator crossings at epochs  $t = k \cdot t_{\text{rev}}$  is  $\lambda_0 + (k - 1) \Delta\lambda$  with integer  $0 \leq k \leq N_{\text{rev}}$  (cf. Eq. (2.29)). For descending equator crossings  $\lambda_0 + \pi + (2k + 1) \Delta\lambda/2$  holds for  $t = (2k + 1) t_{\text{rev}}/2$ .

Figure 6.1 (bottom left) shows the equator crossings of the two single repeat orbits ORB1p and ORB2p (cf. Tab. 4.1) in black and gray dots (ascending) and circles (descending), respectively. ORB1p starts at  $\lambda_0 = 0^\circ$  and ORB2p at  $\lambda_0 = 90^\circ$ . With this analysis of equator crossings the benefit of an inclined pair can not be assessed. The only different parameter between a polar and an inclined pair with the same  $N_{\text{day}}$  and  $N_{\text{rev}}$  which is relevant for this analysis is the revolution time (approximately 40 s difference between  $I = 89^\circ$  and  $I = 70^\circ$ ). Therefore only polar pairs and combinations of polar pairs are analysed here.

The effects of temporal aliasing are analysed on the basis of least-squares estimates of static coefficients for the basic single and double pairs ORB1p, ORB2p and ORB3p (cf. Tab. 4.1). For each orbit the

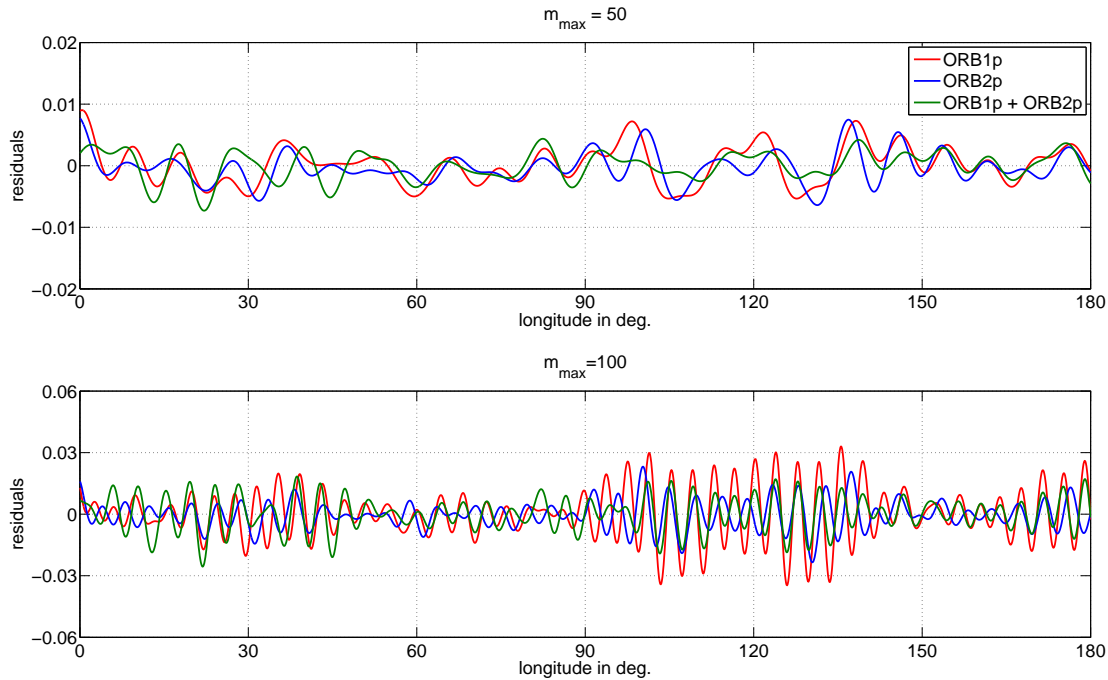


Figure 6.3: Spatial residuals wrt. the static signal ( $0^\circ \leq \lambda \leq 180^\circ$ ) for ORB1p, ORB2p and the combination of both for  $m_{\max} = 50$  (top) and  $m_{\max} = 100$  (bottom).

observations contain the total signal in Eq. (6.1) evaluated at the equator crossings. No stochastic noise is applied, the weighting matrix is the unit matrix and the unknowns are  $(\hat{c}_m, \hat{s}_m)$ .

The differences between the static reference and the estimated coefficients of this LSA are dominated by temporal aliasing effects of the diurnal signal. Figure 6.2 (right) shows the residuals in terms of order amplitudes  $\kappa_{\text{static}}$  (Eq. (6.2)) for the single orbits ORB1p and ORB2p and the combined solution of ORB1p and ORB2p. All three residual amplitudes show smaller values than the mean diurnal signal amplitudes (black) for  $m < 70$ . Around specific orders the residuals show increased amplitudes. These orders are integer multiples of  $N_{\text{rev}}/N_{\text{day}}$  and the magnitude of these effects differs for the different solutions.

The effects are referred to as order resonances (later SH order resonances, cf. Chap. 7). ORB1p shows a stronger order resonance at  $m = 94$  than ORB2p which shows stronger resonance at  $m = 78$ . The combined solution does not benefit much from the different behaviour of the two single orbits. For pure stochastic error effects the combined solution would show smaller residuals for all  $m$  than each single solution. But as temporal aliasing is non-stochastic the larger residuals of ORB1p around the resonance order  $m = 94$  and of ORB2p around  $m = 78$  partly remain in the combined solution as well.

In the spatial domain the residuals are shown in Fig. 6.3 for the same three solutions as in Fig. 6.2. The temporal aliasing effects occur as oscillations around zero. The residuals for  $m_{\max} = 50$  (top) of course contain less spectral content as for  $m_{\max} = 100$  (bottom). From the order amplitudes in Fig. 6.2 (right) it is expected that the residuals up to  $m_{\max} = 100$  are dominated by different order resonances for the ORB1p and ORB2p, respectively. Counting the cycles of the dominating period in the residuals for  $m_{\max} = 100$  leads to approximately 47 for ORB1p and 39 for ORB2p. Because here only half the equator is shown there are 94 cycles for ORB1p in total and 78 for ORB2p, which is related to the largest order resonances at orders 94 and 78, respectively.

This characteristic of temporal aliasing is strongly connected with the SH order resonance analyses in Murböck et al. (2014). This is elaborated in more detail in Chap. 7. The results in Fig. 6.2 show the effects for diurnal variations. In reality the total temporal aliasing effect is dominated by the sum of tidal and non-tidal mass variations in system Earth. In the following the residuals for eight frequencies where such variations have their dominant amplitudes are analysed in the spectral domain.

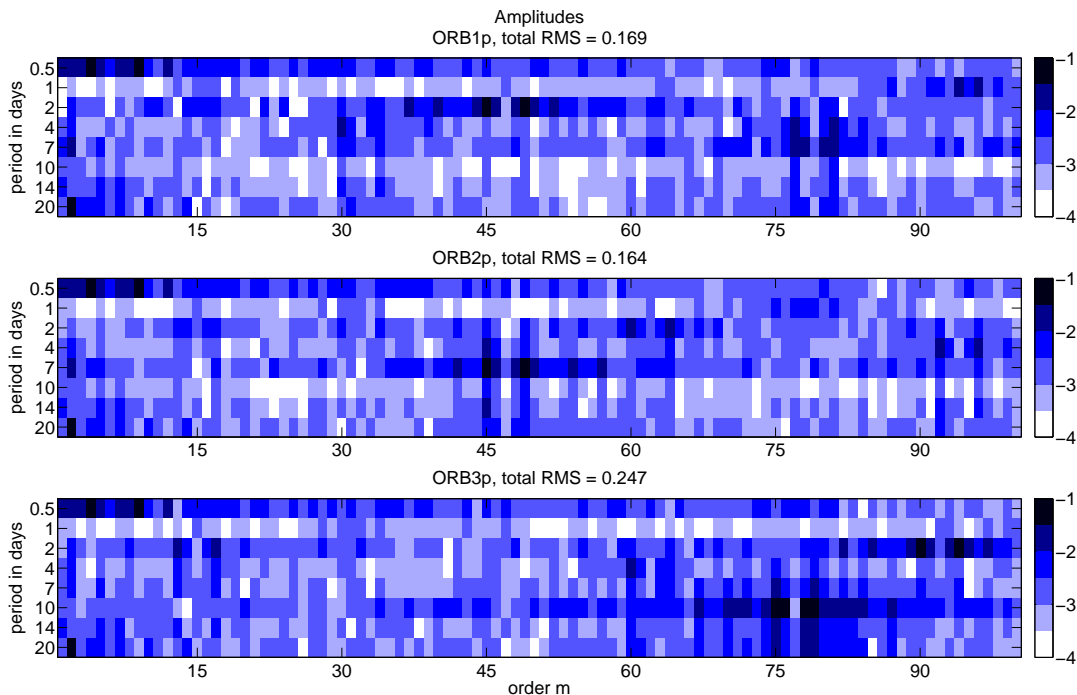


Figure 6.4: Unit-less order amplitudes ( $\log_{10}$ ,  $m_{\max} = 100$ ) of residuals wrt. the static signal for the three basic single polar pairs (ORB1p, ORB2p and ORB3p, cf. Tab. 4.1) for 8 different periods.

For the basic single and double orbits for ORB1, ORB2, and ORB3 (cf. Tab. 4.1) the same analysis is done for the eight periods  $T \in \{0.5, 1, 2, 4, 7, 10, 14, 20\}$  days. This selection contains possible alias frequencies of dominant signals of geophysical mass variations in system Earth or at least frequencies which are close to them. Such geophysical mass variations are due to ocean tides with dominant diurnal and semi-diurnal periods, or non-tidal oceanic and atmospheric variations with periods of a few days. But also for the periods between the selected periods there are geophysical mass variation periods.

The unit-less order amplitudes ( $\log_{10}$ ) of the residuals wrt. the static signal of all 9 solutions are shown in Fig. 6.4 (single solutions ORB1p, ORB2p, and ORB3p), 6.5 (double solutions ORB1p + ORB2p, ORB1p + ORB2p, and ORB1p + ORB3p), and 6.6 (double solutions ORB2p + ORB2p, ORB2p + ORB3p, and ORB3p + ORB3p). The amplitudes for each of the 8 periods are shown up to  $m_{\max} = 100$ . All single solutions show high residuals for the semi-diurnal period for small  $m$ . But these residuals are reduced for all double solutions.

Besides the order resonances for the single pairs for the diurnal period at  $m = 78$  and  $m = 94$  (cf. Fig. 6.2), Fig. 6.4 shows even stronger resonances for different orbits and periods. There is a strong resonance at  $m = 47$  for ORB1p for 2 days and two dominant resonances for ORB3p at  $m = 78$  for 10 days and at  $m = 94$  for 2 days. Another characteristic of all these resonance effects are less strong amplitudes exactly at the resonance order  $m_r$  and maximum amplitudes for  $m_r \pm 2$ .

As shown in Fig. 6.2 the combined solution on the one hand results in only slightly smaller residuals compared to the single pairs. But on the other hand the resonances of both single pairs occur in the combined solution. This is also visible in Fig. 6.5 and 6.6 in comparison with the single orbit resonances. All double solutions including ORB1p (Fig. 6.5) show the largest resonances of ORB1 as well, especially  $m = 47$  for 2 days. For orders and periods which are not affected by the resonances the double pair solution shows smaller residuals than the single pair. This is clearly visible, for example, for ORB1p + ORB1p (Fig. 6.5, top) in comparison with ORB1p (Fig. 6.4, top).

An optimal selection for a single and a double pair out of the basic scenarios can be done on the basis of the total RMS values of the analysis of the 8 periods. Table 6.1 gives the total RMS values and the relative improvement wrt. the worst scenario for this analysis (ORB3p). The pre-selection of the scenarios in Sec. 4.1 is already based on an analysis on optimization of orbit selection regarding temporal

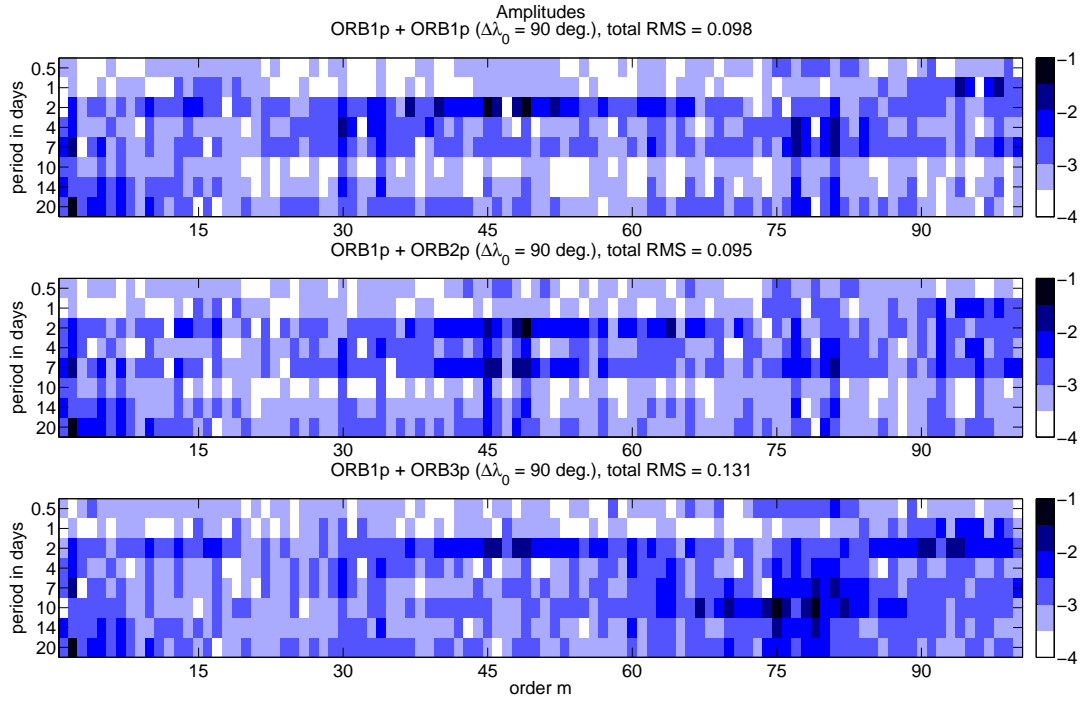


Figure 6.5: Unit-less order amplitudes ( $\log_{10}$ ,  $m_{\max} = 100$ ) of residuals wrt. the static signal for the three basic double polar pairs (ORB1p + ORB1p, ORB1p + ORB2p and ORB1p + ORB3p, cf. Tab. 4.1) for 8 different periods and an ascending node separation of  $90^\circ$ .

aliasing (Murböck et al., 2014). Therefore the total RMS of the different single scenarios differs only by up to 34%. ORB1 and ORB2 show a smaller total RMS than ORB3 and the double pairs without ORB3 show the smallest RMS. As for these 9 scenarios there are no large resonances above  $m = 100$ , the relative rating wrt. the total RMS does not change for  $m_{\max} = 140$ .

Table 6.1: Total unit-less RMS (over all periods and orders  $m$ ) for the equator sampling residuals.

	Total RMS				Improvement in % wrt. ORB3p			
	Single	Double			Single	Double		
		ORB1p	ORB2p	ORB3p		ORB1p	ORB2p	ORB3p
ORB1p	0.169	0.098	0.095	0.131	32	60	62	47
ORB2p	0.164		0.087	0.130	34		65	47
ORB3p	0.247			0.174	0			30

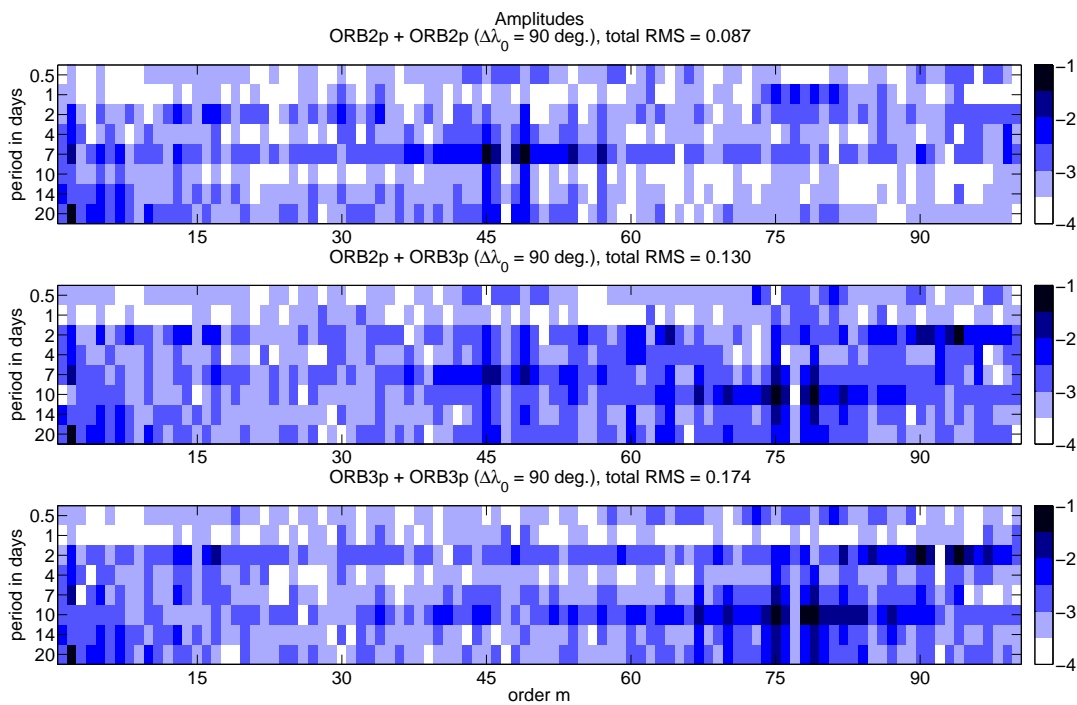


Figure 6.6: Unit-less order amplitudes ( $\log_{10}$ ,  $m_{\max} = 100$ ) of residuals wrt. the static signal for the three basic double polar pairs (ORB2p + ORB2p, ORB2p + ORB3p and ORB3p + ORB3p, cf. Tab. 4.1) for 8 different periods and an ascending node separation of  $90^\circ$ .

## 6.2 Spectral Analysis of Non-tidal Mass Variations

The numerical sampling exercise in Sec. 6.1 gives important insight into the error effects of temporal aliasing for discrete frequencies. In addition to this sampling effect of temporal aliasing, in gravity field retrievals as discussed in Chap. 7 there are upward continuation, and of course the functional model is different.

For ocean tides with their well-known discrete excitation frequencies it is reasonable to apply the analysis in Sec. 6.1 in order to estimate the sampling effects of temporal aliasing. Though the synthetic signal in Eq. (6.1) of course does not describe sufficiently the highly non-linear variations due to ocean tides especially in coastal areas. But the results in Chap. 7 show that one of the main characteristics of error effects due to temporal aliasing form both tidal and non-tidal signals is partly described and analysed with the numerical equator sampling in Sec. 6.1. These characteristics are SH order resonances depending on the orbit.

For the non-tidal mass variations in atmosphere (A), ocean (O), hydrology (H), ice (I), and solid Earth (S) the assumption of discrete frequencies is not sufficient. A spectral analysis of models for mass variations in AOHIS gives the information for the amplitudes for specific frequencies. The model with a temporal resolution of 6 hours and  $l_{\max} = 180$  is described in Gruber et al. (2011) and the data of January 2005 is used. The SH coefficients are provided separately for the 5 parts (AOHIS). There is also an updated version of this model described in Dobsław et al. (2014) which leads to comparable results.

After subtracting a mean and trend signal content, a discrete Fourier transform is applied to the time series for each SH coefficient. The results are SH coefficients of Fourier amplitudes for periods  $T$  between 0.5 and 30 days. Figure 6.7 shows the SH degree amplitudes in mm geoid height ( $\log_{10}$ ) of the Fourier amplitudes for the different periods for  $0 \leq l \leq 100$ . The beforehand subtracted mean and trend contents are also shown in the two top rows of each plot. Because AO (right) contains higher variations for short periods its variations are shown separately from HIS (left).

The means of HIS and AO are larger than the trend and the Fourier amplitudes. All degree amplitudes

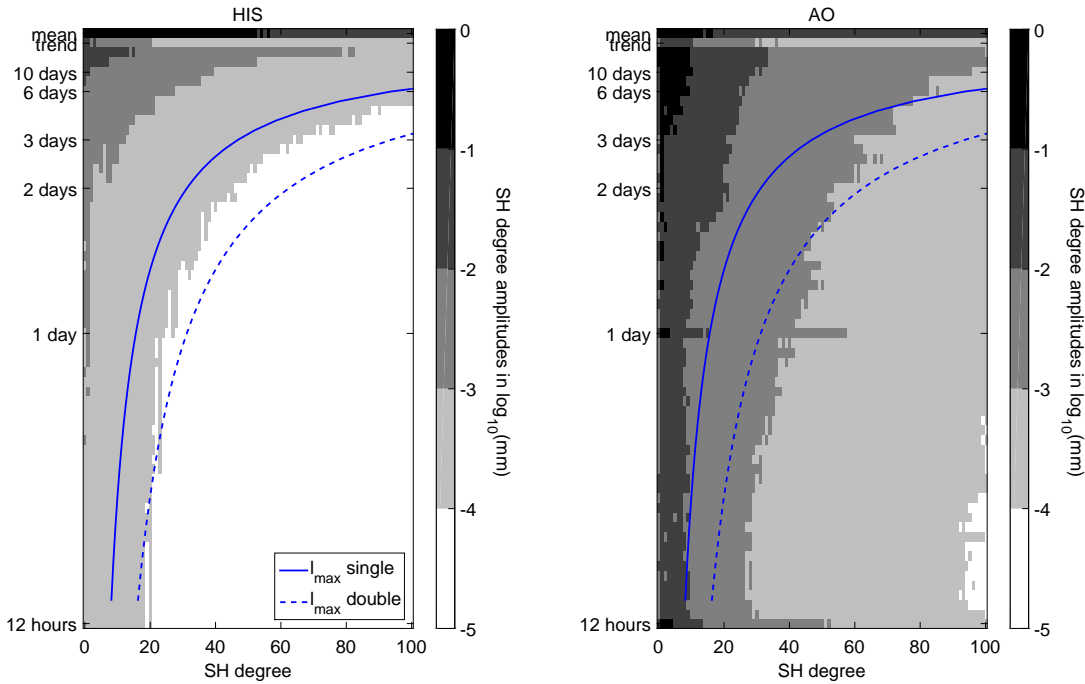


Figure 6.7: SH degree amplitudes in  $\log_{10}$  (mm) geoid heights of non-tidal temporal variations depending on the period in days. Left: hydrology, ice and solid Earth (HIS). Right: atmosphere and ocean (AO). The amplitudes for different periods are computed from the Fourier series of the AOHIS time series for January 2005 from Gruber et al. (2011). The blue lines approximate the maximum possible SH degree of expansion for a single and double pair respectively.

show approximately a  $l^{-3/2}$  behaviour in accordance with the Kaula-rule (Eq. (4.5)). Their largest Fourier amplitudes of more than 0.1 mm geoid height are visible for AO for  $l < 10$  and  $T < 3$  days. For all periods AO shows amplitudes of more than 0.01 mm for  $l < 20$  (30 days) and  $l < 10$  (12 hours). A peak occurs for the diurnal period. The only component showing larger amplitudes for HIS than for AO is the mean. For all Fourier amplitudes HIS amplitudes are smaller than AO amplitudes by more than a factor of 10. This means that the gravitational potential of HIS is smoother than the one of AO for all periods analysed in this study.

The distribution of amplitudes for HIS and AO is also analysed depending on the SH order (Fig. 6.8) analogously to Fig. 6.7. Again there is a  $m^{-3/2}$  behaviour. The HIS part shows larger amplitudes than AO only for  $T < 10$  days and for high SH orders. Neglecting  $m = 0$  and  $m = 1$  there are no larger HIS amplitudes than 1  $\mu\text{m}$  for  $T < 2$  days. Therefore the largest temporal aliasing effects from non-tidal sources in a gravity field retrieval are due to AO.

The maximum SH degree and order which can be reached with LEO single and double orbits is displayed in all plots of Figs. 6.7 and 6.8. With  $N_{\text{rev}}$  equally spaced revolutions a spectral resolution is reached according to  $l_{\text{max}} = N_{\text{rev}}$ . For example, the signals which lead to temporal aliasing in a 3 day single orbit solution (approximately 47 revolutions) are signals with periods  $T < 6$  days (Nyquist) and  $l < 47$  and  $m < 47$ .

This directly leads to a promising method to reduce temporal aliasing. The idea of the method described in Wiese et al. (2011) is the amplitude reduction of the signals leading to temporal aliasing. This reduction is reached by estimating short period low resolution gravity fields together with one high resolution gravity field for the whole observation period.

From the analysis of Fig. 6.7 and 6.8 an extension of this method is derived without elaborating it in more detail. Optimum temporal aliasing reduction is reached when estimating as much of the temporal variations as possible. This could be assessed by estimating not only daily low resolution gravity fields but a series of gravity fields for several periods up to the highest possible SH degree and order (cf. Sec. 8.2).

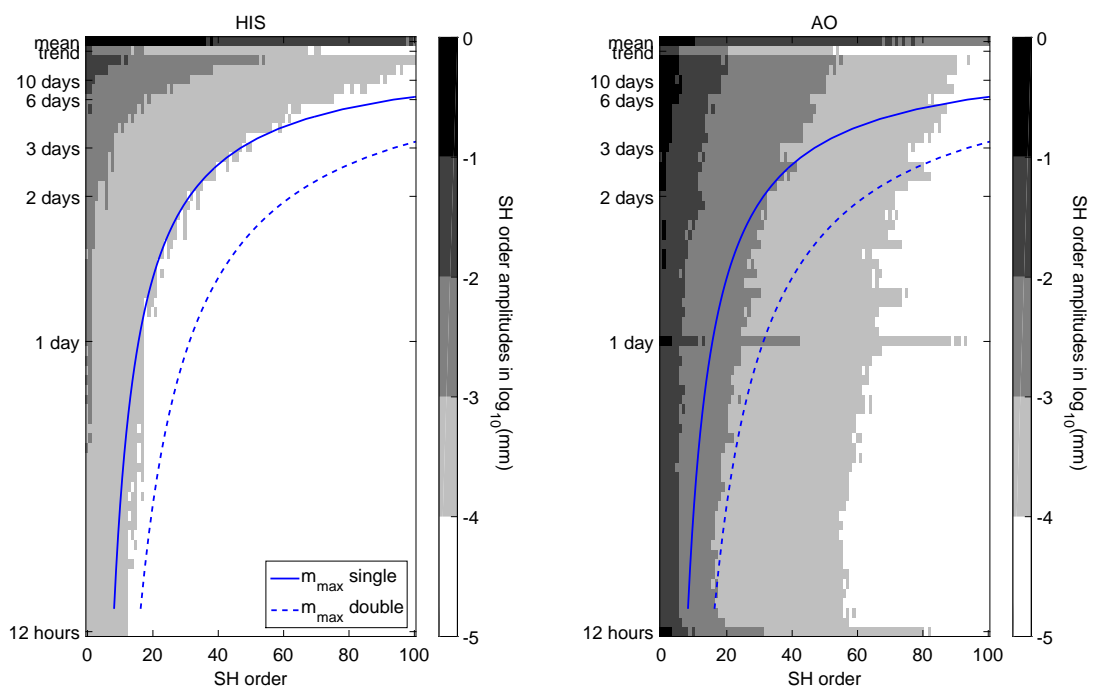


Figure 6.8: SH order amplitudes in  $\log_{10}(\text{mm})$  geoid height of non-tidal temporal variations depending on the period in days. Left: hydrology, ice and solid Earth (HIS). Right: atmosphere and ocean (AO). The amplitudes for different periods are computed from the Fourier series of the AOHIS time series for January 2005 from (Gruber et al., 2011). The blue lines approximate the maximum possible SH order of expansion for a single and double pair, respectively.



## 7 Optimal Orbits regarding Temporal Aliasing

In this chapter it is discussed how optimal orbits regarding temporal aliasing can be determined. This topic is strongly connected with the analyses in Chap. 6. In the conclusions of Murböck et al. (2014) possibilities are shown of how to reduce temporal aliasing for single and double pairs. Optimal altitude bands regarding temporal aliasing for the NGGM are derived as well.

### 7.1 Spherical Harmonic Order Resonances

In Murböck et al. (2014) it is shown that errors due to temporal aliasing from tidal and non-tidal sources affect mainly specific SH order bands. These orders are referred to as SH resonance orders, and they only depend on the two basic rates of a satellite orbit, i.e. the rate of the argument of the latitude  $\dot{u}$  and of the Earth fixed longitude of the ascending node  $\dot{\Lambda}$  (cf. Eq. (2.32)). With  $-l_{\max} \leq k \leq l_{\max}$  these two parameters define the observation frequencies  $\omega(m)$  of a signal along the satellite orbit, which are mapped on the SH order  $0 \leq m \leq l_{\max}$  (Sneeuw, 2000)

$$\omega(m) = k\dot{u} + m\dot{\Lambda}. \quad (7.1)$$

This equation can be evaluated in terms of frequencies in units of Hz or in terms of angular rates. The smaller the absolute minimum value of  $\omega(m)$ , the larger is the resonance effect from temporal aliasing. For orbits between 200 and 600 km altitude strong temporal aliasing effects are expected at SH order  $m$  when  $\min(|\omega(m)|) \leq 1.8 \cdot 10^{-6}$  Hz ( $\approx \dot{u}/100$ ) (Murböck et al., 2014).

Figure 7.1 shows  $\min(|\omega(m)|)$  in  $\log_{10}$  (Hz) for polar orbits ( $I = 89^\circ$ ) between 200 and 600 km altitude and  $m \leq 150$ . Orders with small frequency are affected by resonance effects. The critical limit of  $1.8 \cdot 10^{-6}$  Hz (5.6 days period) is marked with a gray line. In order to minimize the disturbance of monthly gravity field retrievals by temporal aliasing resonance effects orbits with strong resonances in low SH orders should be avoided. Therefore 4 optimal altitude bands for polar LEOs are selected, i.e. around 301, 365, 421, and 487 km altitude (Murböck et al., 2014). The pre-selection of the basic scenarios (Tab. 4.1) is done based on these altitude bands.

It can be seen, that the resonances occur at integer multiples of the numbers of revolutions per day, i.e.  $-\dot{u}/\dot{\Lambda}$  which is equal to  $N_{\text{rev}}/N_{\text{day}}$  for circular repeat orbits. For the selected orbits this ratio is between 15 and 16. The pattern in Fig. 7.1 corresponds to specific repeat cycles. The absolute minima are reached for short period repeat cycles. A  $N_{\text{day}}$  days repeat orbit has its largest resonances at all integer multiples of  $N_{\text{rev}}$ . One day polar repeat orbits with 15 and 16 revolutions, respectively, are in altitudes of 548 and 256 km, respectively. Between these 1 day cycles one 2 day cycle is shown with 31 revolutions at 398 km altitude (cf. Fig. 2.2). This 2 day cycle shows its largest resonances at all even multiples of  $m = 2 \cdot 15.5 = 31$ . In addition to the discussions on these resonances in Kim (2000) the connection with temporal aliasing errors is explained in Murböck et al. (2014).

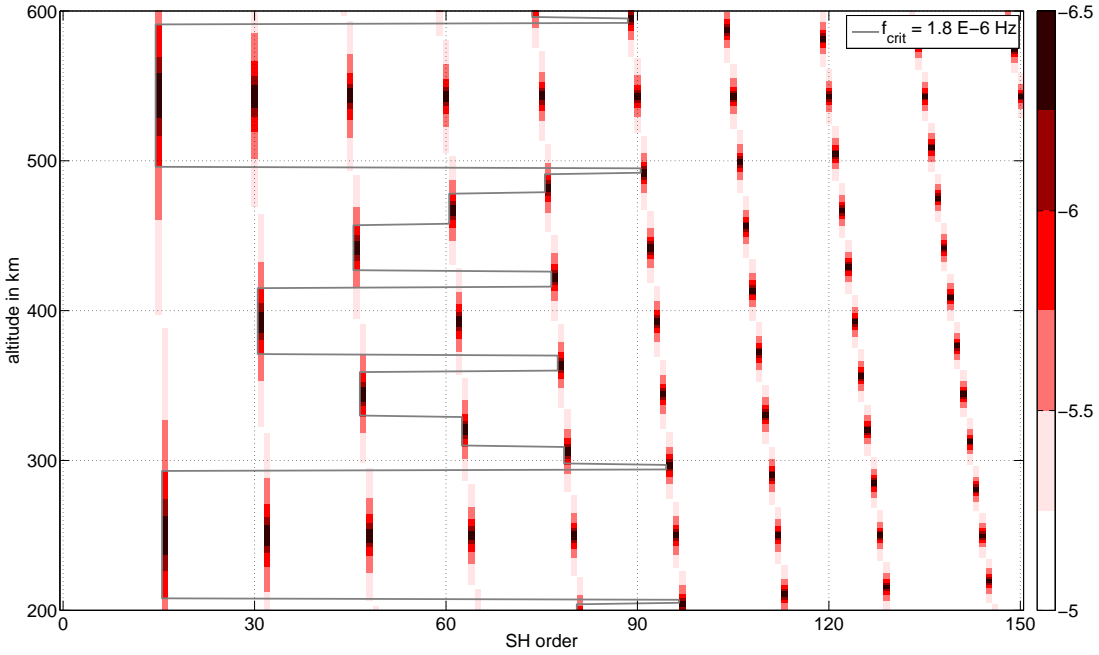


Figure 7.1: SH order resonances in  $\log_{10}$  (Hz) for polar orbits between 200 and 600 km altitude. The gray lines mark the max. SH orders without strong resonances (values below  $1.8 \times 10^{-6}$  Hz) (Murböck et al., 2014).

## 7.2 GRACE Resonances

These resonances are also visible in current monthly GRACE solutions. A representation is shown for the official release 5 solutions of CSR, GFZ, and JPL and for ITSG-Grace2014 (cf. Tab. 2.3). More than 8 years (August 2002 to December 2010) of monthly GRACE solutions up to  $l_{\max} = 90$  (96 for CSR RL05) are used for this analysis. Figure 7.2 shows residual SH order amplitudes of all monthly solutions. In the following it is explained how these residual SH order amplitudes are derived.

The dominating contents in each monthly solution  $\bar{K}_{lm}$  are the mean gravity signal for this month, stochastic noise (mainly from the microwave ranging instrument and from the accelerometers) and non-stochastic errors from temporal aliasing. At first the mean SH coefficients for the whole time series are subtracted. Hence, the signal part in each monthly residual  $\Delta\bar{K}_{lm}$  is reduced to the difference wrt. this mean representing mainly hydrology and ice mass distributions.

SH order amplitudes are computed for each residual monthly solution  $\kappa_{\text{amp}}(m, \Delta\bar{K}_{lm})$  (Eq. (2.11)). A smooth behaviour of the logarithm of the SH order amplitudes for the residual signal and the stochastic noise is assumed. Hence, a best fitting low degree polynomial  $P_n(m)$  with coefficients  $a_i$  ( $0 \leq i \leq n$ ) is able to reduce these two components ( $m = 0$  is excluded from the polynomial fitting). A degree  $n = 4$  for the polynomial is chosen and the residual SH order amplitudes read

$$\Delta\kappa_{\text{amp}}(m, \Delta\bar{K}_{lm}) = \log_{10}(\kappa_{\text{amp}}(m, \Delta\bar{K}_{lm})) - P_n(m) = \log_{10}(\kappa_{\text{amp}}(m, \Delta\bar{K}_{lm})) - \sum_{i=0}^4 a_i m^i. \quad (7.2)$$

Please note that the residual SH order amplitudes in Eq. (7.2) are evaluated in  $\log_{10}(\kappa_{\text{amp}})$ . The values in Fig. 7.2 range from  $-0.5$  to more than  $1$ . For values of  $1$  the SH order amplitudes  $\kappa_{\text{amp}}(m, \Delta\bar{K}_{lm})$  are 10 times larger than the smooth polynomial in  $m$ . The largest residual SH order amplitudes and thereby the largest resonances are around  $m = 60$  in 2004 for all four solutions. Figure 7.1 shows this resonance at 470 km altitude. During the whole period the altitude of GRACE decreases from approximately 490 to 460 km. All four solutions show the  $m = 75$  resonance at the very beginning in 2002 and the  $m = 45$  resonance approximately from 2008 to 2011. Only the CSR RL05 shows the

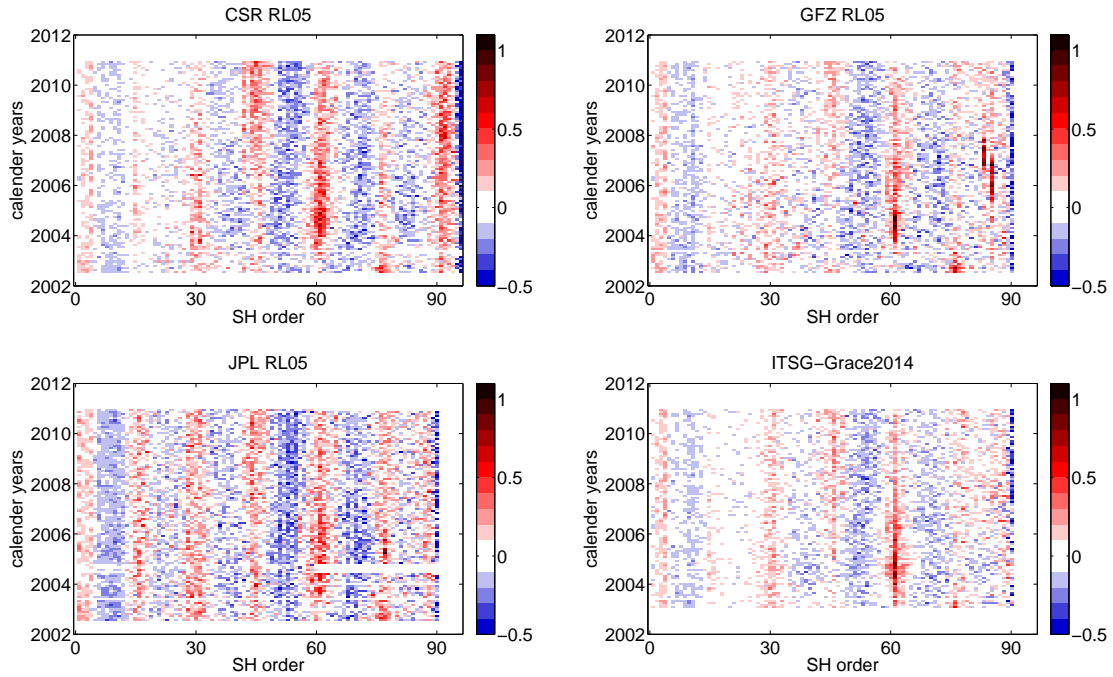


Figure 7.2: SH order resonances in four GRACE solutions, i.e. RL05 of CSR (top left), GFZ (top right) and JPL (bottom left) and ITSG-Grace2014. Shown are reduced SH order amplitudes for each monthly solution.

$m = 90$  resonance for the whole period. A possible reason for this is the higher  $l_{\max}$  compared to the other three. Furthermore, the residual order amplitudes of GFZ RL05 contain large values at  $m = 83$  and  $m = 85$  in 2006 which can not be explained by the order resonances in Fig. 7.1.

From GRACE orbit data the basic rates  $\dot{u}$  and  $\dot{\Lambda}$  are derived in diurnal mean values. Equation (7.1) gives  $\omega(m)$  and  $\min(|\omega(m)|)$  is computed for the whole period. Figure 7.3 shows the resonance periods  $1/\min(|\omega(m)|)$  for the mainly affected orders (center and right). These periods are compared with the total RMS of the mean reduced solutions for the four GRACE solutions in Fig. 7.2.

In the period from 2007 to 2009 there are the smallest RMS between 5 and 10 mm geoid height. Before 2007 the RMS is increased, and especially in 2002 and 2004 it contains peak values between 30 and 50 mm for the different solutions. Obviously the total RMS of the GRACE solutions is related with the SH order resonances. The peaks occur for the periods when GRACE meets a 5 day repeat cycle in 2002 and a 4 day repeat cycle in 2004. The  $m = 61$  resonance dominates the observed period, and a possible reason for the increased total RMS in 2003 and 2005 is this resonance. As the  $m = 61$  resonance period decreases towards 2011 the total RMS decreases as well. In 2010 the  $m = 46$  resonance becomes the dominant part, and this could be a reason for the again increased RMS.

It is shown that the gravity retrieval performance of GRACE depends on the SH order resonances. Excluding the peak values for the short period repeat cycles, the total RMS increases by up to a factor of 2 from periods with low resonances for all orders to periods with increased resonance periods. Furthermore, Chap. 6 explains the relation of these resonances with temporal aliasing. For the NGGM it is required to avoid high resonances, i.e. large resonance periods. As the NGGM has increased instrument accuracies wrt. GRACE temporal aliasing will be the dominant error source of the NGGM. Therefore taking into account the resonance effects becomes even more important.

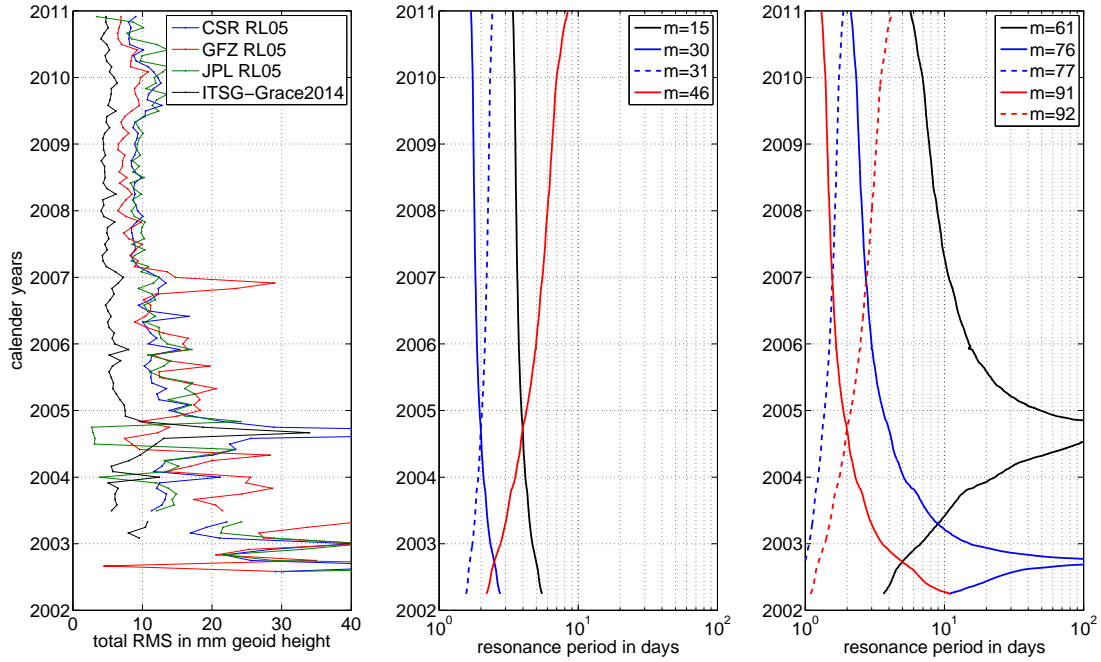


Figure 7.3: Total RMS in mm geoid height of the residual coefficients wrt. the mean of the four monthly GRACE solution series.

## 7.3 Order Resonance Reduction

Temporal aliasing effects are reduced with dedicated satellite formations, e.g. a double Bender-type pair or a single Pendulum formation (cf. Sec. 4.1). Furthermore, a clever orbit choice avoids the largest SH order resonances (Murböck et al., 2014). But the knowledge of the SH order resonances can also directly be used in order to reduce resonance effects. Two examples for such methods are explained in Secs. 7.3.1 and 7.3.2 based on LCLA results.

### 7.3.1 Weighting of Double Pairs

In Sec. 6.1 it is shown that each order resonance of a single pair is also an order resonance of a double pair solution including this single pair. If two single pairs have different order resonances the relative weighting should account for the larger errors around the affected SH orders. This idea is tested on the basis of polar double low-low SST pair simulations regarding tidal and non-tidal temporal aliasing. The chosen scenarios consist of GRACE-like 31 day repeat orbits for which the orbit parameters are given in Tab. 7.1.

The low-low SST observations are computed from the tidal models EOT08a and FES2004 and from

Table 7.1: Basic orbit parameters for the simulations in Sec. 7.3.

Nodal days	31
Revolutions	472, 475, 477, and 479
Altitudes	410 to 480 km
Inter-satellite distance	220 km
Start epoch	March 1, 2004

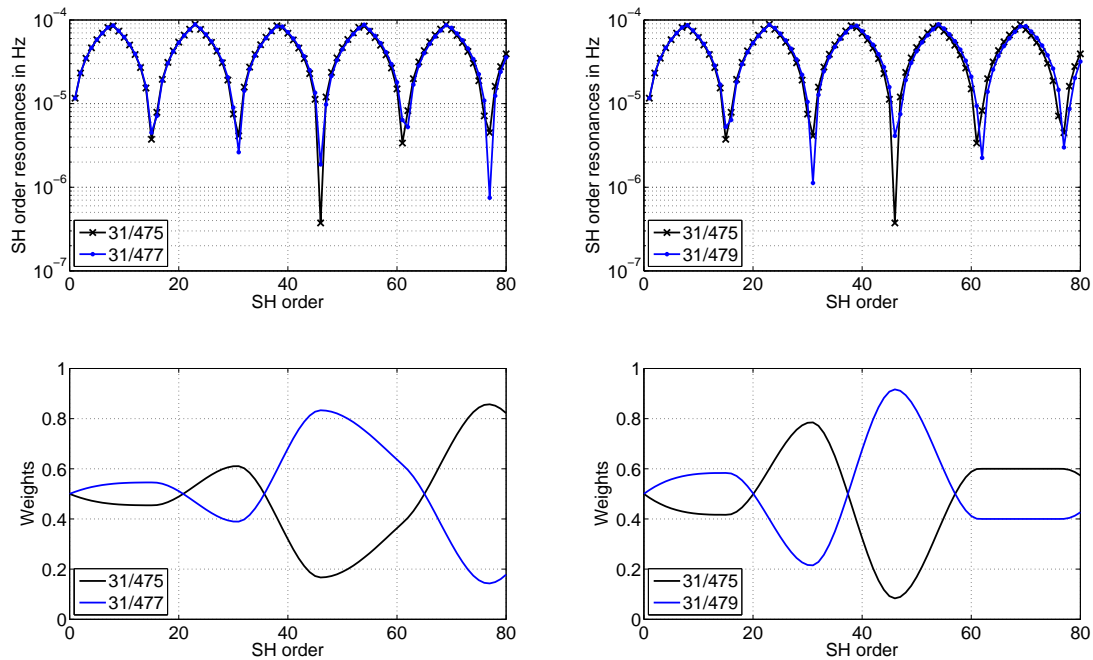


Figure 7.4: SH order resonance frequencies in Hz for two double polar pairs consisting of 31/475 with 31/477 (top left) and 31/479 (top right), respectively. SH order depending weights (bottom) for the two double pairs derived from the peak value relations of the SH order resonance frequencies.

the non-tidal AOHIS models (cf. Tab. 2.3) without a static gravity model. A de-aliasing approach is applied for the ocean tides and AOHIS. This means that high-frequency signal content is reduced in order to reduce temporal aliasing effects. Therefore the full signal of EOT08a is reduced by FES2004 and the AO part of AOHIS is reduced by its mean. Assuming independent observations a white noise in terms of range accelerations with a standard deviation of  $10^{-10}$  m/s<sup>2</sup> is added.

One set of gravity field parameters is estimated from the monthly observations up to  $l_{\max} = 80$  separately from the tidal and the non-tidal observations, i.e. EOT08a – FES2004 and AO – mean(AO). The results contain the temporal aliasing effects from tidal and non-tidal sources, and therefore SH order resonances are expected. Figure 7.4 (top) shows the SH order resonance frequencies  $\min(|\omega(m)|)$  (Eq. (7.1)) in  $\log_{10}$  Hz for two polar ( $I = 89^\circ$ ) 31 days double pairs (31/475 with 31/477, and 31/479, respectively), respectively. The largest resonances are at  $m = 46$  for 31/475, at  $m = 77$  for 31/477, and at  $m = 31$  for 31/479.

The relative weights of the two orbits in a double pair shall account for the large resonances in each pair. Therefore they depend on  $m$  and are computed from the relation between the resonance frequencies at the peak values (multiples of approximately 15). For the combination of 31/475 and 31/479 (top left) for  $m = 46$  this relation is approximately 0.1. Between these values the weights are interpolated with a piecewise cubic interpolation. Figure 7.4 (bottom) shows the weights for each single pair of the two double pairs.

The weights for each pair  $w_i(m)$  ( $i \in \{1, 2\}$  and  $w_1 + w_2 = 1$ ) are applied to all coefficients and the combined coefficients are the weighted mean values

$$\bar{K}_{lm,\text{combination}} = w_1(m) \bar{K}_{lm,1} + w_2(m) \bar{K}_{lm,2}. \quad (7.3)$$

This combination does neither take into account the variances nor covariances but only the relative resonance frequencies. For comparison a rigorous combination on normal equation level is assessed as well (Eq. (2.17)). This rigorous combination takes into account only the variances and co-variances into account but not the resonances.

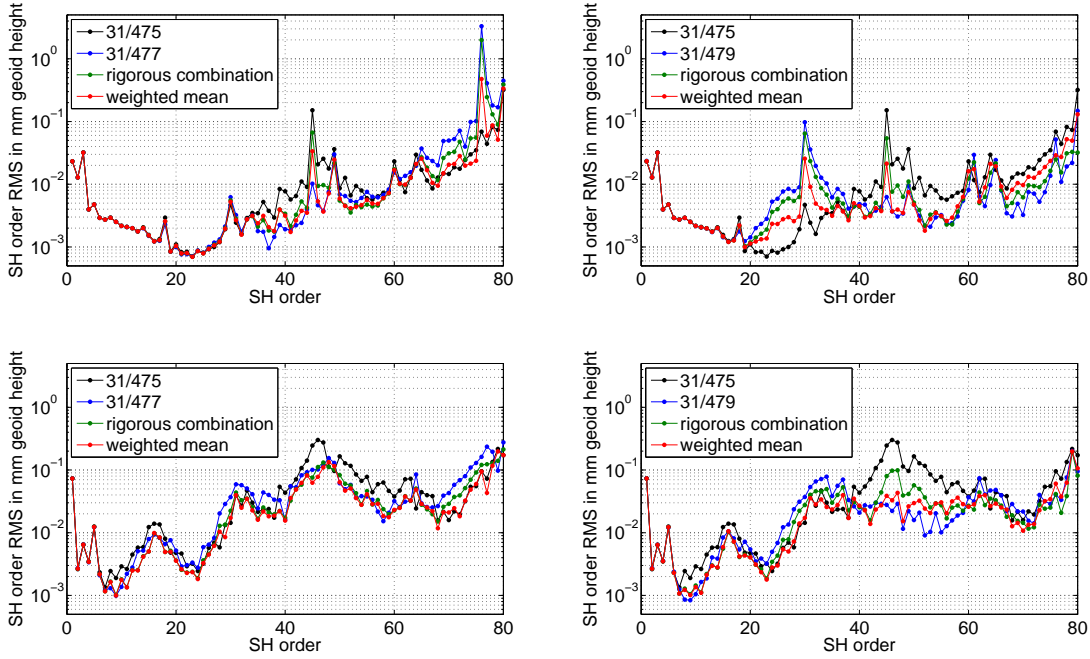


Figure 7.5: SH order RMS (Eq. (2.11)) in mm geoid height for each single pair (black and blue, cf. Tab. 7.1) and the two different combinations (red: weighted mean, green: rigorous) for tidal (top) and non-tidal (bottom) de-aliasing errors.

The results are shown in Fig. 7.5 in terms of SH order RMS (Eq. (2.11)) in mm geoid height for each single pair and the two different combinations, respectively. All curves represent temporal aliasing from background model error assumptions, and the range is between  $1 \mu\text{m}$  and  $1 \text{mm}$ . The ocean tide aliasing (top) shows pronounced peak values at the resonance orders, whereas the non-tidal results (bottom) are smoother. Similar to Sec. 6.1 the rigorous combination (green) suffers from all resonances of the single pairs nearly with the same RMS. In contrast, the weighted mean combinations (red) result in smaller resonance effects than the rigorous combination by down weighting the affected single pairs. Therefore the weighted mean combination shows smaller temporal aliasing effects, especially around the order resonances.

This effect of temporal aliasing reduction by weights depending on the SH order resonances is also visible in the spatial domain. In Fig. 7.6 global geoid heights on a  $1^\circ \times 1^\circ$  grid computed up to  $l_{\text{max}} = 80$  are displayed for the tidal double pair results in Fig. 7.5 (top). There is a strong systematic error effect for

Table 7.2: Statistics of global geoid height residuals in mm for .

		Tidal aliasing						Non-tidal aliasing					
		472	472	472	475	475	477	472	472	472	475	475	477
		475	477	479	477	479	479	475	477	479	477	479	479
rigorous combination	RMS	2.4	8.1	1.6	6.4	1.1	4.3	3.6	2.7	1.9	2.9	2.3	1.8
	min	-9.1	-36	-5.6	-29	-4.5	-19	-20	-17	-16	-17	-14	-11
	max	9.7	32	7.6	28	6.8	17	20	15	14	17	14	11
weighted mean	RMS	1.9	4.0	2.2	1.8	0.80	2.5	2.3	2.1	1.9	2.7	1.6	1.6
	min	-6.8	-18	-7.4	-11	-3.4	-11	-16	-11	-9.7	-16	-9.9	-11
	max	7.2	15	8.0	9.3	3.6	9.9	15	12	9.7	15	9.2	9.8

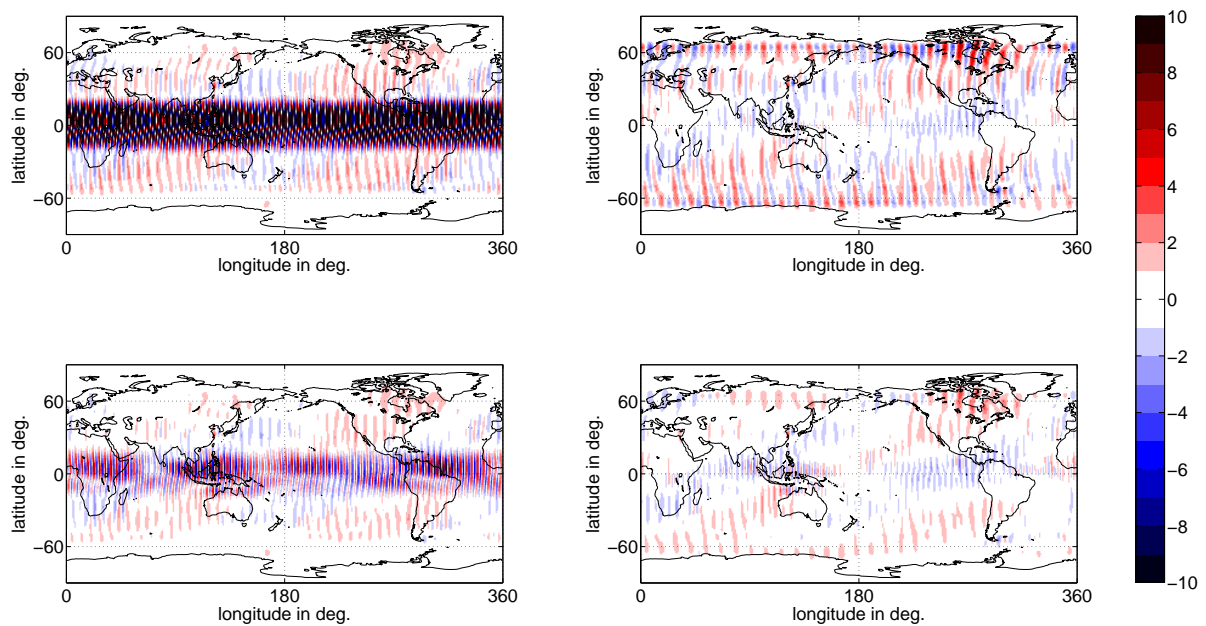


Figure 7.6: Global geoid height residuals in mm for the double pair tidal aliasing results in Fig. 7.5 (top) computed on a  $1^\circ \times 1^\circ$  grid up to  $l_{\max} = 80$ . Top: rigorous combination of 31/475 with 31/477 (left) and 31/479 (right). Bottom: weighted mean (Eq. (7.3)).

the rigorous combination of 31/475 and 31/477 (top left) in terms of latitudinal stripes with amplitudes of more than 1 cm geoid height. It is mainly caused by the strong resonance at  $m = 77$  (Figs. 7.4 and 7.5). These effects are less prominent for the second double pair (top right), but they are reduced with the weighted mean solutions for both double pairs (bottom).

The global RMS for the rigorous combinations is 6.4 mm (top left) and 1.1 mm (top right). It is reduced with the weighted mean solutions to 1.8 mm (by a factor of 3.6) and 0.8 mm (by a factor of 1.4), respectively. The global RMS (and min. and max.) for all double pairs for tidal and non-tidal temporal aliasing and for the two combination approaches is summarized in Tab. 7.2. Only for one double pair (31/472 with 31/479) the weighted mean solution does not lead to a smaller global RMS. On average the weighted mean solutions lead to smaller global RMS of tidal aliasing errors by a factor of 1.8. For the non-tidal results this factor is 1.3.

It is shown that the SH order resonances should be used in order to reduce temporal aliasing effects. The approach of SH order depending weighting could be further improved by taking into account also the variances and co-variances of the single solutions. This is even more important for Bender-type double pairs. Because without applying the variances and covariances for the combination it cannot be taken full advantage of the improved observation geometry with the polar and the inclined pair.

### 7.3.2 Single Pair Regularization

In Sec. 7.3.1 order resonances are used to optimize the relative weighting of a double low-low SST constellation. Here it is explained how the knowledge of the order resonances can be applied for the regularization of a single pair in order to reduce temporal aliasing. In least squares adjustment (LSA) regularization means the combination (Eq. (2.17)) with a regularization matrix  $\mathbf{R}$  and corresponding pseudo observations  $\mathbf{l}_0$ . Assuming independent  $\mathbf{l}_0$  the least squares estimate of the unknowns reads

$$\hat{\mathbf{x}} = (\mathbf{A}^T \mathbf{P} \mathbf{A} + \mathbf{R})^{-1} (\mathbf{A}^T \mathbf{P} \mathbf{l} + \mathbf{l}_0). \quad (7.4)$$

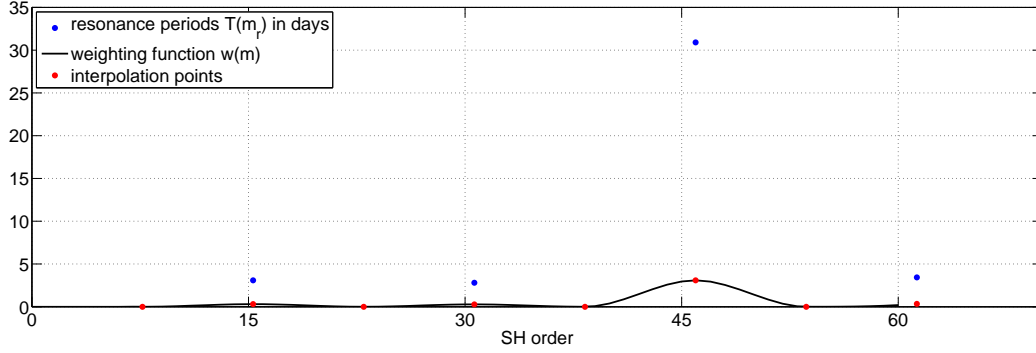


Figure 7.7: Weighting function for regularization according to resonance periods for the 31/475 orbit.

Regularization can be used to reduce SH order resonances from temporal aliasing. The deterministic error effects around the resonance orders are to be reduced by applying regularization at these orders depending on the resonance periods. As no a priori information shall be used here the pseudo-observations are zero  $\mathbf{l}_0 = 0$  and  $\mathbf{R}$  is a diagonal matrix with non-zero entries  $w(m) \cdot \text{diag}(\mathbf{A}^T \mathbf{P} \mathbf{A})$  for  $m > m_{\min}$ . The empirical weighting function  $w(m)$  is again derived by piecewise cubic interpolation of values at the resonance orders  $m_r$  depending on the resonance period  $T(m_r)$ . It reads

$$w(m_r) = a \cdot T(m_r)^e \quad (7.5)$$

with regularization parameters  $a \geq 0$  and  $e \geq 0$ . In between the resonance orders there should be no regularization, and therefore zero weights are introduced there as interpolation points. As  $a$  and  $e$  are positive,  $w(m_r)$  is positive as well and the regularized normal equation matrix  $\mathbf{A}^T \mathbf{P} \mathbf{A} + \mathbf{R}$  is the same except for increased values on the diagonal by  $w(m_r)$  for  $m > m_{\min}$ .

In Fig. 7.7 the resonance periods together with the weighting function are shown for the 31/475 orbit (cf. Tab. 7.1) with the empirically derived regularization parameters  $a = 0.1$  and  $e = 1$  up to  $l_{\max} = 60$ . The resonance periods are the inverse of the resonance frequencies in Fig. 7.4 (top black). At  $m_r = 46$  the resonance period is 31 days, and therefore the weighting function at this order is  $w(m_r = 46) = 0.1 \cdot 31^1 = 3.1$ . Hence, the regularization accounts for the large resonance at  $m = 46$  with introducing pseudo zero observations with weights more than 3 times larger than the diagonal elements of the unregularized normal equation matrix around this order.

This regularization is tested for ocean tide aliasing similar to Sec. 7.3.1. The low-low SST observations are computed from the difference between the two ocean tide models EOT08a and FES2004 plus the mean hydrology and ice signal (HI) for March 2004. The unregularized residuals wrt. mean HI are shown up to  $l_{\max} = 60$  in Fig. 7.8 (left, blue curves) in terms of SH degree and order RMS, respectively. It can be seen that the large resonance at  $m = 46$  leads to increased residuals (even larger than mean HI) for SH degrees  $l > 45$ . The SH order RMS show more pronounced peaks around  $m = 46$ .

An important parameter for the regularization is  $m_{\min}$ . Applying the regularization for orders where the signal (mean HI) to noise (EOT08a – FES2004) ratio is high would deteriorate this ratio. Therefore the regularization should only be applied for  $m > 38$  (between the resonances at  $m = 31$  and  $m = 46$ ). The effect is seen in the regularized results in terms of SH degree and order RMS in Fig. 7.8 (left, red curves). The regularization decreases the residuals for nearly all affected SH degrees and orders below the mean HI signal. The order dependent regularization effect is also shown for the whole spectrum (top right) in terms of  $\log_{10}$  residual relations. Values of  $-1$  mark coefficients where the residuals after regularization are decreased by a factor 10. It can be seen that the regularization improves all SH degrees in a broad band around  $m = 46$ .

The improvement of this ocean tide aliasing reduction with order dependent regularization is also shown in the spatial domain. Similar to the approach described in Sec. 7.3.1 the regularization decreases the systematic latitudinal striping pattern. The global RMS is decreased from 0.9 mm for the unregularized

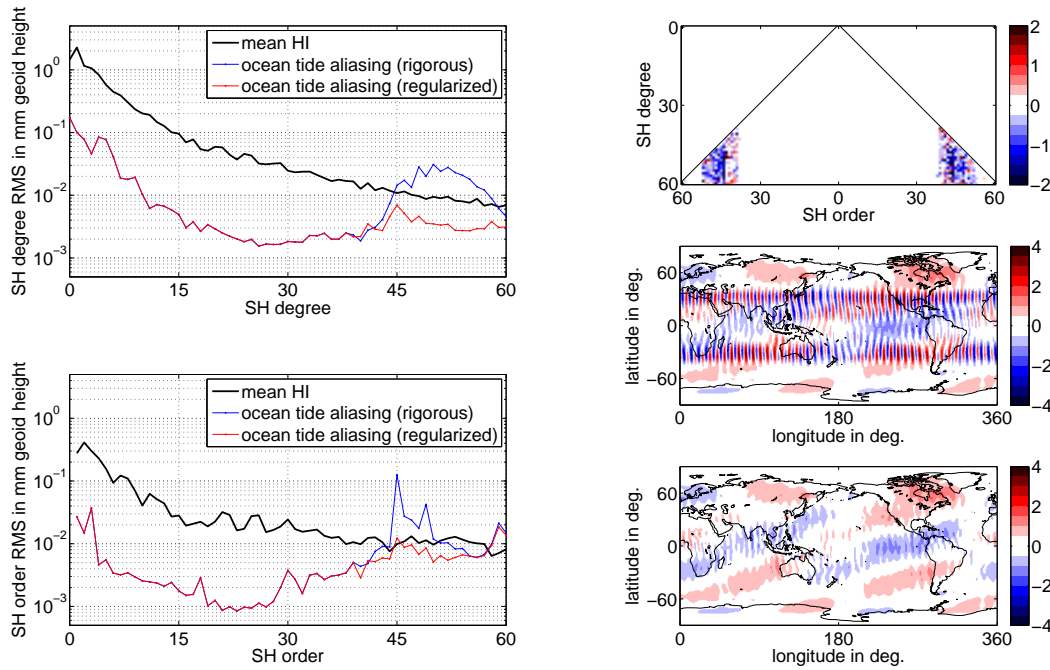


Figure 7.8: Effects of regularization according to SH order resonances for the 31/475 orbit with tidal aliasing up to  $l_{\max} = 60$ . Left: SH degree (top) and order (bottom) RMS in mm geoid height for the residuals of the unregularized and the regularized solution wrt. the mean HI signal. Top right: unregularized residuals wrt. mean HI divided by regularized residuals ( $\log_{10}$ ). Right: global geoid height residuals in mm for the unregularized (center) and the regularized (bottom) solution computed on a  $1^\circ \times 1^\circ$  grid up to  $l_{\max} = 60$ .

residuals by nearly a factor of 2 to 0.5 mm for the regularized residuals. From both analyses, in this section and Sec. 7.3.1 it is concluded, that the information of the SH order resonances can be used to reduce temporal aliasing effects from tidal and non-tidal signals.

Applying a regularization in general means that the estimated coefficients are not un-biased any more. They are biased towards the pseudo-observations according to  $\mathbf{R}$  which plays the role of the normal equation matrix for the pseudo-observations. In order to minimize signal corruption regularization should only be used for unknowns with small signal to noise ratio. This is the case in the here discussed example of reducing SH order resonances.



## 8 Proposed Mission Scenarios

In this chapter gravity field retrieval results of the mission scenarios which are proposed for the NGGM are elaborated. The results are analysed in the spectral and spatial domain, and the major error sources are taken into account. One major error source is stochastic instrument noise for which in Chap. 4 the requirements are derived for basic orbits (Tab. 4.1). But the dominating error source is temporal aliasing from tidal and non-tidal sources. One of the main characteristics of temporal aliasing are SH order resonances which are discussed in Chaps. 6 and 7.

The basic orbits are chosen in specific altitude bands where large resonances do not occur in low SH degrees and orders (Murböck et al., 2014). The resonance periods for the three basic orbits ORB1, ORB2, and ORB3 are shown in Fig. 8.1 up to  $m_{\max} = 140$ . The dominant resonances with resonance periods larger than 10 days are at  $m = 95$  for ORB1, at  $m = 78$  and  $m = 125$  for ORB2, and at  $m = 108$  and  $m = 77$  for ORB3. In Sec. 7.3 it is shown how the resonances can be reduced, especially for a bad signal-to-noise ratio (Sec. 7.3.2). These methods are not applied in this chapter.

The mission scenarios proposed for the NGGM are double Bender-type low-low SST pairs and Pendulum formations in three different altitudes (cf. Chap. 4). The combined scenario with low-low SST and radial SGG is neglected, because current instrument accuracies of SGG are not sufficient to significantly contribute to a low-low SST solution with laser accuracy.

In the first part of this chapter low resolution (31 days,  $l_{\max} = 80$ ) gravity retrieval results are discussed in order to see the impact of tidal and non-tidal temporal aliasing for the different scenarios (Sec. 8.1). Another method to reduce temporal aliasing is elaborated in Sec. 8.2 on the basis of gravity retrievals with high temporal resolution (0.5, 1, and 2 days).

The scheme of the simulations is displayed in Fig. 2.4 and the references for the background models can be found in Tab. 2.3. The total low-low SST observation noise for the three basic scenarios is derived from scaling the spectrum of normally distributed numbers according to the total noise model

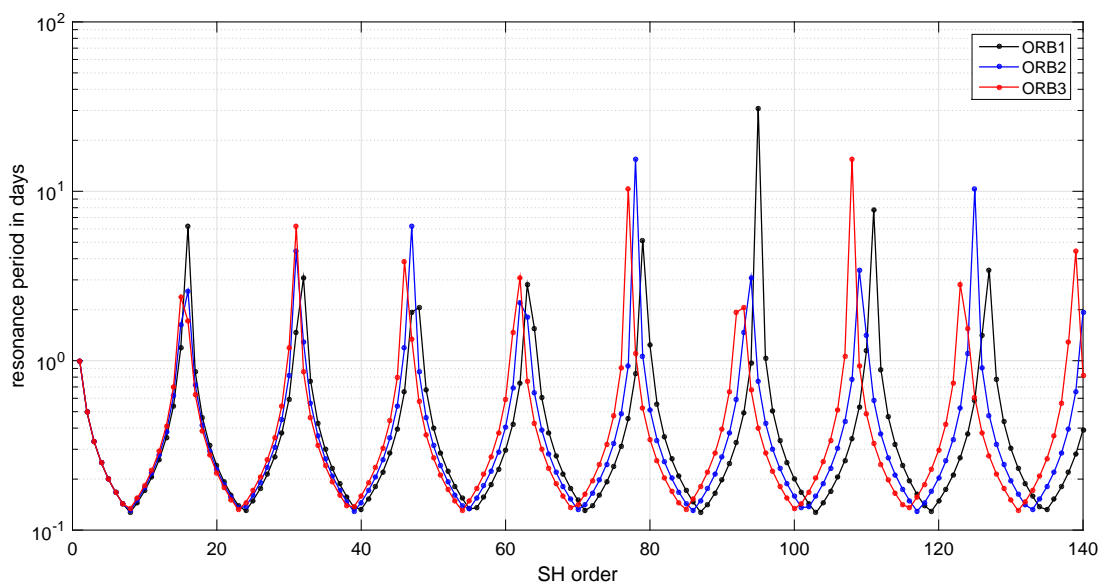


Figure 8.1: SH order resonance periods in days for the three basic orbits ORB1, ORB2, and ORB3.

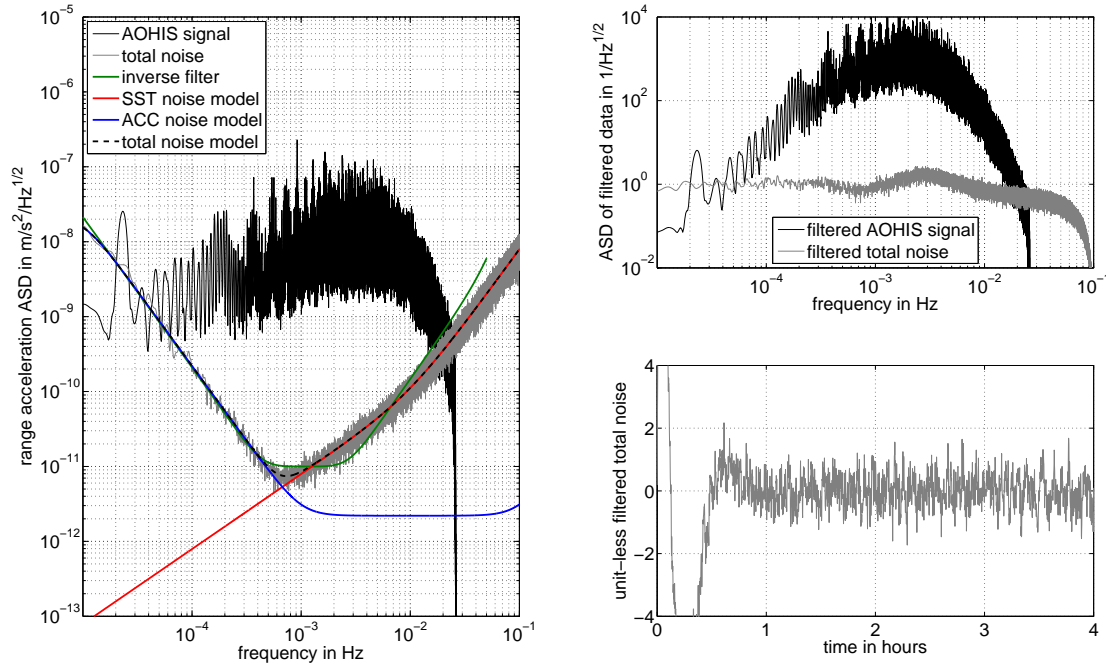


Figure 8.2: Signal, noise and filter application in the spectral and time domain for ORB1p. Left: range acceleration ASD in  $m/s^2/\sqrt{Hz}$  for the AOHIS low-low SST observations (black), the total noise (gray), the inverse frequency response of the ARMA filter (green) and the noise models. Top right: ASD of filtered AOHIS signal and total noise in  $1/\sqrt{Hz}$ . Bottom right: unit-less filtered total noise time series.

(cf. Fig. 4.5 and Tab. 4.3). Fig. 8.2 (left) shows the ASD of the total noise (gray) together with the AOHIS low-low SST signal on ORB1p ( $l_{max} = 80$ , black), the noise models, and the inverse frequency response of the ARMA filter (green) to be applied in Eq. (2.21). The total noise model (black dashed) consists of the laser ranging instrument or SST (red) noise and the accelerometer (ACC, blue) noise. The orbital frequency  $f_0$  is approximately  $1.8 \cdot 10^{-4}$  Hz for the three scenarios according to revolution times of 5,438 s for ORB1p, 5,517 s for ORB2p, and 5,586 s for ORB3p. The respective inclined orbits have a revolution time that is shorter by 41 s.

For the filters of all three scenarios a 2<sup>nd</sup> order Butterworth bandpass filter (maximally flat in pass and stop band) is used, for ORB1 with a pass band at  $0.4 < f < 3$  mHz. The inverse frequency response approximates the total noise ASD with small deviations above 1 mHz. Adequate filtering of the noise time series with this Butterworth filter results in a rather flat filtered spectrum (cf. Fig. 8.2, top right). As in Eq. (2.21) the observations consisting of signal and noise are filtered, the filtered AOHIS signal is also shown (black). Furthermore it is important to take warming up effects of such filters into account. This warm-up effect can be seen in Fig. 8.2 (bottom right) prominently within the first hour of the filtered noise time series. Therefore for all scenarios the first 1,500 epochs (approximately 2 hours) are not used for setting up the normal equation system. A digital filter in general does not only change the amplitudes but also the phases. But in Eq. (2.21) the filter is applied in both forward and reverse directions which is why the phase remains unchanged.

A graphical 3D representation of the orbit configuration is given in Fig. 8.3 for ORB1p (blue) and ORB1i (red) after 1 and 6 days. After 1 and 6 days, respectively, a nearly homogeneous groundtrack pattern is reached. After one day the polar and inclined orbit reach nearly 16 revolutions leading to mean gaps around the equator of 1,300 km (ascending and descending tracks), respectively. After 6 days the mean gaps are decreased to nearly 200 km for one orbit and 100 km for the double orbit.

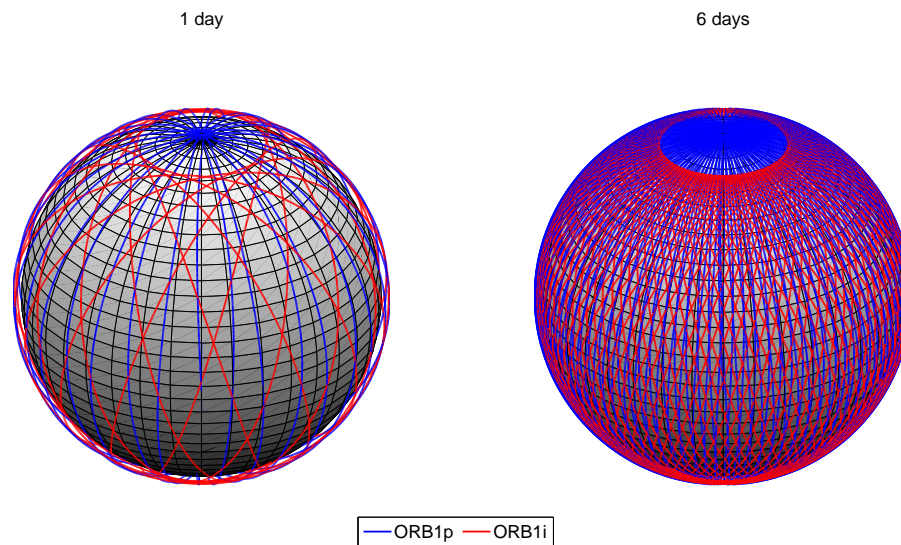


Figure 8.3: 3D orbit positions of ORB1p and ORB1i after 1 day (left) and 6 days (right).

## 8.1 Low Resolution Gravity Retrieval

In this section the results of low resolution gravity retrievals based on LCLA simulations up to  $l_{\max} = 80$  are discussed. The scenarios are the 3 single polar pairs ORB1p, ORB2p, and ORB3p, the 9 different double pairs with these polar pairs, and the 3 single inclined pairs ORB1i, ORB2i, and ORB3i (cf. Tab. 4.1). The key parameter to be analyzed is the effect of temporal aliasing from non-tidal and tidal sources on each scenario. The signal to be observed with each scenario is the mean AOHIS signal. Therefore the residuals wrt. this mean signal represents the real errors. No de-aliasing approach is applied for AOHIS, which means that the full content of the high-frequency variations (mainly AO) aliases into the solutions. For the ocean tide part de-aliasing is applied by using the difference between EOT08a and FES2004 as ocean tide input for the LCLA. The results are shown in the spectral and spatial domain.

### 8.1.1 Temporal Aliasing from Non-Tidal Variations

At first non-tidal aliasing is addressed and Fig. 8.4 shows the residuals wrt. the mean AOHIS for the 3 single pairs and the 9 double pairs in terms of unit-less SH coefficients ( $\log_{10}$ ), respectively. Resonances are visible for the single pairs (top row) in terms of high residuals around specific SH order bands. These resonances are reduced for the double pair residuals, but especially the double pairs with ORB3p (right column) suffer from the resonances. This effect is even enhanced because of the higher orbital altitude of ORB3. All scenarios show small residuals around the zonal coefficients ( $m = 0$ ), but for the zonals the single pairs are even more sensitive than the double pairs. And the double pair residuals have less variability with SH order.

Figures 8.5 and 8.6 show the corresponding SH degree and order amplitudes of the residuals in mm geoid height in comparison with the mean AOHIS signal (black) and the formal errors (dashed curves). The formal errors represent the performance level of each scenario in a static simulation case. It can be seen that the temporal aliasing effects due to the high-frequency AOHIS variations are around 2 orders of magnitude larger than the formal errors. This means that the high-frequency variations have to be reduced to be able to benefit from the sensitive instruments. This issue is discussed in Sec. 8.2.

The effects of the SH order resonances can be seen (Fig. 8.6). Especially for the single pairs the resonances lead to step-wise increases of the SH degree amplitudes for  $l = m_r$ . These steps reach one

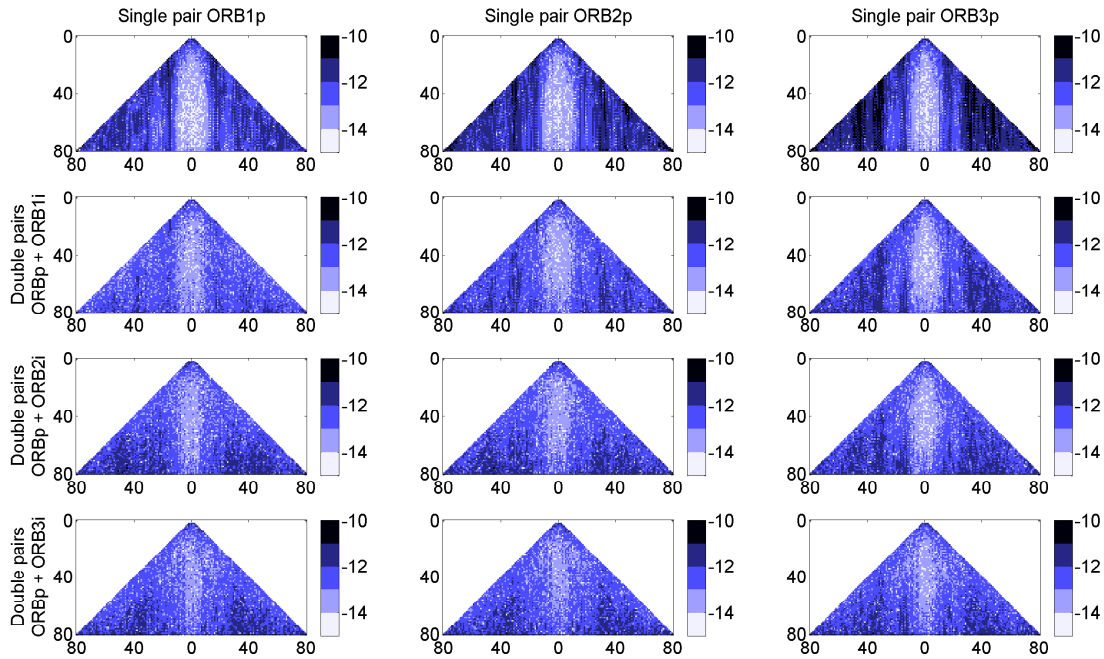


Figure 8.4: Non-tidal temporal aliasing: residuals of the full AOHIS analyses wrt. the mean AOHIS for the 3 single pairs (top row) and the 9 double pairs in terms of fully normalized unit-less SH coefficients ( $\log_{10}$ ) up to  $l_{\max} = 80$ , respectively. The second row contains the double pair residuals of ORB1p (left), ORB2p (center), and ORB3p (right) with ORB1i, respectively. The two bottom rows display the residuals analogously for the combinations with ORB2i and ORB3i.

order of magnitude for  $l = 15$  for all three single pairs and nearly one order of magnitude for  $l = 30$  for ORB3p. The SH degree amplitudes for the double pairs stay below the mean AOHIS signal up to SH degrees between 57 (ORB3p + ORB1i) and 78 (ORB1p + ORB1i). This means that the scenarios are able to observe the mean AOHIS signal on global average significantly with a spatial resolution of 350 and 260 km, respectively.

The spatial distribution of the residuals representing non-tidal temporal aliasing effects is displayed in Fig. 8.7 in terms of global geoid heights in mm. The single pair solutions (top row) show strong striping patterns with amplitudes of more than 20 mm geoid height for ORB3p. These errors are significantly reduced for all 9 double pair cases. The double pair residuals are dominated by systematic errors up to 5 mm geoid height in areas with high temporal AOHIS (mainly AO) variations around  $\pm 60^\circ$  latitude.

The lowest double pair scenario with ORB1p and ORB1i has the smallest residuals, and any combination of ORB1p and ORB2p with ORB1i and ORB3i is superior to the others. This becomes clearer when comparing the global RMS of these residuals in Tab. 8.1. The single pairs show a global RMS between 1 and 6 mm geoid height. The combination with the inclined pairs reduces the polar single pair RMS on average by a factor of 2 for ORB1p, 4 for ORB2p, and 9 for ORB3p. The double pair ORB1p + ORB1i has a global RMS of 0.3 mm.

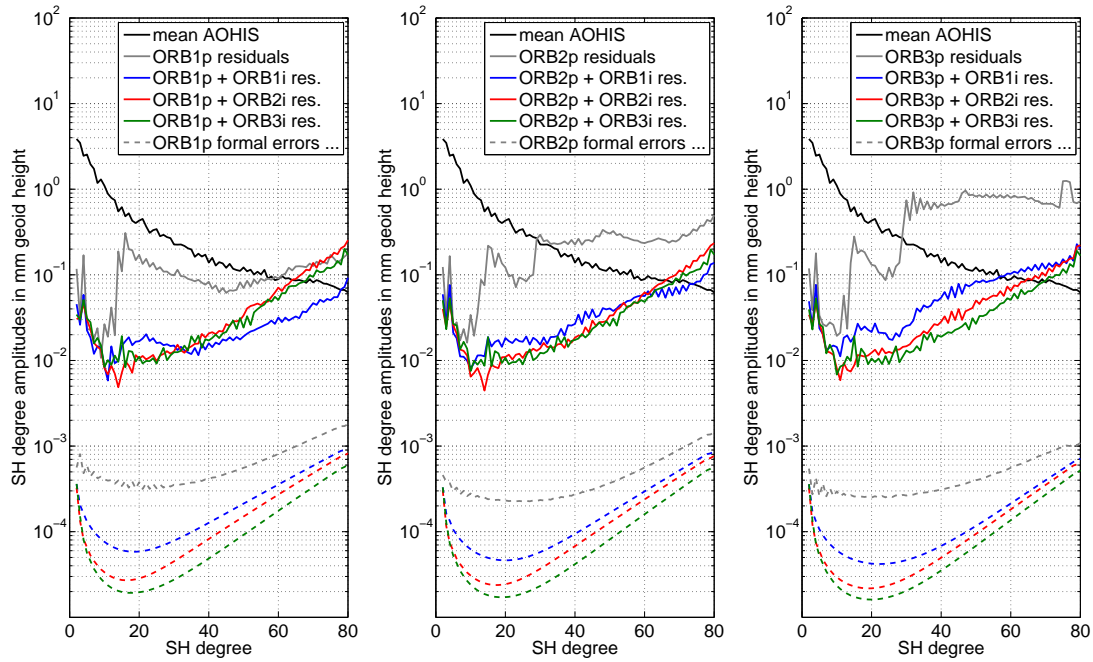


Figure 8.5: Non-tidal temporal aliasing: SH degree amplitudes in mm geoid height up to  $l_{\max} = 80$  of the full AOHIS analyses residuals wrt. the mean AOHIS for the 3 single pairs (gray) and the 9 double pairs in comparison with the mean AOHIS signal and the formal errors, respectively.

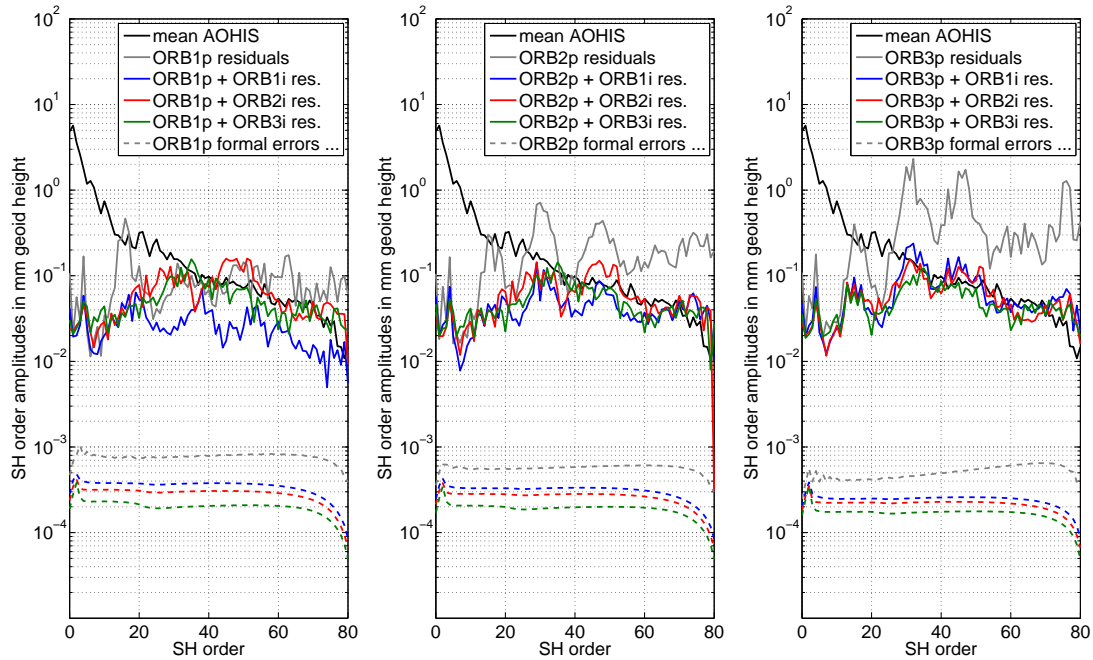


Figure 8.6: Non-tidal temporal aliasing: SH order amplitudes in mm geoid height up to  $l_{\max} = 80$  of the full AOHIS analyses residuals wrt. the mean AOHIS for the 3 single pairs (gray) and the 9 double pairs in comparison with the mean AOHIS signal and the formal errors, respectively.

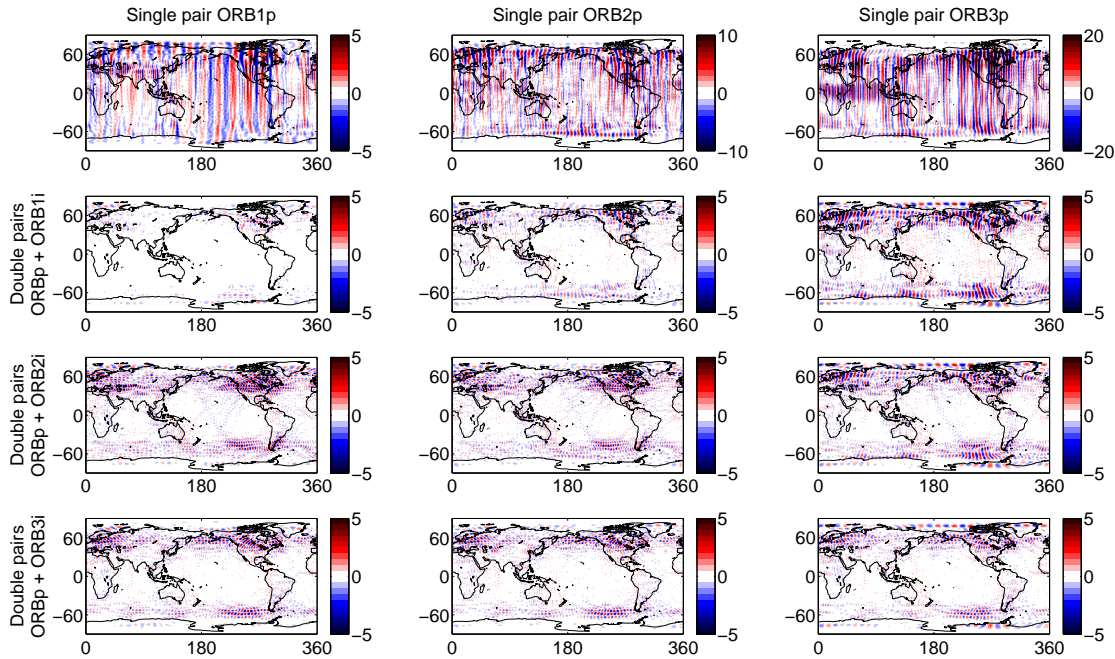


Figure 8.7: Non-tidal temporal aliasing: global geoid height residuals in mm computed on a  $1^\circ \times 1^\circ$  grid up to  $l_{\max} = 80$  of AOHIS wrt. the mean AOHIS for the 3 single pairs (top row) and the 9 double pairs, respectively. The second row contains the double pair residuals of ORB1p (left), ORB2p (center), and ORB3p (right) with ORB1i, respectively. The two bottom rows display the residuals analogously for the combinations with ORB2i and ORB3i. Note the different scales of the first row and the three bottom rows (double pair solutions).

### 8.1.2 Temporal Aliasing from Ocean Tides

In order to analyse the effects of temporal aliasing from ocean tides a de-aliasing approach is applied. The observations are computed from the mean AOHIS signal and the differences between the ocean tide models EOT08a and FES2004 (cf. Tab. 2.3). This ocean tide model difference (OTD) represents the model error assumption. The results are shown analogously to the figures in Sec. 8.1.1.

Figure 8.8 shows the SH spectrum of the residuals representing ocean tide temporal aliasing. Here the resonances are more prominently visible than for non-tidal aliasing (Sec. 8.1.1). The SH degree amplitudes (Fig. 8.9) show clearly the resonance at  $m = 47$  for ORB2p, and at  $m = 31$  for ORB3p. As in the non-tidal case (Fig. 8.5), the SH degree amplitudes of the ocean tide aliasing errors for double pairs are between 0.01 and 0.1 mm geoid height with minima around  $l = 40$ . For high SH degree in these analyses the ocean tide temporal aliasing is smaller than the non-tidal temporal aliasing. This also holds for the SH order amplitudes in Fig. 8.10, and as in the non-tidal case the smallest residuals

Table 8.1: Global geoid height residual RMS (weighted with cosine of latitude) in mm for non-tidal (AOHIS, cf. Fig. 8.7) and tidal (residual ocean tides, cf. Fig. 8.11) aliasing for the 3 single pairs and the 9 double pairs, respectively.

	AOHIS aliasing			Residual ocean tide aliasing		
	ORB1p	ORB2p	ORB3p	ORB1p	ORB2p	ORB3p
	1.0	2.1	5.7	0.43	1.5	6.1
ORB1i	0.27	0.44	0.75	0.24	0.37	0.75
ORB2i	0.68	0.63	0.62	0.34	0.36	0.56
ORB3i	0.54	0.52	0.49	0.67	0.66	0.85

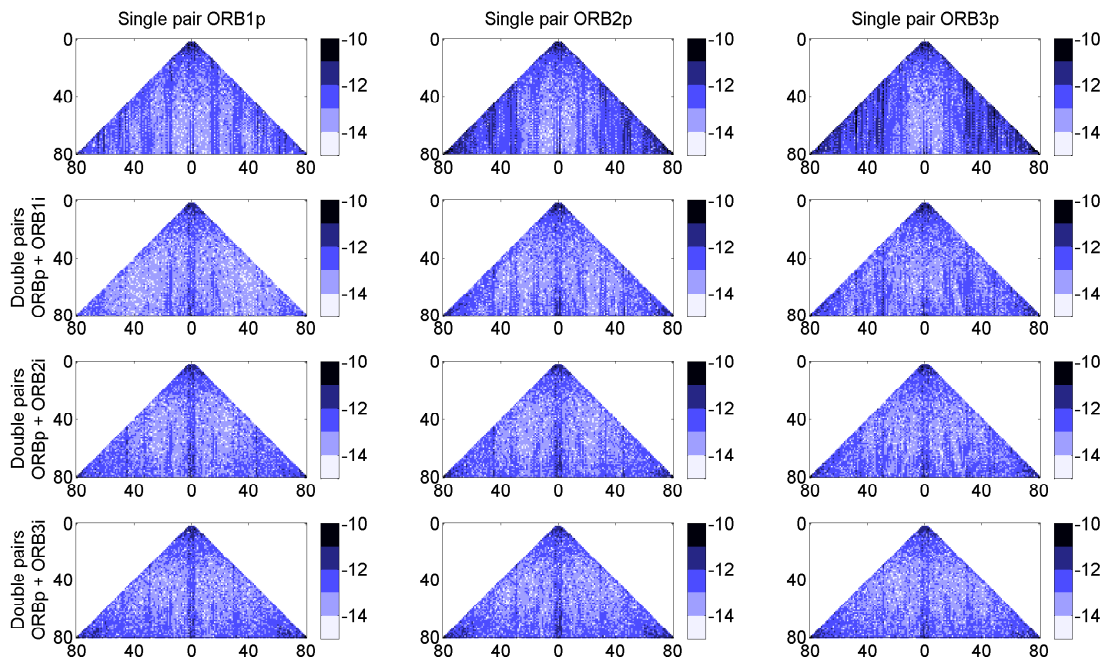


Figure 8.8: Ocean tide temporal aliasing: residuals of the OTD (EOT08a – FES2004) analyses wrt. the mean AOHIS for the 3 single pairs (top row) and the 9 double pairs in terms of fully normalized unit-less SH coefficients ( $\log_{10}$ ) up to  $l_{\max} = 80$ , respectively. The second row contains the double pair residuals of ORB1p (left), ORB2p (center), and ORB3p (right) with ORB1i, respectively. The two bottom rows display the residuals analogously for the combinations with ORB2i and ORB3i.

are given by ORB1p + ORB1i.

The global geoid height residuals (Fig. 8.11) are dominated by the resonance effects, especially by the  $m = 79$  resonance. This resonance effect results in a narrow band around the equator with high residuals of more than 20 mm geoid height for ORB3p and up to 5 mm for the double pairs with ORB3p and ORB3i. The single polar pair ORB1p gives even smaller residuals and a smaller global RMS (Tab. 8.1) than its combination with ORB3i. In comparison with the non-tidal temporal aliasing effects (Sec. 8.1.1) the average improvement of the single polar pair solutions by combinations with the inclined pairs is smaller for the ocean tide aliasing case.

In comparison with an in-line pair a Pendulum pair improves the observation geometry by adding more cross-track information to the inter-satellite range measurements. Figure 8.12 shows the reduction of the temporal aliasing effects from AOHIS and OTD in comparison with the corresponding in-line pairs for this formation in terms of SH degree amplitudes for the three scenarios ORB1p, ORB2p, and ORB3p.

For all these Pendulum results the zonal coefficients for  $l \in \{2, 4, 6\}$  have been excluded. This is because the low degree zonals of the Pendulum solutions have very large residuals and formal errors (cf. Fig. 4.2). As this effect is included in the formal errors as well, it is related to the observation geometry (in combination with the weight matrix). The pendulum solutions could be stabilized in the low degrees, for example, by combining low-low and high-low SST. By excluding these three coefficients from the residuals, the Pendulum results must be considered as optimistic for the low degrees.

In comparison with the in-line pairs the Pendulum pairs reduce the SH degree amplitudes of the residuals wrt. the mean AOHIS signal by a factor of 2 to 3. For these tidal and non-tidal results up to  $l_{\max} = 80$  the Pendulum pairs show comparable AOHIS retrieval performance to the average Bender-type double pair solutions (cf. Figs. 8.5 and 8.9). The scenario with the smallest residual of all the simulations in this section outperforms the Pendulum scenarios approximately by a factor of 2 for tidal aliasing and by a factor of 3 for non-tidal aliasing.

Together with Sec. 8.1.1 this section gives important information for the selection of the mission scenarios

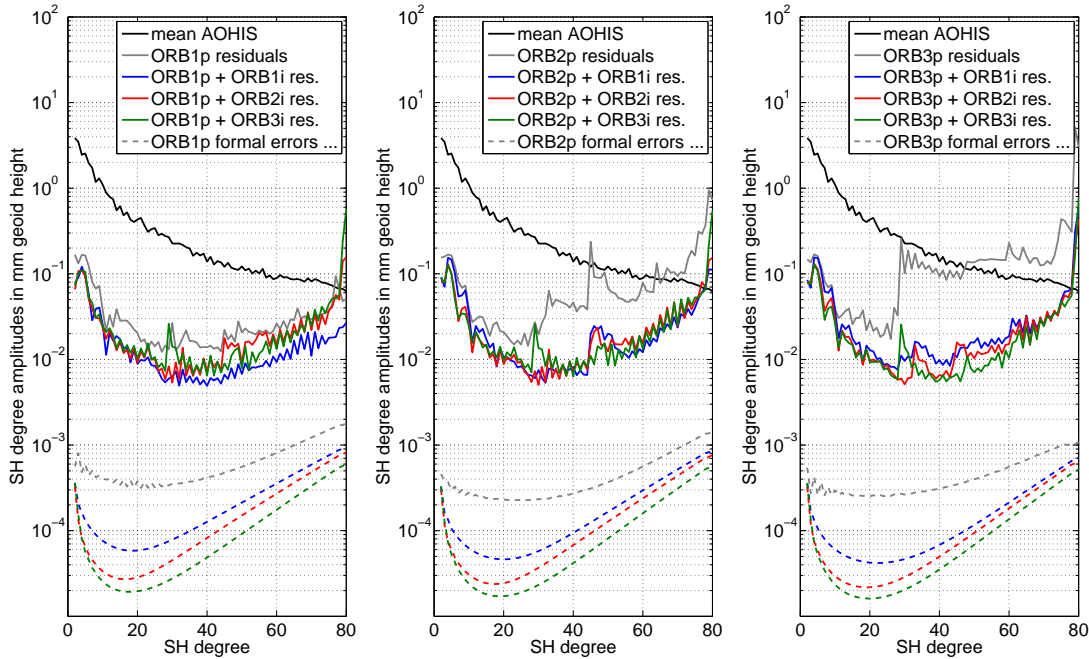


Figure 8.9: Ocean tide temporal aliasing: SH degree amplitudes in mm geoid height up to  $l_{\max} = 80$  of the OTD (EOT08a – FES2004) analyses residuals wrt. the mean AOHIS for the 3 single pairs (gray) and the 9 double pairs in comparison with the mean AOHIS signal and the formal errors, respectively.

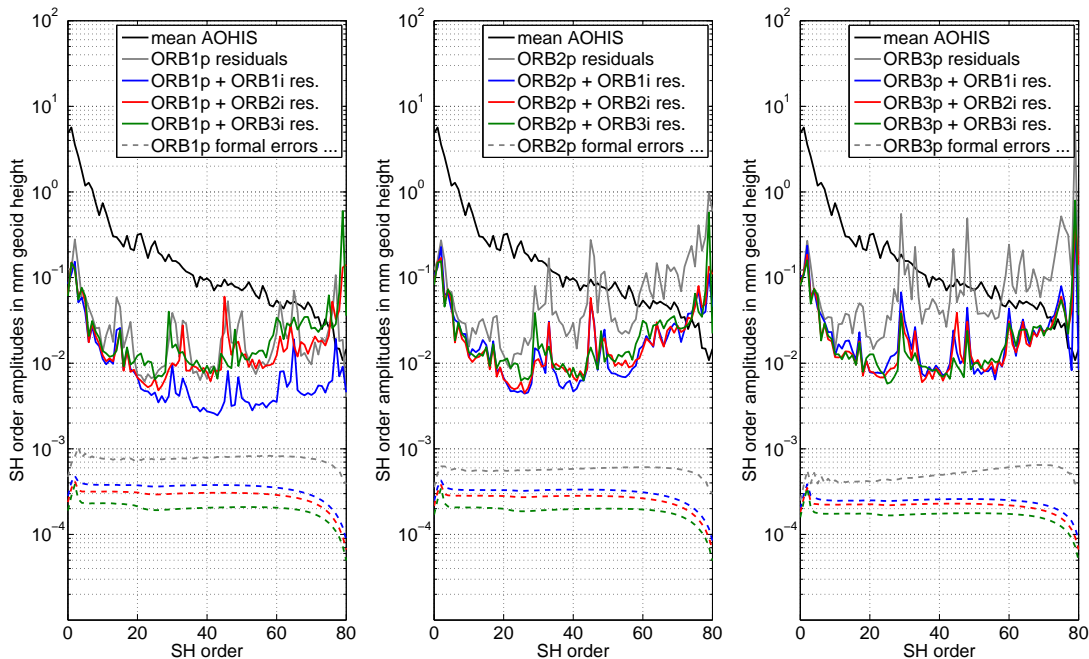


Figure 8.10: Ocean tide temporal aliasing: SH order amplitudes in mm geoid height up to  $l_{\max} = 80$  of the OTD (EOT08a – FES2004) analyses residuals wrt. the mean AOHIS for the 3 single pairs (gray) and the 9 double pairs in comparison with the mean AOHIS signal and the formal errors, respectively.

for the NGGM and for the issue of temporal aliasing from tidal and non-tidal sources. For these low resolution results ( $l_{\max} = 80$ ) the single polar pair ORB3p and double pairs including ORB3p and ORB3i give the worst mean AOHIS retrieval performance. Of course this sequence may look different for high resolution retrievals. The effects of the large SH order resonance of ORB1p at  $m = 95$  (cf. Fig. 8.1) is not visible in the results in this section.

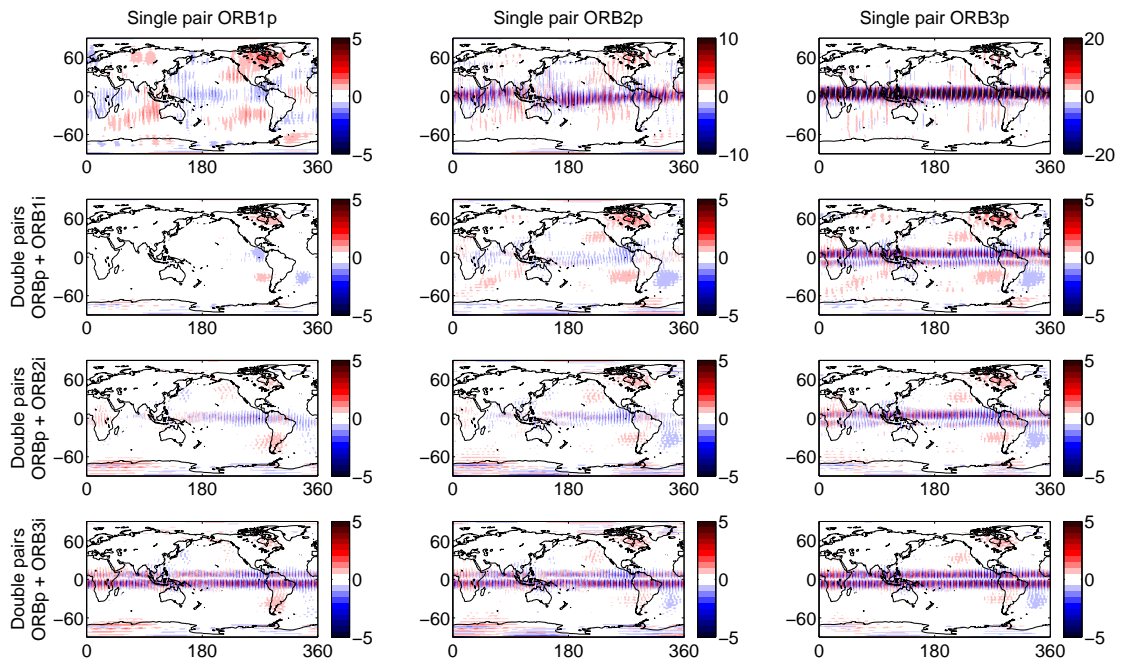


Figure 8.11: Ocean tide temporal aliasing: global geoid height residuals in mm computed on a  $1^\circ \times 1^\circ$  grid up to  $l_{\max} = 80$  of OTD (EOT08a – FES2004) wrt. the mean AOHIS for the 3 single pairs (top row) and the 9 double pairs, respectively. The second row contains the double pair residuals of ORB1p (left), ORB2p (center), and ORB3p (right) with ORB1i, respectively. The two bottom rows display the residuals analogously for the combinations with ORB2i and ORB3i. Note the different scales of the first row and the three bottom rows (double pair solutions).

The NGGM does not benefit from the required accurate instruments in the case of temporal aliasing from full AOHIS variations and ocean tide de-aliasing with an accuracy similar to the difference between EOT08a and FES2004. In order to fulfil the mission objectives the reduction of these variations is required. In Wiese et al. (2011) it is described how temporal aliasing can be reduced by estimating low resolution gravity fields with high temporal resolution in addition to one high resolution gravity for the whole observation period. Based on this method in Sec. 8.2 this procedure is discussed for the NGGM and the gain of temporal aliasing reduction is estimated.

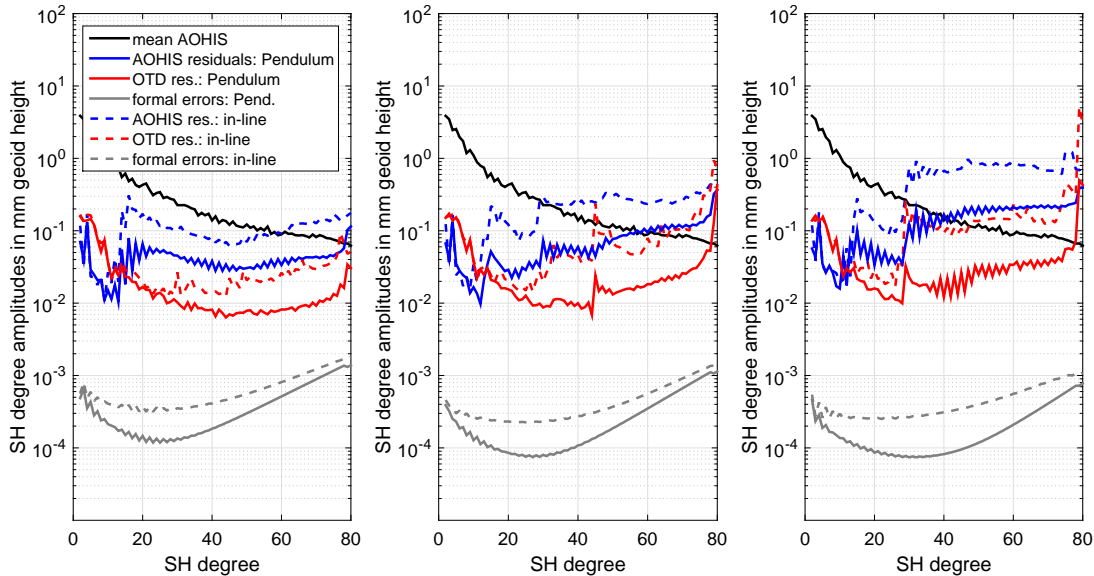


Figure 8.12: SH degree amplitudes in mm geoid height up to  $l_{\max} = 80$  of the residuals of the AOHIS and the OTD (EOT08a – FES2004) analyses wrt. the mean AOHIS for the polar Pendulum pairs in comparison with the mean AOHIS signal, the polar in-line pair residuals and the formal errors, respectively. From left to right there are the results for ORB1p, ORB2p, and ORB3p. The zonal coefficients for  $l \in \{2, 4, 6\}$  have been excluded from the Pendulum results.

## 8.2 High Temporal Resolution Gravity Retrieval

High-frequency mass variations mainly in atmosphere and oceans lead to large temporal aliasing errors in monthly gravity field retrievals. In Sec. 8.1 it is shown for the basic scenarios that the errors from temporal aliasing from the full variations of AOHIS and the difference between two ocean tide models are around 2 orders of magnitude above the instrument noise of the NGGM. One possibility to reduce temporal aliasing errors is the estimation of short period low resolution gravity field parameters in addition to one set of high resolution gravity field parameters for the whole observation period (Wiese et al., 2011). In this section this method is discussed for the NGGM with respect to the short period gravity retrieval performance and the approximation of the reduction rate of non-tidal variations.

The largest temporal variations of non-tidal mass distributions have periods of several days (Fig. 6.7, right). Hence, estimating gravity fields every  $n_{\text{day}} \in \{0.5, 1, 2\}$  days provides a big advantage. A global gravity field is observed with high temporal resolution (although with low spatial resolution). Therefore the variations above the Nyquist period of  $2 \cdot n_{\text{day}}$  do not alias into the high resolution retrieval for the main observation period (31 days for the NGGM).

The short period gravity retrieval performance is estimated for the double low-low SST in-line pair ORB1p + ORB1i. In order to take different AOHIS variabilities during one month into account three different epochs during January 2005 are chosen for the initial epoch of the short periods. The 12 hour period starts at 1 January, the 1 day period at 10 January, and the 2 day period at 20 January. As each of ORB1p and ORB1i performs more than 15 revolutions per day after 12 hours the gravity field parameters are set to  $l_{\max} = 15$  (30 for 1 day and 60 for 2 days).

As for the simulations in Sec. 8.1 the low-low SST observations are computed from the AOHIS model with full variations and from the differences between the two ocean tide models EOT08a and FES2004 (cf. Tab. 2.3). Figure 8.13 shows the SH degree amplitudes of the residuals wrt. the mean AOHIS signal for the three short periods, separately for the contributions of AOHIS and of the ocean tide model difference (OTD). The residuals for all three periods are significantly below the mean AOHIS signals. Only OTD leads to residuals as big as the mean AOHIS signal around the resonance orders. The AOHIS aliasing does not show these resonances and the residuals stay below the mean AOHIS signal for all SH degrees.

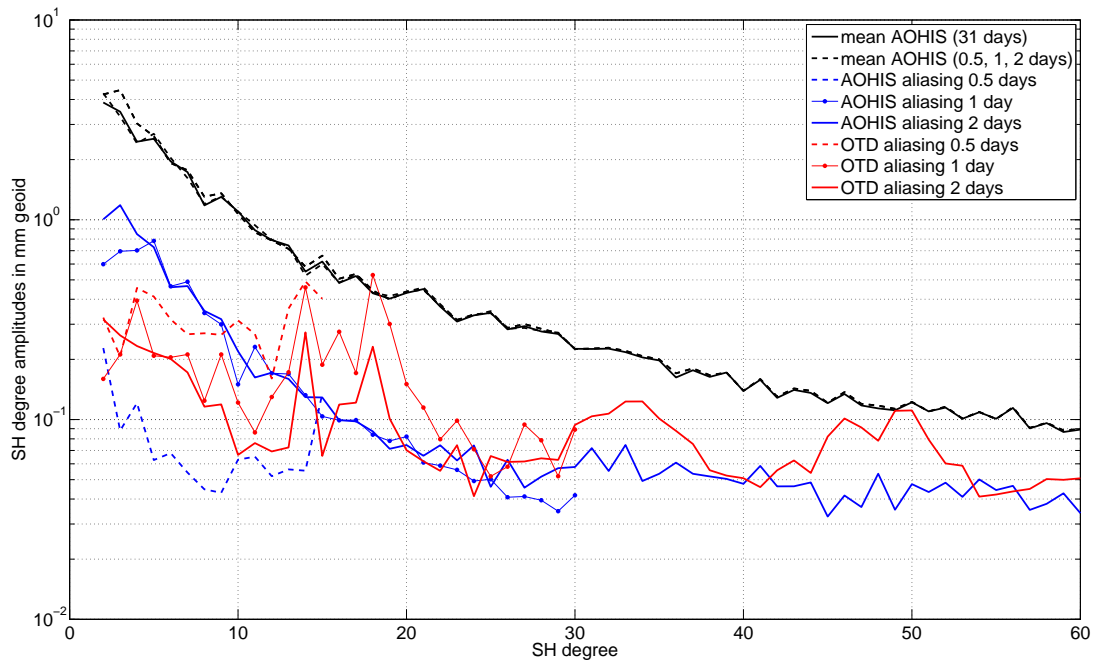


Figure 8.13: SH degree amplitudes in mm geoid height of the residuals of the AOHIS and the OTD (EOT08a – FES2004) analyses wrt. the mean AOHIS for the double pair ORB1p + ORB1i in comparison with the mean AOHIS signal for the three short periods of 0.5, 1, and 2 days.

In Fig. 8.14 the estimated mean gravity field (row 2) and the residuals for AOHIS (row 3) and OTD (row 4) is displayed in comparison with the mean AOHIS signal (row 1) in terms of global geoid heights computed up to the different  $l_{\max}$ . The mean AOHIS signal shows geoid heights of more than 50 mm for the areas with large hydrological variations, especially for the Congo region. It changes from 1 January (0.5 days period) to 10 January (1 day period) and 20 January (2 days period) with a global RMS of 3 and 4 mm (maximum geoid height changes of 15 and 25 mm), respectively.

The residuals for AOHIS and OTD are one order of magnitude smaller than the mean AOHIS signal. For the 0.5 days period the characteristic of the geoid height residuals are similar for AOHIS and OTD. A possible reason for this is spatial aliasing due to large gaps. It has to be analysed how the double pair orbit configuration, especially the ascending node separation, could be optimized in order to reduce spatial aliasing in this case. However, the effects are small compared to the mean AOHIS signal. For 1 and 2 days the geoid height residuals for AOHIS and OTD show the same behaviour as the monthly retrievals in Sec. 8.1 with lower spatial resolution (cf. Figs. 8.7 and 8.11).

The global RMS values of the geoid heights in Fig. 8.14 are given in Tab. 8.2. The residuals show global RMS values of around 1 mm and the mean AOHIS signals of around 8 mm. This confirms that a global gravity field can be observed in short periods of 0.5, 1, and 2 days. In the following it is discussed how this estimation reduces the temporal aliasing errors of the NGGM.

The main advantage of co-estimating short period gravity field parameters together with one set of high resolution gravity field parameters for the whole monthly period is temporal aliasing reduction. The signals above the Nyquist period of the short period estimates do not alias into the high resolution solution, because they are observed with high temporal resolution. This effect is analysed in Wiese et al. (2011) for a single polar pair and two double pairs. Without post-processing filtering but with AO de-aliasing the short period gravity estimates improve the results without additional short period gravity estimates approximately by a factor of 2. However, Wiese et al. (2011) estimate the smallest improvements for the Bender-type double pair. This improvement rate agrees with the results of the following assessment for the estimation of 0.5, 1, and 2 days gravity retrievals.

Analogously to Fig. 6.7 the amplitudes of the non-tidal AOHIS variations are shown in Fig. 8.15 de-

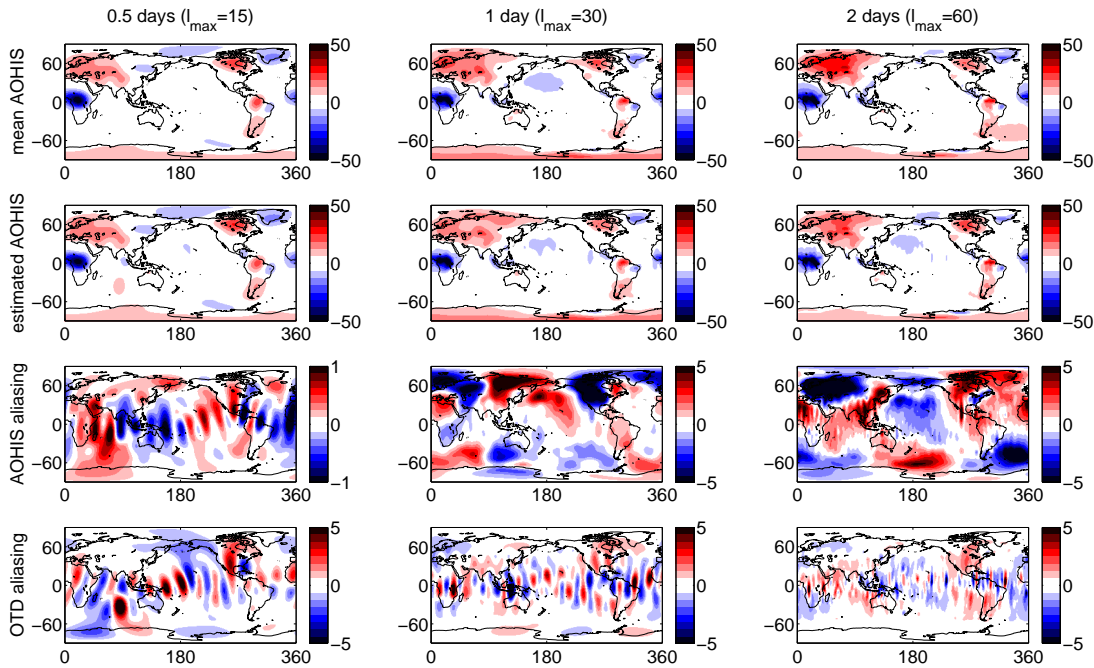


Figure 8.14: Global geoid heights in mm computed on a  $1^\circ \times 1^\circ$  grid of mean AOHIS, estimated AOHIS, and the residuals of OTD (EOT08a – FES2004) and AOHIS wrt. the mean AOHIS for the 3 short periods of 0.5 ( $l_{\max} = 15$ ), 1 ( $l_{\max} = 30$ ), and 2 ( $l_{\max} = 60$ ) days, respectively.

pending on the period between 0.5 and 30 days and on the SH degree  $0 \leq l \leq 100$ . The amplitudes for each period are computed from the Fourier series of the AOHIS time series for January 2005 (Gruber et al., 2011). The signals which are observed with the three short period retrievals are marked with blue boxes. Except for the AOHIS signals with periods below 1 day the largest amplitudes are covered by the three short period retrievals.

All AOHIS signal contents outside the blue boxes in Fig. 8.15 alias into the monthly high resolution solution. By summing up the total RMS for each period the total temporal aliasing error RMS of AOHIS can be estimated. This is done for  $2 \leq l \leq 140$  for the three short periods separately and for the combination of the three short periods. Figure 8.16 shows the cumulative geoid heights over the periods of the total AOHIS variations (gray) in comparison with the variations without the 4 short period cases (blue) and the reduction (red).

As the short period estimates reduce the AOHIS signal contents with the largest amplitudes the RMS of the reduced variations shows no significant increase above each Nyquist period. Especially the signal contents with periods larger than 3 days and amplitudes larger than 0.1 mm are observed (cf. Fig. 8.15). The total RMS of the AOHIS variations (gray) for this month sums up to 2.3 mm geoid height. With the combined short period retrievals (0.5, 1, and 2 days) the RMS for this month is reduced to 1 mm.

Table 8.2: Global geoid height RMS (weighted with cosine of latitude) in mm for the mean AOHIS signal and for the non-tidal (AOHIS) and tidal (OTD) residuals for the double pair ORB1p + ORB1i for 0.5, 1, and 2 days periods, respectively (cf. Fig. 8.14).

Period in days	0.5 ( $l_{\max} = 15$ )	1 ( $l_{\max} = 30$ )	2 ( $l_{\max} = 60$ )
mean AOHIS signal	7.0	7.6	8.4
AOHIS residuals	0.35	1.7	2.1
OTD residuals	1.3	1.1	0.89

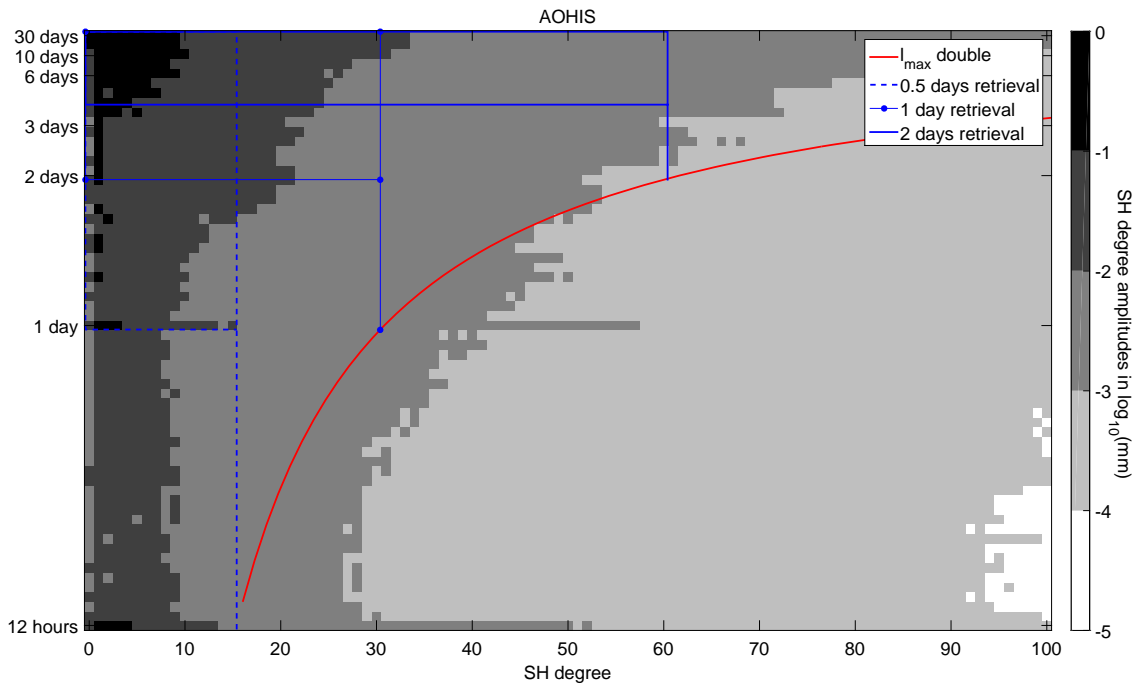


Figure 8.15: SH degree amplitudes in  $\log_{10}$  (mm) geoid heights of non-tidal AOHIS variations depending on the period in days. The amplitudes for different periods are computed from the Fourier series of the AOHIS time series for January 2005 from Gruber et al. (2011). The red line represents the maximum possible SH degree of expansion for a double pair. The blue lines mark the amplitudes which are observed with the three short periods of 0.5, 1, and 2 days, respectively. With the 1 day retrieval, for example, the signals above the Nyquist period of 2 days are observed up to  $l_{\max} = 30$ .

This analysis applies only for AOHIS and not for ocean tides. But as Wiese et al. (2011) include ocean tide de-aliasing errors in the analyses, and a similar reduction is shown, it can be assumed for the ocean tide aliasing reduction as well.

The largest part is reduced already with the 12 hours estimates. Therefore it is recommended to take this period into account for the NGGM. As described above, the orbit configuration of the double pair has to be optimized wrt. optimal sampling in each 12 hours in order to avoid spatial aliasing and to increase the spatial resolution. The main conclusions of this section are used for the discussions of the final high resolution results in Secs. 8.3 and 8.4.

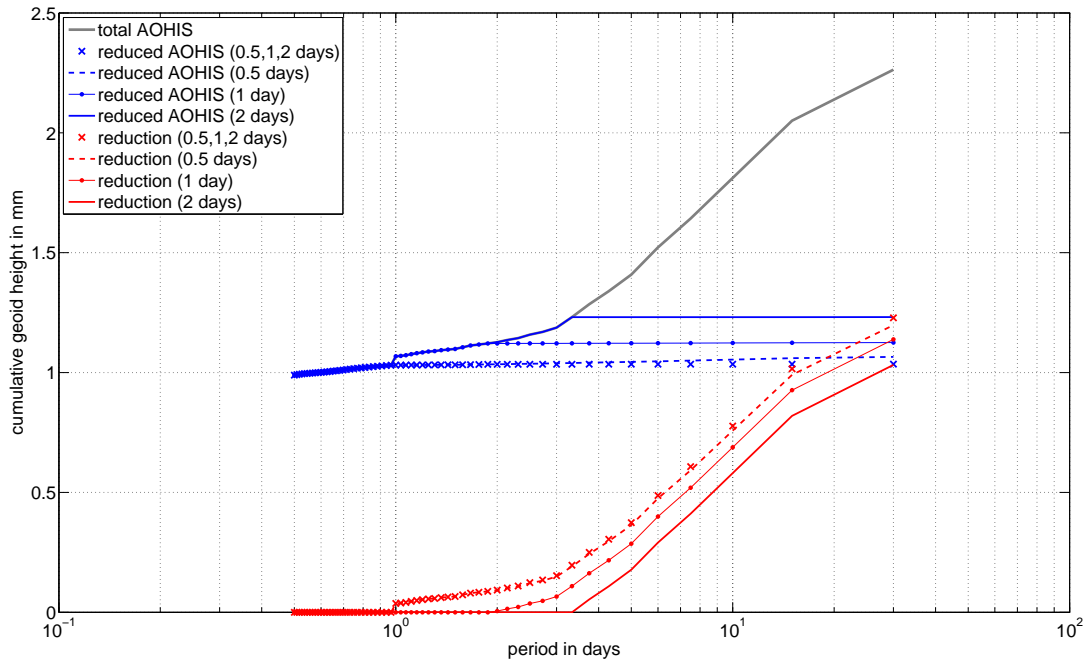


Figure 8.16: Cumulative geoid heights in mm over the periods of the total AOHIS variations (gray) in comparison with the variations without the 3 short period retrievals separately and without the combination of the three short period retrievals, respectively. The geoid heights are computed from the total RMS for each period of AOHIS for  $2 \leq l \leq 140$  with and without the blue boxes in Fig. 8.15. The red curves represent the reduction of AOHIS variations with each of the 4 short period cases.

### 8.3 High Spatial Resolution Gravity Retrieval

In this section the results of gravity retrievals with high spatial resolution ( $l_{\max} = 140$ ) are assessed and discussed. This spatial resolution is sufficient for the comparison of these final results with the mission objectives. The results are presented analogously to the low resolution results in Sec. 8.1. The simulation scheme is given in Fig. 2.4. As static gravity field model GOCO02S (second release of Pail et al. (2010)) and as non-tidal variations AOHIS (Gruber et al., 2011) is chosen. The ocean tide aliasing effects are not assessed with high resolution. The low resolution results in Sec. 8.1 are used for the discussion.

The best gravity retrieval results in Sec. 8.1 are reached for the double low-low SST pairs combining the observations of a polar and a  $70^\circ$  inclined pair. The double pairs consist of pairs of the basic scenarios (Tab. 4.1). As observation noise the same data is used as described in Sec. 8.1 (cf. Fig. 8.2).

At first a static simulation is discussed for the single polar pair ORB1p and the double pair ORB1p + ORB1i. Figure 8.17 shows the static residuals of these two scenarios in terms of SH degree amplitudes (left) and in terms of global geoid heights (right). The SH degree amplitudes of the residuals show good agreement with the formal errors. This shows, that the observations are weighted correctly with the ARMA filter according to the colored noise. The small deviations between the slopes of the formal errors compared to the static residuals for high SH degrees for the single and double pair are due to the different slopes of the inverse frequency response of the filter compared to the noise ASD for high frequencies (cf. Fig. 8.2).

The spatial distribution of the static geoid height residuals computed up to  $l_{\max} = 134$  (corresponding to a spatial resolution of 150 km) does not show systematic effects (Fig. 8.17, right). The absolute maximum residuals are 0.35 mm for the single, and 0.17 mm for the double pair. The global RMS of the double pair residuals is smaller than a factor of 2 as well ( $34 \mu\text{m}$  for double, and  $72 \mu\text{m}$  for single). Furthermore, the double pair residuals show the impact of the inclined pair. The residuals at latitudes  $\phi$  with only polar pair observations ( $|\phi| > 70^\circ$ ) are higher than the residuals for  $|\phi| < 70^\circ$ .

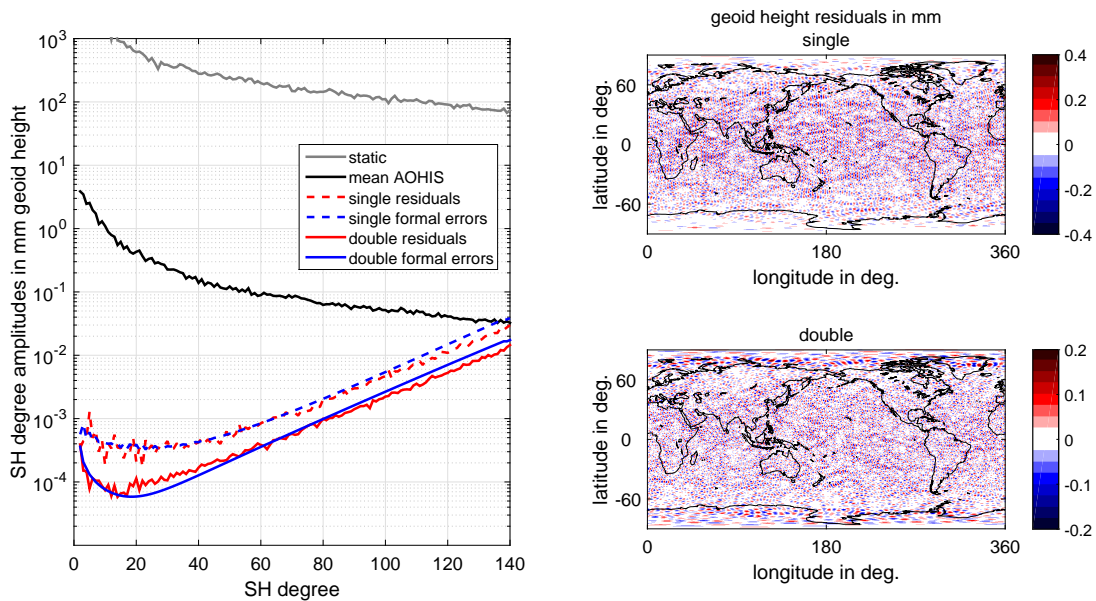


Figure 8.17: Left: SH degree amplitudes in mm geoid height up to  $l_{\max} = 140$  of the static residuals for the single polar pair ORB1p and the double pair ORB1p + ORB1i in comparison with the mean AOHIS signal and the formal errors. Right: global geoid heights in mm computed up to  $l_{\max} = 134$  on a  $0.5^\circ \times 0.5^\circ$  grid of the single (ORB1p, top) and double (ORB1p + ORB1i, bottom) pair residuals. Note the different range between the spatial geoid height residuals.

The high resolution AOHIS aliasing results are shown analogously to Fig. 8.5 in terms of SH degree amplitudes including instrument noise and temporal aliasing from full AOHIS. Figures 8.18, 8.19, and 8.20 display the results for the three single polar pairs ORB1p, ORB2p, and ORB3p and the corresponding double pairs combining the polar pair with the three  $70^\circ$  inclined pairs. As for the low resolution results the single pair residuals show strong resonance effects, especially at  $l = 15$ , whereas the double pair residuals are much smoother. For high SH degrees the combinations of ORB1p with ORB2i and ORB3i, respectively, do not improve the results of the single polar pair ORB1p (Fig. 8.18).

The residuals including full AOHIS aliasing are larger than the formal errors approximately by a factor of 100. For low SH degrees the resonances have more impact on the residuals, but towards  $l_{\max} = 140$  the impact of the orbital altitude increases. Hence, the residuals for all double pairs consisting of ORB1i (270 km altitude, blue lines) are smaller than the double pairs with ORB2i (330 km altitude, red lines), which are slightly smaller than the double pairs with ORB3i (390 km altitude, green lines).

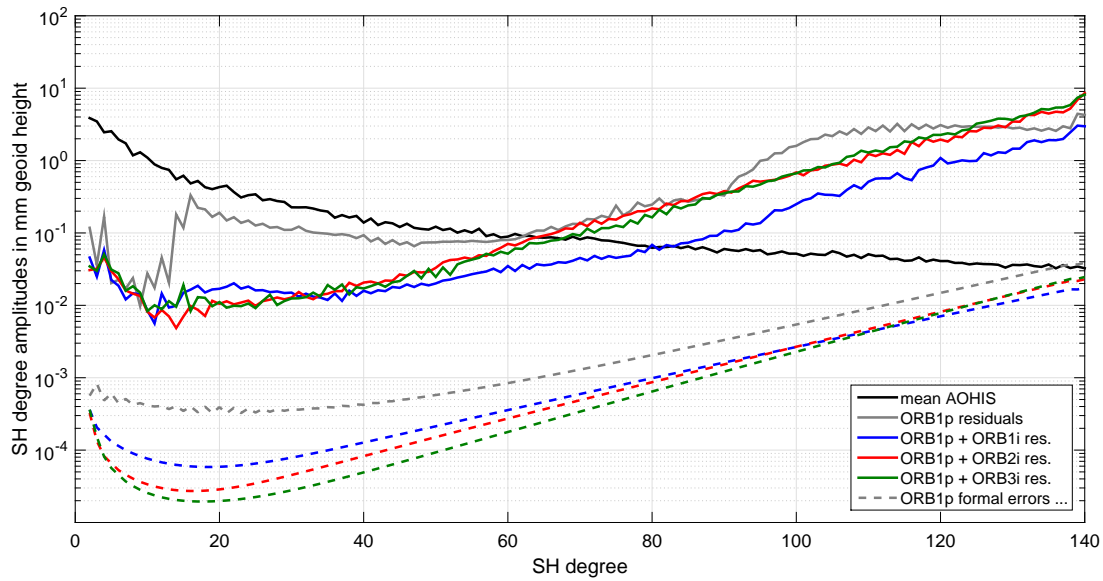


Figure 8.18: Non-tidal temporal aliasing: SH degree amplitudes in mm geoid height up to  $l_{\max} = 140$  of AOHIS residuals wrt. the mean AOHIS for the polar single pair ORB1p (gray) and the 3 double pairs with ORB1p in comparison with the mean AOHIS signal and the formal errors, respectively.

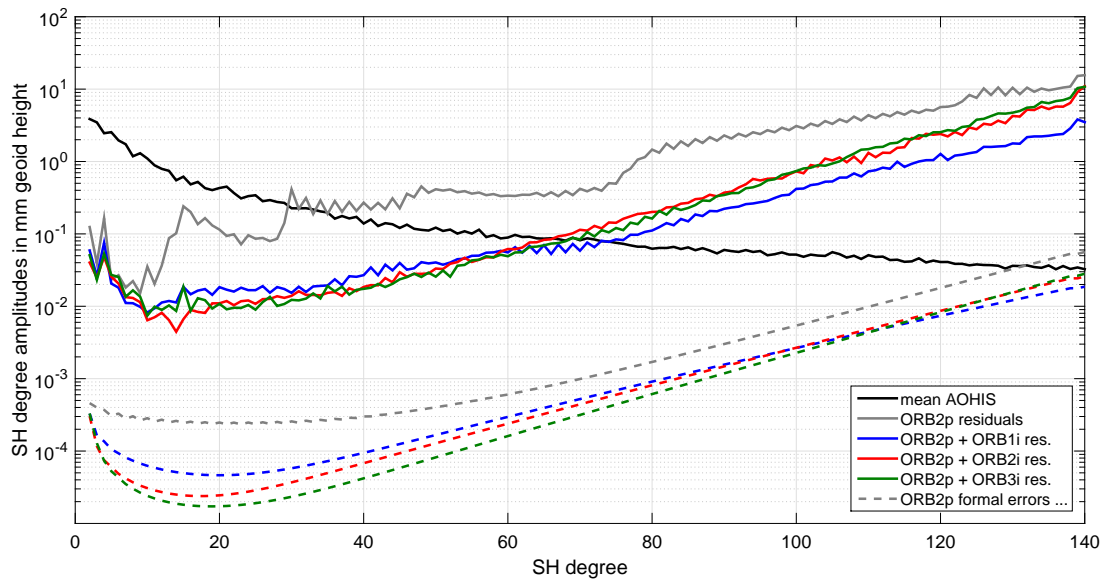


Figure 8.19: Non-tidal temporal aliasing: SH degree amplitudes in mm geoid height up to  $l_{\max} = 140$  of AOHIS residuals wrt. the mean AOHIS for the polar single pair ORB2p (gray) and the 3 double pairs with ORB2p in comparison with the mean AOHIS signal and the formal errors, respectively.

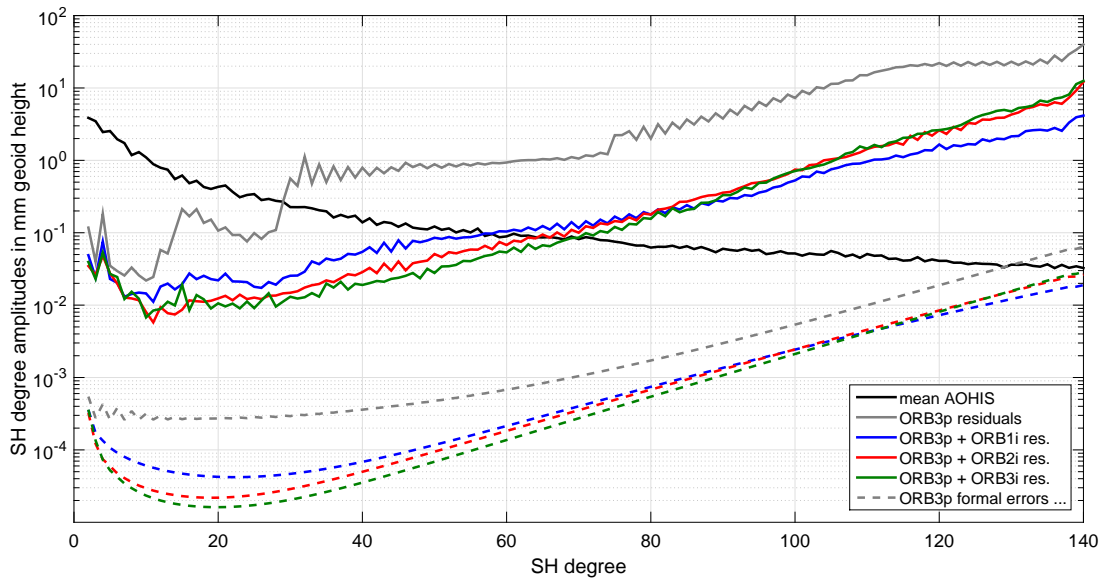


Figure 8.20: Non-tidal temporal aliasing: SH degree amplitudes in mm geoid height up to  $l_{\max} = 140$  of AOHIS residuals wrt. the mean AOHIS for the polar single pair ORB3p (gray) and the 3 double pairs with ORB3p in comparison with the mean AOHIS signal and the formal errors, respectively.

## 8.4 Comparison with Mission Objectives

In this section the high resolution results are compared to mission objective MO2 with required global geoid accuracies of 0.01 mm for 500 km and of 0.4 mm for 150 km spatial resolution. In Sec. 4.2 it is explained that the instrument noise of the ranging instrument and the accelerometers accounts for 50% of these required geoid accuracies. As in the final simulations the total effect of instrument noise plus temporal aliasing is assessed, temporal aliasing must account for less than 50% of the requirements in order to fulfil MO2.

At first this is only applied to the non-tidal aliasing contributions and the required geoid accuracy of the final AOHIS simulations is  $5 \mu\text{m}$  at  $l = 40$  (500 km spatial resolution) and 0.2 mm at  $l = 134$  (150 km spatial resolution). The cumulative geoid errors representing global mean geoid errors depending on the SH degree are displayed for the basic scenarios in Figs. 8.21, 8.22, and 8.23 in comparison with the formal errors and the static residuals (without AOHIS aliasing).

In comparison with the SH degree amplitude plots in Sec. 8.3 they show a much smoother behaviour. As the amplitudes decrease for the very low SH degrees before they increase above approximately  $l = 10$ , the cumulative errors are flat for the low SH degrees. The cumulative geoid errors of the static residuals (black) are well represented by the cumulative formal errors. But the cumulative errors including the full AOHIS aliasing are two orders of magnitude above the formal errors.

On the basis of the cumulative geoid errors at  $l = 40$  and  $l = 134$  the comparison with MO2 is assessed. Table 8.3 shows the cumulative geoid errors for the 3 single and the 9 double pairs for the two spatial resolutions. As these errors are dominated by temporal aliasing from full AOHIS variations, a requirement for the reduction of these variations is formulated in order to reduce the AOHIS temporal aliasing errors to the in MO2 required values. This required reduction rate is given in brackets for each scenario and the two resolutions, respectively. This means that the cumulative geoid errors divided by the numbers in brackets give the requirements in MO2. The required reduction rates are larger for the high spatial resolution at 150 km. Therefore these rates for  $l = 134$  represent the NGGM requirements for the reduction of AOHIS variations.

The best scenarios with the smallest cumulative errors at  $l = 134$  and therefore the smallest required AOHIS reduction rate are the three double pairs consisting of the inclined pair in the lowest altitude

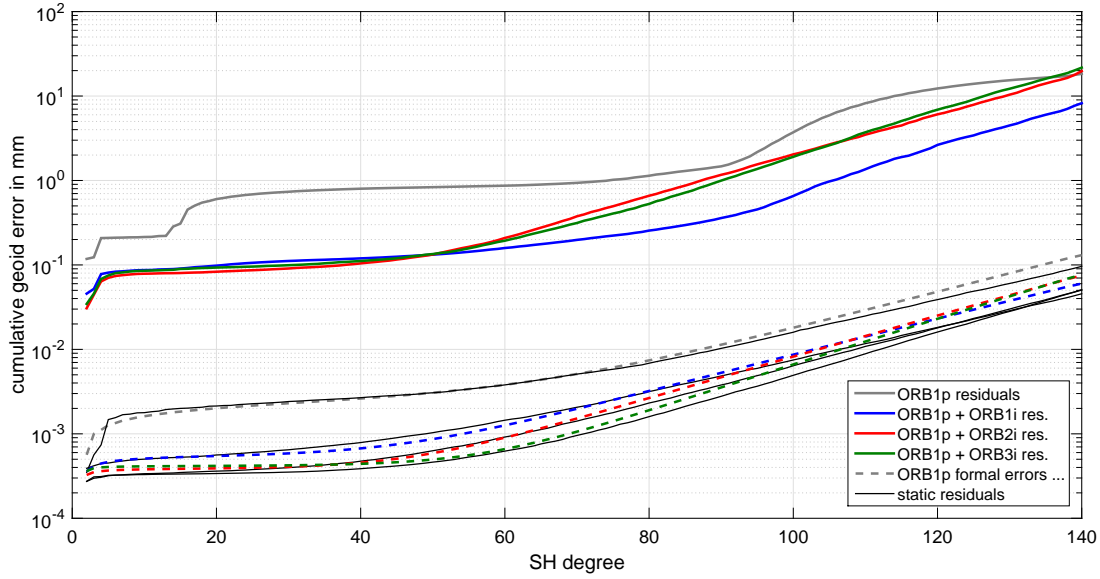


Figure 8.21: Cumulative geoid errors up to  $l_{\max} = 140$  of AOHIS residuals wrt. the mean AOHIS for the polar single pair ORB1p (gray) and the 3 double pairs with ORB1p in comparison with the formal errors and the static residuals (black), respectively.

ORB1i. How the required AOHIS reduction rates around 40 for these three scenarios can be achieved is discussed in Chap. 9. If this reduction is not achieved the signals of interest in the science requirements (Tab. 3.2) can only be measured with decreased resolution.

The global geoid height residuals wrt. mean AOHIS including full AOHIS temporal aliasing for the best single pair scenario (ORB1p) and three best double pair scenarios (double pairs including ORB1i) computed up to  $l_{\max} = 134$  are shown in Fig. 8.24. The global RMS of these grids is the same as the cumulative geoid errors for these scenarios given in Tab. 8.3. But the absolute geoid height residuals reach maximum values of around 10 cm for ORB1p (top left) and ORB3p + ORB1i (bottom right) and values around 6 cm for ORB1p + ORB1i (top right) and ORB2p + ORB1i (bottom left). Furthermore the residuals are not randomly distributed and show systematic effects. For the single pair these systematic effects are visible in a narrow North-South striping pattern with maximum values in latitude bands around  $\pm 40^\circ$ . This striping pattern is significantly reduced for the three double pairs but especially around  $40^\circ$  latitude it is still visible for all three double pairs.

As for ocean tides there are no high resolution results, the low resolution results in Sec. 8.1.2 are used

Table 8.3: Cumulative geoid error in mm including instrument errors and full AOHIS aliasing in mm together with the required reduction of the AOHIS variations (in brackets) in order to reach 50% of MO2 ( $5 \mu\text{m}$  at 500 km and 0.2 mm at 150 km). For example, the double pair ORB1p + ORB1i results in a cumulative geoid error of 5.7 mm at  $l = 134$ . This error is dominated by full AOHIS aliasing and therefore the AOHIS variations have to be reduced by a factor of 29 to reach 0.2 mm.

Spatial resolution	500 km ( $l_{\max} = 40$ )			150 km ( $l_{\max} = 134$ )		
	ORB1p	ORB2p	ORB3p	ORB1p	ORB2p	ORB3p
	0.80 (160)	1.1 (220)	2.4 (480)	16 (80)	39 (195)	110 (550)
ORB1i	0.12 (24)	0.14 (28)	0.19 (38)	5.7 (29)	7.3 (37)	9.0 (45)
ORB2i	0.10 (20)	0.10 (20)	0.12 (24)	13 (65)	16 (80)	17 (85)
ORB3i	0.11 (22)	0.11 (22)	0.11 (22)	15 (75)	18 (90)	19 (95)

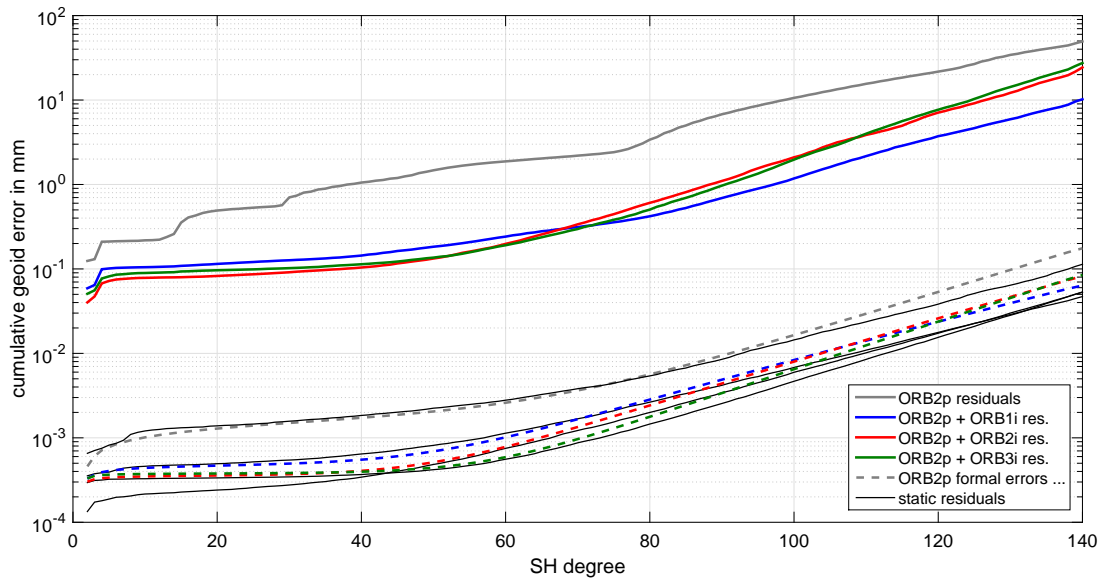


Figure 8.22: Cumulative geoid errors up to  $l_{\max} = 140$  of AOHIS residuals wrt. the mean AOHIS for the polar single pair ORB2p (gray) and the 3 double pairs with ORB2p in comparison with the formal errors and the static residuals (black), respectively.

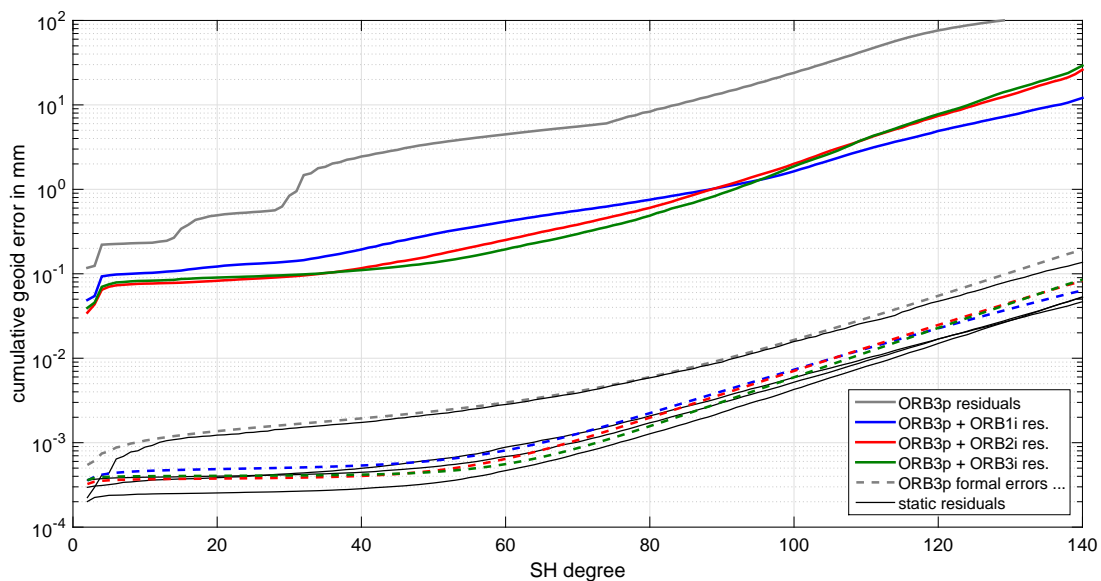


Figure 8.23: Cumulative geoid errors up to  $l_{\max} = 140$  of AOHIS residuals wrt. the mean AOHIS for the polar single pair ORB3p (gray) and the 3 double pairs with ORB3p in comparison with the formal errors and the static residuals (black), respectively.

for deriving the cumulative geoid errors displayed in Fig. 8.25 for all 3 single pairs and 9 double pairs, respectively. Two sets of cumulative geoid errors are shown in each plot. The full ocean tide aliasing geoid error contribution is derived from the full signal in EOT08a (dashed lines), and the residual signal as before is derived from the difference between EOT08a and FES2004 (solid lines). It can be seen that the residual ocean tide contribution is approximately one order of magnitude smaller than the full ocean tide contribution. The low SH degree residual content is larger than in the non-tidal case (cf. Fig. 8.9). Therefore the cumulative geoid errors are flat up to  $l = 60$  for the double pairs.

Analogously to the non-tidal case the cumulative geoid errors of the full and reduced ocean tide (OT) contributions at  $l = 40$  are compared with 50% of the required geoid accuracy in MO2 of  $5 \mu\text{m}$  (Tab. 8.4). Here the impact of the orbital altitude is smaller than for the high resolution non-tidal case and the

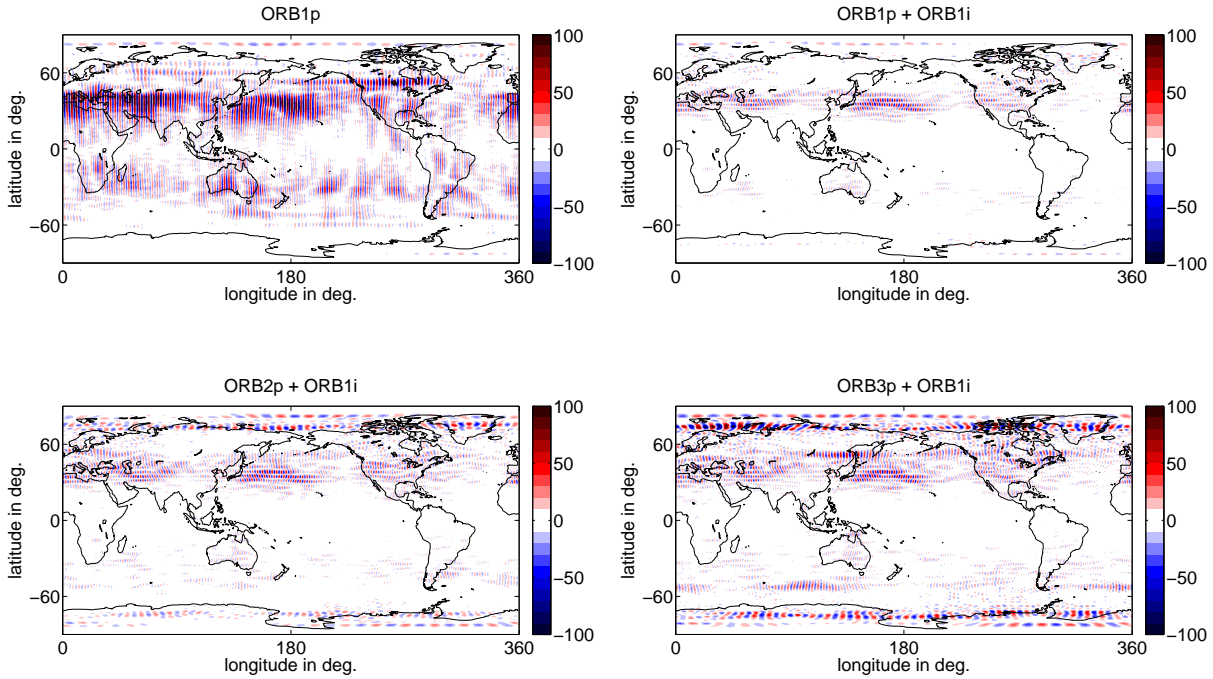


Figure 8.24: Global geoid height residuals in mm computed up to  $l_{\max} = 134$  on a  $0.5^\circ \times 0.5^\circ$  grid for the best single pair ORB1p (top left) and the three best double pairs ORB1p + ORB1i (top right), ORB2p + ORB1i (bottom left), and ORB3p + ORB1i (bottom right).

cumulative geoid errors for the double pairs in the reduced ocean tide case range only from 0.22 to 0.3 mm. The required reduction rate of the full and the reduced OT contribution is given in brackets, and for the reduced OT contribution it is around 50 and therefore in the same order of magnitude as the required AOHIS reduction rates.

The main error contribution for the NGGM is temporal aliasing from non-tidal (AOHIS) and tidal (OT) sources. The main results of this section are requirements for the reduction of the high-frequency signal contents in AOHIS and OT. In Chap. 9 these results are discussed also wrt. whether and how this reduction is achievable.

Table 8.4: Cumulative geoid error at  $l = 40$  due to full (EOT08a) and reduced (EOT08a – FES2004) ocean tide (OT) variations in mm together with the required OT reduction in brackets in order to fulfil the 50% geoid accuracy requirement of MO2 for 500 km ( $5 \mu\text{m}$ ).

	full OT			reduced OT		
	ORB1p	ORB2p	ORB3p	ORB1p	ORB2p	ORB3p
	3.8 (760)	4.5 (900)	4.8 (960)	0.38 (76)	0.41 (82)	0.63 (130)
ORB1i	3.0 (600)	2.6 (520)	2.8 (560)	0.22 (44)	0.29 (58)	0.30 (60)
ORB2i	3.5 (700)	2.9 (580)	3.0 (600)	0.22 (44)	0.23 (46)	0.24 (48)
ORB3i	3.4 (680)	2.8 (560)	2.9 (580)	0.23 (46)	0.23 (46)	0.23 (46)

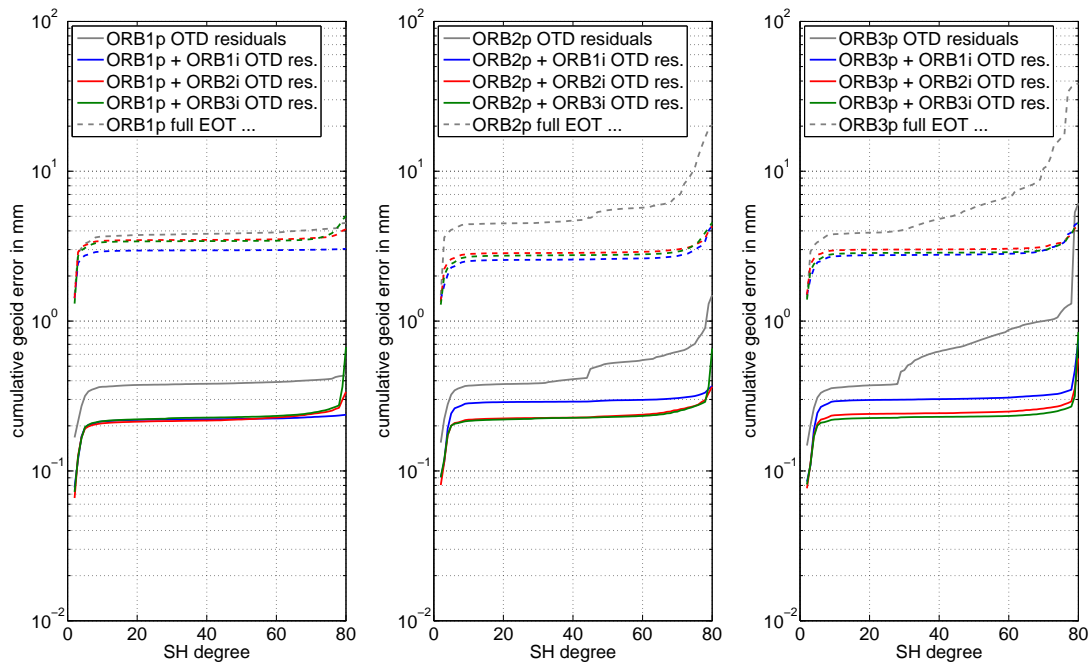


Figure 8.25: Cumulative geoid errors up to  $l_{\max} = 80$  of full (EOT08a, dashed lines) and reduced (EOT08a – FES2004, OTD, solid lines) ocean tide residuals wrt. the mean AOHIS for the three single pairs (gray) and the corresponding double pairs, respectively.



## 9 Summary, Conclusions, and Outlook

Several issues on a Next Generation Gravity Mission (NGGM) are discussed. The time series of gravity fields derived from GRACE is continued with GRACE-FO without a large gap. But there is a need for having a NGGM after GRACE-FO with which the spatial and temporal resolution shall be further increased. This thesis gives significant information for the scientific assessment of the NGGM.

The theoretical basis for the assessment of the NGGM is given in Chap. 2 with the physical description of the Earth's gravity field. The gravitational potential of the Earth is expressed as a series of spherical harmonic (SH) base functions. The SH expansion of the gravitational potential and its functionals is used in spherical approximation.

The observations collected by a gravity satellite mission are used to estimate the SH coefficients of the gravitational potential in a least squares sense (Sec. 2.2). Thereby the application of an adequate stochastic model is necessary in order to weight the observations correctly. The satellite orbits are approximated by only taking into account the effects of the zonal coefficients of degree 0 and 2. Hence, the orbit positions can be formulated analytically (Sec. 2.3).

An important issue for the NGGM is a homogeneous groundtrack coverage. This is valid for repeat orbits performing an integer number of revolutions in an integer number of nodal days. The altitude of a repeat orbit is derived iteratively taking into account the rates of the orbital parameters due to the Earth's flattening term  $J_2$ . Aiming also at short period gravity field signals it is also recommended to find orbits which give a nearly homogeneous groundtrack coverage not only after the whole repeat period but also for specific sub-cycles. An approach is presented how to derive the spatio-temporal sampling of an orbit with its sub-cycles.

For the simulation of gravity retrievals from satellite observations two independent simulation environments are used in this thesis (Sec. 2.4). The first is a semi-analytical approach which is used to estimate in a least squares sense the formal errors of a gravity field retrieval. This simulator is based on the expression of the gravitational potential in a local orbit reference frame. Furthermore, it is computationally fast because of using fast Fourier techniques to evaluate the variance covariance matrix for a gravity field retrieval in the spectral domain. This simulator does not use the observations themselves, but only the spectral representation of the observation noise. Therefore only stochastic effects of a gravity field retrieval can be assessed with this simulator. The second environment is a numerical closed-loop simulator which estimates the variance covariance and the adjusted unknown gravity field parameters by inverting a full normal equation matrix. With this environment also non-stochastic effects can be analysed, which are introduced together with the observations.

The two simulators are compared with respect to the different observation types used in this thesis. The most important observation type for the NGGM is low-low SST in terms of inter-satellite range accelerations. The numerical closed-loop simulator approximates this observation type with the gravitational acceleration differences along the line of sight between the two satellites. Thereby a term consisting of velocity differences between the satellites is neglected. The semi-analytical simulator in this case uses a functional model derived from orbit perturbations implicitly including this term. As the simulation comparison of the two environments in the case of low-low SST gives comparable results this simplification may be seen as not critical.

The objectives of the NGGM are derived from a set of science requirements (Chap. 3). They are consistently expressed in terms of geoid heights and to the basic temporal resolution of one month. Assuming a NGGM with 2 satellites or 2 satellite pairs at maximum the science requirements are

consolidated to a set of observable signals which shall be observed with the required accuracy, and temporal and spatial resolution. From this set the objectives of the NGGM are derived. The NGGM must provide global coverage for specific periods and a long mission duration covering one solar cycle. In order to fulfil the science requirements the geoid must be derived with an accuracy of 0.01 mm at a spatial resolution of 500 km and 0.4 mm at 150 km. The objective for a high spatial resolution of 50 km is not achievable with the NGGM, possibly, as discussed here, for the generation thereafter.

For a set of promising mission scenarios instrument requirements are derived which enable the NGGM to be sensitive to the signals defined in the science requirements (Chap. 4). The scenarios are low-low SST scenarios with improved observation geometry compared to a GRACE-like in-line formation. This is a single low-low SST Pendulum formation and a double low-low SST pair combining two in-line formations on a polar and a lower inclined orbit. Furthermore, the combination of low-low SST and radial satellite gravity gradiometry (SGG) is analysed. But with current technology the radial SGG observations are not able to contribute significantly to a low-low SST mission with a laser interferometry as inter-satellite ranging instrument. The instrument requirements are derived for the two key instruments for a low-low SST mission, i.e. the inter-satellite ranging instrument and the accelerometers measuring the non-gravitational forces acting on the satellite. The instrument requirements depend on the orbital altitude and for the low basic scenarios around 300 km altitude an inter-satellite ranging accuracy of 20 nm is required. For the higher scenarios around 420 km altitude 2 nm are required. For the accelerometers an accuracy around  $2 \cdot 10^{-12}$  m/s<sup>2</sup> is required. An important computational aspect for the assessment of the NGGM is described in Daras et al. (2015): enhanced numerical precision is required to benefit even more from the high instrument accuracies.

In the final simulations error contributions of star sensors, GNSS positioning and so-called tone errors are neglected. These error contributions are discussed in Chap. 5 and requirements are derived for them as well. The largest error contribution for the NGGM is temporal aliasing from high-frequency mass variations due to tidal and non-tidal sources. In Chap. 6 this effect is analysed based on the sampling of signals with discrete frequencies on the equator, observed at the equator crossings of single and double pairs, respectively. Main characteristics of temporal aliasing are resonances depending on the repeat orbit and on the frequency of the signal. The largest high-frequency mass variations are due to ocean tides and non-tidal mass variations in the atmosphere and the oceans. The amplitudes of the non-tidal signals are analysed based on a Fourier series of mass variation models including atmosphere, ocean, hydrology, ice and solid Earth (AOHIS).

Optimal orbits regarding temporal aliasing avoid large resonances and can be found in specific altitude bands in which the basic scenarios are chosen (Chap. 7 and Murböck et al. (2014)). Temporal aliasing leads also to SH resonances in monthly GRACE solutions. This is analysed based on GRACE monthly gravity field time series longer than 8 years from four processing centers. Furthermore, two methods to reduce the SH resonances from a gravity field solution are analysed in the case of double low-low SST pairs and a single pair. For the double pairs it is shown that an optimal weighting depending on the resonance periods for each SH order improves the combination without taking this effect into account. In the case of a single pair a regularization method is applied which introduces pseudo zero observations for the affected SH orders. With both methods an improvement of approximately a factor 2 is achieved.

For the basic single and double pair scenarios closed-loop simulations are performed in order to assess the gravity retrieval performance for the three main error contributions (Chap. 8). This is the instrument noise and the dominating effect of temporal aliasing due to tidal and non-tidal sources. The monthly gravity field retrievals for low and high spatial resolution show that the temporal aliasing effects of the full content of AOHIS is 2 orders of magnitude larger than the instrument noise. For ocean tides the situation is even worse. Temporal aliasing from full ocean tides is 3 orders of magnitude larger than the instrument noise. The double pairs with a polar and inclined pair give the best gravity retrieval performance. The single polar Pendulum formation shows large residuals for the low SH degree zonal coefficients. But for high SH degrees it is nearly as good as the double pairs.

There are different options to reduce high-frequency signals in order to reduce temporal aliasing effects. As applied for GRACE gravity field processing, for example, the high frequency signal contents of AO

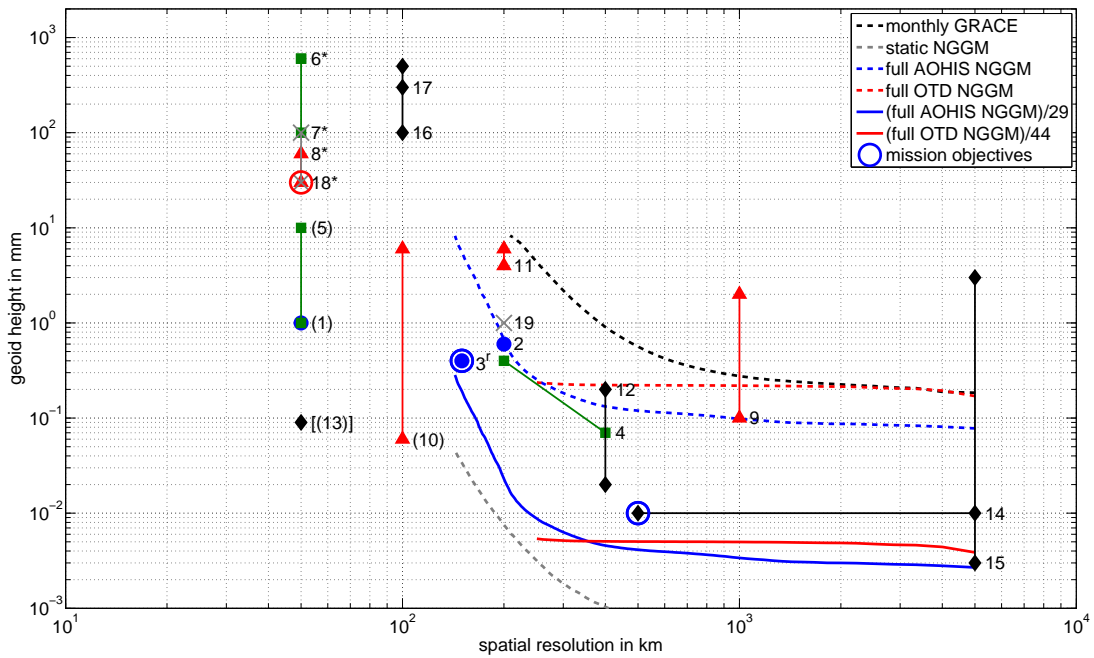


Figure 9.1: Cumulative geoid error in mm for the best NGGM scenario (ORB1p + ORB1i) for different error contributions in comparison with the monthly GRACE error, the science requirements (the numbers correspond to Tab. 3.2), and the mission objectives (cf. Fig. 3.3). The NGGM total geoid error contribution of full (blue dashed) and reduced AOHIS (blue solid) and of full (red dashed) and reduced (red solid) ocean tide differences (OTD).

and ocean tides are reduced with a priori model information. Doing so the effects are reduced by approximately one order of magnitude. But of course the model errors alias into the solution. Furthermore, the functional model can be extended in order to co-estimate additional empirical parameters like, for example, piecewise linear parameters. This option is not analysed in this thesis. A third option of co-estimating short period low resolution gravity parameters in addition to one set of high resolution gravity parameters for one month is described in Wiese et al. (2011). This method is discussed in Sec. 8.2 with respect to an increased temporal resolution of 12 hours in the case of a double pair. Without fully assessing this approach the reduction of temporal aliasing from AOHIS is quantified resulting in an expected improvement of more than a factor of 2.

From the final monthly high spatial resolution gravity field retrievals the main conclusions are derived. The best scenarios are the double pairs including the lowest inclined pair. However, even for these scenarios the cumulative geoid error at 150 km spatial resolution including temporal aliasing from full AOHIS is larger than the required accuracy by a factor between 30 and 50. In the case of temporal aliasing from full ocean tides it is larger than the requirements by a factor of more than 500. A reduced ocean tide impact is analysed by using the difference between two ocean tide model as representation of the ocean tide model errors. In this case the three best scenarios reach a cumulative geoid error larger than the requirements by a factor between 40 and 60.

For the best scenario ORB1p + ORB1i these factors are applied to the full AOHIS signal (reduced by a factor of 29) and the ocean tide differences (reduced by a factor of 44). The resulting cumulative geoid errors for the different contributions are shown in Fig. 9.1 together with the science requirements (the numbers correspond to Tab. 3.2) and mission objectives analogously to Fig. 3.3 depending on the spatial resolution. This NGGM scenario fulfils the mission objectives at 500 and 150 km spatial resolution. It gives an improved geoid error by a factor of approximately 100 compared to a monthly GRACE solution (black dashed line). The NGGM is able to fulfil the requirements above the combined blue and red solid line with required resolution. The requirements with high spatial resolution of 50 km are not fulfilled but the corresponding signals can be observed with reduced spatial resolution.

These applied reduction factors are ambitious requirements. Compared to that, in Gruber et al. (2014)

a classical de-aliasing approach is applied for AOHIS by subtracting the best knowledge on the high-frequency AO variations. This best knowledge is assumed to reach 90% of the full AO signal. Hence, it corresponds approximately to a AOHIS reduction factor of 10 and only a factor of 3 is missing. The reduction factor of 44 for ocean tide model errors has to be seen much more critical.

But for ocean tides there is another possibility to separate these effects from the gravity field parameters. The amplitudes and phases of the different ocean partial tides can be co-estimated in the gravity field retrieval. This is not possible within a monthly retrieval but a long time series is needed in order to separate the different partial tide parameters. It has to be analysed whether a double pair as proposed here for the NGGM is able to reach sufficient accuracy.

Furthermore, the co-estimation of short period gravity parameters (Wiese et al., 2011) including a 12 hours period has to be validated. In this context the formation parameters, especially the ascending node separation of a double pair, has to be further optimized. Another promising mission scenario is able to further improve temporal aliasing reduction. This is the precise ranging between GNSS satellites or GEOs and a number of LEOs on different orbits. This scenario is shortly discussed in Sec. 4.1.

The proposed NGGM scenarios are on the one hand promising wrt. the gravity field retrieval performance. Thereby, the required instrument accuracies are comparable to the accuracies of instruments on present satellite missions. The GOCE accelerometers provide observations with an accuracy in the order of  $10^{-12}$  m/s<sup>2</sup> (Stummer, 2013) and the laser interferometer for GRACE-FO reaches the  $10^{-8}$  m level. But the realization of these accuracies in a low orbital altitude around 300 km requires an expensive and comprehensive satellite instrument concept. Especially the thruster system must be able to fulfil the requirements for the drag compensation and the laser pointing.

The NGGM is of great importance for science and society. Increased spatial and temporal resolution as well as increased accuracy of global gravity field models will improve the understanding of many processes in system Earth. Figure 9.1 shows the science requirements which can be fulfilled with the NGGM with the required resolution. They are in the fields of geodesy, oceanography, hydrology, glaciology, and solid Earth physics (cf. Tab. 3.2). For example, the requirements for unified height systems (SR19), ground water (SR2), glacial isostatic adjustment (SR12), and ice mass balance (SR4) are fulfilled with the NGGM.

## Bibliography

- Anselmi A, (2010). Assessment of a Next Generation Mission for Monitoring the Variations of Earth's Gravity. *Final Report, Document SD-RP-AI-0668, Thales Alenia Space, 22 December 2010.*
- Bender PL, Wiese DN, and Nerem RS, (2008). A Possible Dual-GRACE Mission With 90 Degree And 63 Degree Inclination Orbits. *Proceedings of the 3rd International Symposium on Formation Flying, Missions and Technologies. Noordwijk, Netherlands*, pages 59–64.
- Bock H, Jäggi A, Meyer U, Visser PNAM, van den IJssel J, van Helleputte T, Heinze M, and Hugentobler U, (2011). GPS-derived orbits for the GOCE satellite. *Journal of Geodesy*, 85(11):807–818. doi: 10.1007/s00190-011-0484-9.
- Brockmann JM, Zehentner N, Höck E, Pail R, Loth I, Mayer-Gürr T, and Schuh WD, (2014). EGM\_TIM\_RL05: An Independent Geoid with Centimeter Accuracy Purely Based on the GOCE Mission. *Geophysical Research Letters*, 41(22):8089–8099. doi: 10.1002/2014GL061904.
- Chen YQ, Schaffrin B, and Shum CK, (2008). Continental water storage changes from GRACE line-of-sight range acceleration measurements. In Xu P, Liu J, and Dermanis A, editors, *V Hotine-Marussi Symposium on Mathematical Geodesy*, volume 132 of *International Association of Geodesy Symposia*, pages 62–66. Springer Berlin. IAG Section II Symposium Munich, October 5-9, 1998.
- Cui M, Zeitouny G, Bhattacharya N, van den Berg SA, Urbach HP, and Braat JJM, (2009). High-accuracy long-distance measurements in air with a frequency comb laser. *Optics Letters*, 34(13):1982–1984.
- Dahle C, Flechtner F, Gruber C, König D, König R, Michalak G, and Neumayer KH, (2014). GFZ RL05: An Improved Time-Series of Monthly GRACE Gravity Field Solutions. In Flechtner F, Sneeuw N, and Schuh WD, editors, *Observation of the System Earth from Space - CHAMP, GRACE, GOCE and future missions*, pages 29–39. Springer Berlin Heidelberg. doi: 10.1007/978-3-642-32135-1\_4. Advanced Technologies in Earth Sciences.
- Daras I, Pail R, Murböck M, and Yi W, (2015). Gravity field processing with enhanced numerical precision for LL-SST missions. *Journal of Geodesy*, 2015(89):99–110. ISSN 0949-7714. doi: 10.1007/s00190-014-0764-2.
- Dobslaw H, Bergmann-Wolf I, Dill R, Forootan E, Klemann V, Kusche J, and Sasgen I, (2014). Updating ESA's Earth System Model for Gravity Mission Simulation Studies: 1. Model Description and Validation. *Scientific Technical Report 14/07*. ISSN 1610-0956. doi: 10.2312/GFZ.b103-14079.
- Drinkwater M, Floberghagen R, Haagmans R, Muzi D, and Popescu A, (2003). GOCE: ESA's first Earth Explorer Core mission. In Beutler GB, Drinkwater M, Rummel R, and Steiger R, editors, *Earth Gravity Field from Space - from Sensors to Earth Science, Space Sciences Series of ISSI*, volume 18, pages 419–432. Kluwer Academic Publishers, Dordrecht, Netherlands. ISBN 1-4020-1408-2. doi: 10.1007/978-3-642-37222-3\_54.
- Elsaka B, (2012). Simulated Satellite Formation Flights for Detecting the Temporal Variations of the Earth's Gravity Field. *DGK, Reihe C, 678*. ISSN 0065-5325. ISBN 978-3-7696-5090-7. Verlag der Bayerischen Akademie der Wissenschaften, München.
- Förste C, Flechtner F, Schmidt R, König R, Meyer U, Stubenvoll R, Rothacher M, Barthelmes F, Neumayer KH, Biancale R, Bruinsma SL, and Lemoine JM, (2006). A mean global gravity field mode from the combination of satellite mission and altimetry/gravimetry surface gravity data. *Geophysical Research Abstracts*, 8(03462). Poster presented at EGU General Assembly 2006, Vienna, Austria.
- Gruber T, Bamber JL, Bierkens MFP, Dobslaw H, Murböck M, Thomas M, van Beek LPH, van Dam T, Vermeersen LLA, and Visser PNAM, (2011). Simulation of the time-variable gravity field by means of coupled geophysical models. *Earth System Science Data*, 3(1):19–35. ISSN 1866-3508. doi: 10.5194/essd-3-19-2011. <http://www.earth-syst-sci-data.net/3/19/2011/>.

- Gruber T, Murböck M, Baldesarra M, Brieden P, Danzmann K, Daras I, Doll B, Feili D, Flechtner F, Flury J, Heinzel G, Iran Pour S, Kusche J, Langemann M, Löcher A, Müller J, Müller V, Naeimi M, Pail R, Raimondo JC, Reiche J, Reubelt T, Sheard B, Sneeuw N, and Wang X, (2014). e2.motion - Earth System Mass Transport Mission (Square) - Concept for a Next Generation Gravity Field Mission. *Deutsche Geodätische Kommission der Bayerischen Akademie der Wissenschaften, Reihe B, Angewandte Geodäsie*, (318). ISSN 0065-5317. ISBN 978-3-7696-8597-8. URL <http://dgk.badw.de/fileadmin/docs/b-318.pdf>. Final Report of Project "Satellite Gravimetry of the Next Generation (NGGM-D)".
- Heiskanen WA and Moritz H, (1967). *Physical Geodesy*. W. H. Freeman and Company, San Francisco, United States of America. Library of Congress Catalogue Card Number: 66-24950.
- Iran Pour S, (2013). Sampling the Earth's Time-Variable Gravity Field from Satellite Orbit – Design of Future Gravity Satellite Missions. *DGK, Reihe C, 721*. ISSN 0065-5325. ISBN 978-3-7696-5133-1. Verlag der Bayerischen Akademie der Wissenschaften, München.
- Jekeli C, (1999). The determination of gravitational potential differences from satellite-to-satellite tracking. *Celestial Mechanics and Dynamical Astronomy*, 75(2):85–101. doi: 10.1023/A:1008313405488.
- Kaula WM, (1966). *Theory of Satellite Geodesy*. Blaisdell Publishing Company, Waltham, Massachusetts, United States of America. Library of Congress Catalogue Card Number: 65-14571.
- Keller W and Sharifi MA, (2005). Satellite gradiometry using a satellite pair. *Journal of Geodesy*, 78(9): 544–557. ISSN 0949-7714. doi: 10.1007/s00190-004-0426-x.
- Kim J, (2000). Simulation study of a low-low satellite-to-satellite tracking mission. Dissertation, The University of Texas at Austin.
- Liu X, (2008). Global gravity field recovery from satellite-to-satellite tracking data with the acceleration approach. *Publications on Geodesy 68*. ISSN 0165 1706. ISBN 978 90 6132 309 6. Netherlands Geodetic Commission, Delft.
- Liu X, Ditmar P, Siemes C, Slobbe DC, Revtova E, Klees R, Riva R, and Zhao Q, (2010). DEOS Mass Transport model (DMT-1) based on GRACE satellite data: methodology and validation. *Geophysical Journal International*, 181:769–788. doi: 10.1111/j.1365-246X.2010.04533.x.
- Lyard F, Lefevre F, Letellier T, and Francis O, (2006). Modelling the global ocean tides: modern insights from FES2004. *Ocean Dynamics*, 56:394–415. doi: 10.1007/s10236-006-0086-x.
- Mayer-Gürr T, (2014). ITSG-Grace2014: a new GRACE gravity field release computed in Graz. *GRACE Science Team Meeting (GSTM), Potsdam, Germany, 30 September 2014*.
- Mayer-Gürr T, Eicker A, Kurtenbach E, and Ilk KH, (2010). ITG-GRACE: Global static and temporal gravity field models from GRACE data. In Flechtner FM, Manda M, Gruber T, Rothacher M, Wickert J, Güntner A, and Schöne T, editors, *System Earth via Geodetic-Geophysical Space Techniques*, Advanced Technologies in Earth Sciences, pages 159–168. doi: 10.1007/978-3-642-10228-8\_13, ISBN: 978-3-642-10227-1.
- Mohr PJ, Taylor BN, and Newell DB, (2012). CODATA recommended values of fundamental physical constants: 2010. *Reviews of modern physics*, 84. ISSN 0034-6861. doi: 10.1103/RevModPhys.84.1527.
- Montenbruck O and Gill E, (2005). *Satellite Orbits*. Springer. ISBN 978-3-540-67280-7. Corrected 3rd Printing.
- Murböck M, (2011). Genauigkeitssimulation von Schwerefeld-Satellitenmissionen. Master's thesis, Technische Universität München. Diplomarbeit, german, IAPG / FESG No. 30, ISSN 1437-8280, ISBN-13 978-3-934205-29-1, URL [http://www.iapg.bgu.tum.de/mediadb/935719/935720/iapg\\_fesg\\_rpt\\_30.pdf](http://www.iapg.bgu.tum.de/mediadb/935719/935720/iapg_fesg_rpt_30.pdf).
- Murböck M and Pail R, (2014). Reducing non-tidal aliasing effects by future gravity satellite formations. In Rizos C and Willis P, editors, *Earth on the Edge: Science for a Sustainable Planet, IAG Symposia*, volume 139, pages 407–412. Springer. ISBN 978-3-642-37221-6. doi: 10.1007/978-3-642-37222-3\_54.
- Murböck M, Pail R, Ilias D, and Gruber T, (2014). Optimal orbits for temporal gravity recovery regarding temporal aliasing. *Journal of Geodesy*, 88(2):113–126. ISSN 0949-7714. doi: 10.1007/s00190-013-0671-y.
- Pail R, (2005). A parametric study on the impact of satellite attitude errors on GOCE gravity field recovery. *Journal of Geodesy*, 79(4-5):231–241. doi: 10.1007/s00190-005-0464-z.

- Pail R, Metzler B, Preimesberger T, Lackner B, and Wermuth M, (2007). GOCE quick-look gravity field analysis in the framework of HPF. In *Proceedings 3rd GOCE user workshop*, number ESA SP-627, pages 325–332, Noordwijk. European Space Agency.
- Pail R, Goiginger H, Schuh WD, Höck E, Brockmann JM, Fecher T, Gruber T, Mayer-Gürr T, Kusche J, Jäggi A, and Rieser D, (2010). Combined satellite gravity field model GOCO01S derived from GOCE and GRACE. *Geophysical Research Letters*, 37. ISSN 0094-8276. doi: 10.1029/2010GL044906. EID L20314, American Geophysical Union.
- Panet I, Flury J, Biancale R, Gruber T, Johannessen J, van den Broeke MR, van Dam T, Gegout P, Hughes C, Ramillien G, Sasgen I, Seoane L, and Thomas M, (2013). Earth System Mass Transport Mission (e.motion): A Concept for Future Earth Gravity Field Measurements from Space. *Surveys in Geophysics*, 34(2):141–163. ISSN 0169-3298. doi: 10.1007/s10712-012-9209-8.
- Pavlis NK, Holmes SA, Kenyon SC, and Factor JK, (2012). The development and evaluation of the Earth Gravitational Model 2008 (EGM2008). *Journal of Geophysical Research*, 117. doi: 10.1029/2011JB008916.
- Petit G and Luzum B, (2010). IERS Conventions (2010). *IERS Technical Note No. 36*. URL <http://www.iers.org/IERS/EN/Publications/TechnicalNotes/tn36.html>.
- Rees D, Barnett JJ, and Labitzke K (Editors), (1990). CIRA 1986, COSPAR International Reference Atmosphere, Part II: Middle Atmosphere Models. *Advances in Space Research*, 10(12).
- Rees D (Editor), (1988). COSPAR International Reference Atmosphere 1986 Part 1. Thermospheric Models. *Advances in Space Research*, 8(5/6).
- Reigber C, Lühr H, and Schwintzer P, (2000). Status of the CHAMP Mission. In Rummel R, Drewes H, Bosch W, and Hornik H, editors, *Towards an Integrated Global Geodetic Observing System (IGGOS)*, volume 120 of *International Association of Geodesy Symposia*, pages 63–65. Springer Berlin Heidelberg. ISBN 978-3-642-64107-7. doi: 10.1007/978-3-642-59745-9\_9. IAG Section II Symposium Munich, October 5-9, 1998.
- Reubelt T, Götzelmann M, and Grafarend EW, (2006). Harmonic analysis of the earths gravitational field from kinematic champ orbits based on numerically derived satellite accelerations. In Flury J, Rummel R, Reigber C, Rothacher M, Boedecker G, and Schreiber U, editors, *Observation of the Earth System from Space*. Springer Berlin Heidelberg.
- Reubelt T, Sneeuw N, Iran Pour S, Hirth M, Fichter W, Müller J, Brieden P, Flechtner F, Raimondo JC, Kusche J, Elsaka B, Gruber T, Pail R, Murböck M, Doll B, Sand R, Wang X, Klein V, Lezius M, Danzmann K, Heinzel G, Sheard B, Rasel E, Gilowski M, Schubert C, Schäfer W, Rathke A, Dittus H, and Pelivan I, (2014). *Future Gravity Field Satellite Missions*, pages 165–230. Springer-Verlag Berlin Heidelberg. ISBN 978-3-642-32134-4. doi: 10.1007/978-3-642-32135-1\_21. Advanced Technologies in Earth Sciences, GEOTECHNOLOGIEN Science Report No. 20., ISSN 2190-1635.
- Rummel R, (1979). Determination of short-wavelength components of the gravity field from satellite-to-satellite tracking or satellite gradiometry - an attempt to an identification of problem areas. *Manuscripta Geodaetica.*, 4(2):107–148.
- Savcenko R and Bosch W, (2008). EOT08a - empirical ocean tide model from multi-mission satellite altimetry. *DGFI Report, München, Germany*, 81.
- Schlicht A, Hugentobler U, Schäfer W, Feldmann T, Nothnagel A, Stetter M, Heinze M, Artz T, Pail R, Murböck M, and Reußner E, (2014). Geodesy and Time Reference in Space (GETRIS) and the impact on LEO POD. *Geophysical Research Abstracts*, 16. EGU2014-11330, EGU General Assembly 2014, Vienna, Austria.
- Schlie J, Murböck M, and Pail R, (2014). Feasibility Study of a Future Satellite Gravity Mission Using GEO-LEO Line-of-Sight Observations. In Rizos C and Willis P, editors, *Earth on the Edge: Science for a Sustainable Planet, IAG Symposia*, volume 139, pages 123–130. Springer. doi: 10.1007/978-3-319-10837-7\_16.
- Schuh WD, (1996). Tailored numerical solution strategies for the global determination of the earth’s gravity field. In *Mitteilungen der Institute der Technischen Universität Graz*, number 81, Graz.
- Sharifi MA, (2004). Satellite gradiometry using a satellite pair. Master’s thesis, Universität Stuttgart, Holzgartenstr. 16, 70174 Stuttgart. URL <http://elib.uni-stuttgart.de/opus/volltexte/2004/1998>.

- Sheard BS, Heinzl G, Danzmann K, Shaddock DA, Klipstein WM, and WM Folkner, (2012). Intersatellite laser ranging instrument for the GRACE follow-on mission. *Journal of Geodesy*, 86(12): 1083–1095. ISSN 0949-7714. doi: 10.1007/s00190-012-0566-3.
- Siemes C, (2008). *Digital Filtering Algorithms for Decorrelation within Large Least Squares Problems*. PhD thesis, Rheinische Friedrich-Wilhelm-Universität zu Bonn.
- Sneeuw N, (2000). A semi-analytical approach to gravity field analysis from satellite observations. *DGK, Reihe C*, 527. ISBN 3-7696-9566-6. Verlag der Bayerischen Akademie der Wissenschaften, München.
- Sneeuw N, Flury J, and Rummel R, (2005). Science Requirements on Future Missions and Simulated Mission Scenarios. *Earth, Moon, and Planets*, 94: 113–142. doi: DOI 10.1007/s11038-004-7605-x.
- Stummer C, (2013). Gradiometer Data Processing and Analysis for the GOCE Mission. *DGK, Reihe C*, 695. ISBN 978-3-7696-5107-2. Verlag der Bayerischen Akademie der Wissenschaften, München.
- Tapley BD, Bettadpur S, Watkins M, and Reigber C, (2004). The gravity recovery and climate experiment: Mission overview and early results. *Geophysical Research Letters*, 31(9). doi: 10.1029/2004GL019920.
- Tapley BD, Flechtner F, Bettadpur S, and Watkins M, (2013). The Status and Future Prospect for GRACE After the First Decade. *American Geophysical Union, Fall Meeting 2013, abstract #G32A-01. 2013AGUFM.G32A..01T*.
- Torge W, (2003). *Geodäsie*. Walter de Gruyter, 2 edition. ISBN 3-11-017545-2.
- Vallado DA, (2013). *Fundamentals of Astrodynamics and Applications*. Microcosm Press, 4 edition. ISBN 978-11881883180.
- Visser PNAM, Sneeuw N, Reubelt T, Losch M, and van Dam T, (2010). Space-borne gravimetric satellite constellations and ocean tides: aliasing effects. *Geophysical Journal International*, 181(2):789–805. doi: 10.1111/j.1365-246X.2010.04557.x.
- Watkins MM and Yuan DN, (2012). GRACE: JPL Level-2 Processing Standards Document. URL [ftp://podaac.jpl.nasa.gov/allData/grace/docs/L2-JPL.ProcStds\\_v5.pdf](ftp://podaac.jpl.nasa.gov/allData/grace/docs/L2-JPL.ProcStds_v5.pdf). For Level-2 Product Release 05.
- Weigelt M, van Dam T, Jäggi A, Prange L, Tourian MJ, Keller W, and Sneeuw N, (2013). Time-variable gravity signal in greenland revealed by high-low satellite-to-satellite tracking. *Journal of Geophysical Research*, 118(7):3848–3859. doi: 10.1002/jgrb.50283.
- Welch PD, (1967). The use of fast Fourier transform for the estimation of power spectra: A method based on time averaging over short, modified periodograms. *Audio and Electroacoustics, IEEE Transactions*, 15(2): 70–73. ISSN 0018-9278. doi: 10.1109/TAU.1967.1161901.
- Wiese DN, Folkner WM, and Nerem RS, (2009). Alternative mission architectures for a gravity recovery satellite mission. *Journal of Geodesy*, 83(6):569–581. ISBN 0949-7714. doi: 10.1007/s00190-008-0274-1.
- Wiese DN, Visser PNAM, and Nerem RS, (2011). Estimating low resolution gravity fields at short time intervals to reduce temporal aliasing errors. *Advances in Space Research*, 48(6):1094–1107. doi: 10.1016/j.asr.2011.05.027.
- Wiese DN, Nerem RS, and Lemoine FG, (2012). Design consideration for a dedicated gravity recovery satellite mission consisting of two pairs of satellites. *Journal of Geodesy*, 86(2):81–98. ISBN 0949-7714. doi: 10.1007/s00190-011-0493-8.
- Zhu Z, Zhou ZB, Cai L, Bai YZ, and Luo J, (2013). Electrostatic gravity gradiometer design for the future mission. *Advances in Space Research*, 51:2269–2276. doi: 10.1016/j.asr.2013.01.031.

# Acknowledgements

I would like to thank my supervisors Prof. Roland Pail and Prof. Reiner Rummel for their guidance. They gave me the opportunity to join the GOCE community and to learn a lot in satellite gravimetry from this mission. GOCE has been the basis for my main research activities on the NGGM. I also want to thank my co-examiner Prof. Nico Sneeuw for fruitful discussions during NGGM project meetings.

I would like to thank all my colleagues at the Institute of Astronomical and Physical Geodesy for their feedback and the friendly working environment. Special thanks go to Dr. Thomas Gruber for both excellent research project collaboration and any other support.

This thesis would not have been possible without the support and help from my family and friends. Particularly I am very grateful to my parents and my wife Julia for their encouragement.